1290

UNIVERSIDADE Đ
COIMBRA

Afonso Manuel Lopes Paixão Pereira Marques

CALIBRATION OF THE NEXT-DEMO++ ELECTROLUMINESCENT TIME PROJECTION CHAMBER WITHIN THE NEXT EXPERIMENT

Thesis submitted to the University of Coimbra in fulfillment of the requirements for the Master's Degree in Engineering Physics under the scientific supervision of Ph.D. Neus López March and Ph.D. Filipa Isabel Gouveia de Melo Borges Belo Soares.

October of 2020

1 2 90
FACULDADE DE CIÊNCIAS E TECNOLOGIA
UNIVERSIDADE DE COIMBRA

INTEGRATED MASTER IN ENGINEERING PHYSICS

Calibration of the NEXT-DEMO++ Electroluminescent Time Projection Chamber within the NEXT Experiment

---

Afonso Manuel Lopes Paixão Pereira Marques

Supervisors:

Ph.D. Neus López March
Ph.D. Filipa Borges Belo Soares

LIP
LABORATÓRIO DE INSTRUMENTAÇÃO
E FÍSICA EXPERIMENTAL DE PARTÍCULAS
partículas e tecnologia

IFIC
INSTITUT DE FÍSICA CORPUSCULAR

Coimbra, October of 2020

Ao meu tio Zé...

As for me, I want to have fun while I'm working. Now, not everyone thinks physics is fun, but I do.

DONNA STRICKLAND

If it disagrees with experiment, it's wrong. And that simple statement is the key to science. It doesn't make a difference how beautiful your guess is...

RICHARD FEYNMAN

Agradecimentos

Huc veni ut tibi gratias agerem.

Quero agradecer, em primeiro lugar, às minhas orientadoras de dissertação de mestrado: à **Doutora Neus López**, pela ajuda, empenho e, acima de tudo, paciência que demonstrou ao longo da minha estadia em Valência e pelas muitas horas em chamada por Skype, e à **Professora Doutora Filipa Borges**, que me acolheu num estágio de verão em 2017 no que viria a ser o meu primeiro contacto com o mundo de investigação e que esteve sempre presente para me orientar e esclarecer qualquer dúvida.

À **Professora Doutora Filomena Santos**, o meu especial agradecimento pelas palavras, orientações e sabedoria que me transmitiu, mas principalmente pela preocupação que demonstrou e continua a demonstrar pelo meu bem estar, físico e mental. Ao **Doutor José Escada**, ao **Doutor Rui Silva** e em especial ao aluno de **Doutoramento Alexandre Trindade**, o meu agradecimento pela companhia, pelos conselhos ao longo destes anos, pelas técnicas que aprendi e pela picardia clubística sempre que um dos 3 grandes perdia. À **Nicole**, a mais recente contratação no mercado de verão, agradeço e desejo muito sucesso. Ao **Cortez**, aquele amigo sempre presente para aconselhar sobre problemas nos detetores e para dar a motivação quando as coisas parecem mais tristes, obrigado! Em especial, ao excelente ambiente que vivi nestes 4 anos no **LIP Detetores Gasosos**, pelas conversas sobre a atualidade, desde política até às mais recentes contratações futebolísticas.

A todos os alunos e investigadores do **IFIC**, em Valência, em especial do grupo responsável pelo **NEXT-DEMO++**: **Doutor Ander Estévez**, **Doutor Jose Ángel**, **Doutor Josh Renner** e aos alunos de Doutoramento **Carmen Luque**, **Gonzalo Díaz** e **Ryan Felkai**, mas também a toda a restante equipa com quem privei (**Doutor Michel Sorel**, **Doutor Alberto Andrés**, **Doutor Andrew Laing**, **Doutor José Maria**, **Doutor Justo Martín-Albo**, **Doutora Paola Ferrario** e **Doutor Pau Novella**), o meu profundo agradecimento pela integração tão calorosa no vosso espaço, muitas vezes deixando de falar espanhol para falar inglês, nas reuniões e nas conversas casuais.

À minha mãe **Teresa**, a minha alma gémea, mulher de coragem e exemplo, ao meu pai **Mário**, o melhor cozinheiro do concelho de Cantanhede, e aos meus irmãos **Diogo** e **Fernando**, as pessoas de quem mais gosto e sempre gostarei, a minha gratidão por me proporcionarem uma infância muito feliz, onde nunca me faltou nada, e por confiarem em mim quando disse que queria Engenharia Física em vez de Medicina, para o vosso desagrado. À minha avó **Alicinha**,

a minha “pequerrucha”, e ao meu avô **Etelvino**, o “Mister Etelvine”, obrigado por cuidarem de mim quando era pequeno e ainda o continuarem a fazer, são muito importantes para mim! À restante família, cães e gatos incluídos, agradeço o carinho e atenção.

Em lugar de destaque, ao meu falecido tio **Zé**, que muita falta me faz, por ter estado presente quando o mundo parecia mais negro, distraindo-me dos problemas, motivando-me para ser mais e melhor a cada dia que passa.

A todos os **Professores** que me acompanharam desde o Ensino Primário até à Universidade, a minha gratidão pelo conhecimento que transmitiram, pela dedicação e pela excelente pedagogia que me fez gostar de continuar a ensinar e, se tudo correr bem, também eu ser Professor!

Ao funcionários e amigos do Departamento de Física, **Sr. Cruz**, **Dona Teresa**, **Dona Lurdes**, **Dona Cristina** e **Sr. Sapage** da Secretaria, à **Dona Adélia** da Biblioteca, ao **Engenheiro Nuno** e ao **Emanuel**, obrigado!

Aos colegas, amigos e mentores do **“Cantemus”** e do **“Alma de Coimbra”**, os dois grupos corais que me acompanham desde a infância e entrada na Universidade, respetivamente, obrigado, com especial abraço ao **Maestro Augusto Mesquita**.

À música, aos *huevos* do **Couraça**, à caneca do **Luna** e ao melhor clube de Portugal, **Futebol Clube do Porto**, os meus tubos de escape, um brinde sentido!

Quero agradecer aos meus amigos mais próximos por me aturarem, tarefa que sei ser hercúlea de vez em quando. Aos “Not Dogs”, **David**, **Jordão**, **Brito** e, mais recentemente, **Gabriel**, que continuemos a ser diferentes da rebanhada. À **Carolina**, pela forte amizade que sobreviveu a intrigas de todos os quadrantes. Ao **Hugo**, um dos meus melhores amigos e, certamente, o mais antigo, aquela pessoa que é incapaz de se zangar comigo mais de 5 minutos, o meu colega de quarto nas digressões, obrigado! Aos meus restantes amigos: **Droó**, **Faria**, **Simas**, **Rodrigo**, **Aparício**, **Nuno Brito**, a todo o pessoal Physis e ao G4 do melhor mandato do Núcleo de Estudantes do Departamento de Física, **Félix**, **Filó** e **Padrão**.

Postrema autem non minimus, à **Tânia**, a pessoa mais teimosa que conheço, única e irreverente, com o sotaque mais bonito de Portugal e arredores, mestre em revirar os olhos mas que, por baixo de toda a dureza superficial, consegue ser doce e carinhosa. Encontrei em ti alguém muito parecido comigo, mas acabámos por nos conhecer na altura errada. Não me arrependo de nada. Obrigado por tudo: pelos risos e pelos choros, pela confidência e confiança que depositaste (e espero que deposites) em mim, por me ouvires e me aconselhares... Sei que vais ter muito sucesso na tua vida e espero poder continuar a presenciar os feitos! Obrigado...

Abstract

One of the still lingering mysteries in Physics is the asymmetry matter-antimatter and the reason for the predominance of matter. One of the theories that tries to explain this asymmetry is related to *leptogenesis*, a lepton asymmetry that would induce baryon asymmetry. The key relies on the nature of neutrino, a lepton that until the recent neutrino oscillation experiments was thought to be massless. The possibility arises for the neutrino to be either a Dirac or a Majorana particle. If it is a Majorana neutrino, then its particle is equivalent to the respective antiparticle.

A promising process to prove that the neutrino is a Majorana particle would be the observation of the neutrinoless double beta decay ($\beta\beta^{0\nu}$). In this proposed rare decay there is no emission of neutrinos, violating the total lepton number conservation, a postulate of the Standard Model (SM), that would introduce then a process in favour of *leptogenesis.* The experiments searching for the neutrinoless double beta decay rely on the unarguable detection of the released electrons, requiring large masses of the decaying isotope and large exposure times. In addition, an isotope selection with large Q value favours the process as the phase-space factor $G^{0\nu}$ varies with $Q^5_{\beta\beta}$. More importantly, however, is an energy resolution close to the intrinsic limit to distinguish the signal from this decay from that with neutrino emission. Moreover, a strong background rejection is important as some internal radioactive components may have decay energies close to the $Q_{\beta\beta}$ value. The best results using the isotope ^{136}Xe belong to the experiment KamLAND-ZEN, with a half-life limit of 1.07×10^{26} years, translating into an effective neutrino mass below 0.09 - 0.24 eV.

The NEXT experiment is one of the experiments working with gaseous ^{136}Xe, using a Time Projection Chamber (TPC) at high pressure to unmistakably identify the characteristic energy of the decay. Using xenon is fundamental since it has a decay rate for the double beta decay (with neutrino emission) rather slow (2.2×10^{21} years) when compared to what is expected in the neutrinoless mode. Electroluminescence (EL) is a linear process compared to avalanche detectors, with smaller fluctuations. It is possible to obtain a signal with an energy proportional to the incident particles, thus allowing an energy resolution at FWHM below 0.5 % at the selected energies, sustained by a Fano factor for High Pressure Gaseous Xenon (HPXe) remaining at 0.170 ± 0.007.

The NEXT detectors are based in the Separated Optimised Function TPC (SOFT) principle, where the energy and tracking information are obtained in different planes. This TPC allows for the reconstruction of the 3-dimensional position and the determination of the energy of the primary ionisation event. While the energy is recorded with PMTs, the (X, Y) positions are recorded by an array of SiPMs. The Z-coordinate is calculated from the time difference between the primary and secondary scintillation signals. It is expected, for NEXT-100, a detector currently under construction, a half-life limit of 2.8×10^{25} years for an exposure of 100 kg year, or 6.0×10^{25} years after running 3 years, resulting in an effective neutrino mass of 0.08 - 0.16 eV.

* * *

The NEXT-DEMO++ is an upgraded version of the previous prototype NEXT-DEMO with the purpose of studying different gas mixtures that could reduce the diffusion of the drifting electrons. Moreover, as it has been built with the same sensors as the NEW and NEXT-100 detectors, NEXT-DEMO++ has become an ideal test-bench for NEXT-100 and future NEXT detectors.

In general, the response of NEXT detectors depends on the position of the initial event. To mitigate this effect, that would translate in a degradation of the energy resolution, it is necessary to calibrate the detection to normalise the energy of events occurring in different regions of the detector. This calibration results in the so-called calibration maps that uses an internal ^{83m}Kr point-like, evenly distributed source.

The production of the maps consists on minimising the contribution of undesired events and background by data selection and on correcting the energy of the events (in the case with an exponential function with initial charge, drift time and lifetime of the electrons as parameters).

* * *

Applying the calibration maps to the data collected results in improved energy distributions. In our case, the correct energy is mostly concentrated around 11200 pes, while the uncorrected energy varies between 10500 pes, for a radial region of $0 < R < 20$ mm, to 11000 pes in the outer regions.

The best description of the krypton energy distribution was found to be the fitting of a Gaussian function to the signal contribution and a polynomial function to the background. The polynomial order of the background modelling function does not affect the energy resolution, neither does the fit range. The energy resolution varies from 3.6 to 4.2 % for a radial selection of $20 < R < 30$ mm and a drift time of $150 < DT < 200$ μs and for $0 < R < 20$ mm and $0 < DT < 50$ μs, respectively. The fluctuations on the value are attributed mainly to lower statistical significance in the different regions.

From the geometry of the system, a profile of the radial correction was created. The energy of the events is corrected around 2 % until a radius of $R = 40$ mm, with the correction increasing as the radial section is considered until a maximum of 7 %.

Like in other NEXT detectors, the electrons' lifetime does not depend on the drift time, thus on the Z-coordinate. The lifetime maps also show a lifetime of around 48 ms, a higher value when compared to other NEXT detectors.

The dependence of the energy, for high-energy sources, on the length of the Z-track, seen in other NEXT detector, has also been observed and quantified. Changes in the detector's configuration have been made to explore possible explanations to these observations and data taking is currently ongoing.

Keywords: Neutrinos, Neutrinoless double beta decay, Xenon, Electroluminescence, TPC, NEXT, NEXT-DEMO++, Calibration maps, Krypton, TPB

Sumário

Um dos mistérios que persiste em Física consiste na assimetria matéria-antimatéria e a predominância da matéria. Uma das teorias que tenta explicar esta assimetria é a *leptogenesis*: uma assimetria leptogénica pode induzir uma assimetria bariónica. A chave prende-se com a natureza do neutrino, um leptão que, até às mais recentes experiências de oscilação de neutrinos, se pensava não ter massa. Um neutrino pode, de acordo com esta ideia, ser uma partícula Dirac ou uma partícula Majorana. Se for uma partícula Majorana, então a sua partícula é idêntica à sua antipartícula.

Um processo promissor que pode provar se o neutrino é uma partícula Majorana seria a observação do decaimento beta duplo sem emissão de neutrinos ($\beta\beta^{0\nu}$). Neste decaimento raro não existe emissão de neutrinos violando, assim, a conservação do número leptónico total, um postulado do Modelo Padrão, traduzindo-se num ponto a favor da *leptogenesis*. As experiências que estudam o decaimento beta duplo sem emissão de neutrinos baseiam-se na deteção inequívoca dos eletrões emitidos, com a necessidade de massa elevadas do isótopo em causa, bem como tempos de exposição elevados. Além disso, a escolha de um isótopo com elevado valor de Q favorece o processo, dado que o fator de espaço-fase $G_{0\nu}$ varia com $Q_{\beta\beta}^5$. No entanto, é também importante atingir resoluções em energia que permitam distinguir o sinal deste decaimento do sinal do decaimento com emissão de neutrinos. Ainda, devido ao facto de alguns componentes internos do detetor poderem ter isótopos que decaiam com energias similares a $Q_{\beta\beta}$, é necessário ter uma forte rejeição de ruído de fundo. Os melhores resultados usando o isótopo ^{136}Xe pertencem à experiência KamLAND-ZEN, atingindo um tempo de semivida de 1.07×10^{26} anos, o que equivale a uma massa efetiva do neutrino abaixo de 0.09 - 0.24 eV.

A experiência NEXT é uma das experiências que usa ^{136}Xe gasoso numa Câmara de Projeção Temporal, em inglês Time Projection Chamber (TPC), a alta pressão para identificar de forma inequívoca a energia caraterística deste decaimento. É fundamental o uso de xénon dado que o tempo de semivida no seu decaimento beta duplo com emissão de neutrinos ser relativamente lento (2.2×10^{21} anos) quando comparado com o decaimento sem emissão de neutrinos. A Eletroluminescência (EL) é um processo linear e com menores flutuações quando comparado com detetores baseados em avalanche. É possível obter um sinal com uma energia proporcional à energia das partículas incidentes, permitindo atingir resoluções em energia (FWHM) menores que 0.5 % nas energias em causa, facto corroborado pelo fator de Fano de 0.170 ± 0.007 para o xénon gasoso a alta pressão.

Os detetores do NEXT baseiam-se no príncipio TPC de Funções Otimizadas Separadas, em inglês Separated Optimised Function TPC (SOFT), que consiste em recolher a informação sobre a energia e posição tridimensional da ionização primária em diferentes planos. Enquanto que a energia é registada em PMTs, as coordenadas (X, Y) são registadas por um *array* de SiPMs. A coordenada Z é calculada a partir da diferença temporal entre os sinais de cintilação primária e secundária. É esperado que o detetor em construção NEXT-100 atinja um tempo de semivida de 2.8×10^{25} anos para uma exposição de 100 kg ano, ou 6.0×10^{25} anos depois de coletar dados durante 3 anos, o que corresponde a uma massa efetiva de neutrino de 0.08 - 0.16 eV.

* * *

O NEXT-DEMO++ é uma versão atualizada do protótipo NEXT-DEMO com o propósito de estudar diferentes misturas gasosas de modo a reduzir a difusão dos eletrões. Além disso, dado que usa os mesmos sensores que o detetor NEW e o NEXT-100, é um excelente detetor para testar vários aspetos do NEXT-100 e de futuros detetores.

A resposta de um detetor do NEXT depende, em geral, da posição do evento inicial. Para mitigar este efeito, que se traduz na degradação da resolução em energia, é necessário calibrar o detetor de modo a normalizar a energia dos eventos nas diferentes regiões do detetor. Estas calibrações resultam em mapas de calibração que usam o decaimento de ^{83m}Kr, uma fonte radioativa interna de baixa energia, como referência.

A produção destes mapas consiste na seleção dos dados para reduzir a contribuição de outros eventos e do ruído de fundo e, posteriormente, na correção da energia (que, neste caso, consiste no fit de uma função exponencial onde a carga inicial, o tempo de deriva e o tempo de vida são parâmetros).

* * *

Após aplicar os mapas de calibração, a distribuição de energia é melhorada. Neste caso, a distribuição de energia corrigida está maioritariamente concentrada em 11200 pes, enquanto que a distribuição de energia não corrigida varia entre 10500 pes, para a região radial $0 < R < 20$ mm e entre 11000 pes para a região mais exterior do detetor.

A melhor forma de descrever o sinal de energia consiste em fazer um fit da uma função gaussiana na região do pico e uma função polinomial para descrever o fundo. O grau da função polinomial e o intervalo em que se faz o fit não afeta o valor da resolução em energia. A resolução em energia obtida varia entre 3.6 e 4.2 % para a região radial $20 < R < 30$ mm e um tempo de deriva $150 < DT < 200$ μs para o primeiro valor e $0 < R < 20$ mm e $0 < DT < 50$ μs para o segundo valor. A diferença entre os dois valores é atribuída a diferentes significâncias estatísticas nas várias regiões do detetor.

Foi feito ainda um perfil radial das correções aplicadas. A energia dos eventos é corrigida cerca de 2 % até uma região radial de $R = 40$ mm, aumentando à medida que nos aproximamos da região mais exterior do detetor até um valor de 7 %.

Tal como observado nos outros detetores do NEXT, o tempo de vida dos eletrões não depende do seu tempo de deriva e, consequentemente, na coordenada Z. O tempo de vida obtido tem um valor médio de cerca de 48 ms, um valor mais elevado quando comparado com os outros detetores.

A dependência da energia, para fontes de alta energia, com o traço da coordenada Z, efeito presente em outros detetores do NEXT, foi observada e quantificada. De modo a explorar possíveis explicações, foram feitas modificações no detetor e, de momento, está a ser feita a coleção e análise dos dados.

Palavras-chave: Neutrinos, Decaimento beta duplo sem emissão de neutrinos, Xénon, Eletroluminescência, TPC, NEXT, NEXT-DEMO++, Mapas de calibração, Krypton, TPB

Contents

List of Figures

List of Tables

List of Acronyms and Initials

ADC Analog-to-Digital Converter. 45, 46

AMoRE Advanced Mo-based Rare process Experiment. xii, xvii, 90

BBN Big Bang Nucleosynthesis. 8

BFS Breadth First Search. 50

BLR Baseline Restoration. 46

CANDLES Calcium fluoride for the study of Neutrinos and Dark matters by Low Energy Spectrometer. xii, xvii, 16, 85

CCWFs Calibrated Corrected Waveforms. 47

CL Confidence Limit. xix, 6, 7, 16–20, 33, 34, 86, 87

CMB Cosmic Microwave Background Radiation. 8

COBRA Cadmium Zinc Telluride 0-Neutrino Double-Beta. xii, xix, 86, 87

CP Charge conjugation Parity. 9

CUORE Cryogenic Underground Observatory for Rare Events. xiii, 12, 16, 17, 86

CWFs Corrected Waveforms. 46

DBDM Double Beta Dark Matter. xiv, 29

DCBA Drift Chamber Beta-ray Analyzer. xii, xvii, xix, 87, 88

DCBA/MTD Drift Chamber Beta-ray Analyzer and Magnetic Tracking Detector. xii, xvii, 87, 88

DIPC Donostia International Physics Center. 2

DONUT Direct Observation of the NU Tau. 4

EC Electron Capture. xiii, xv, 12, 51, 52

EL Electroluminescence. iii, v, vii, xiii, xvii, 25, 27–30, 32, 37–39, 43, 48, 77, 79–82, 84

EXO Enriched Xenon Observatory. xiii, 12, 18

FLARES Flexible Scintillation Light Apparatus for Rare Event Searches. xii, 89

FPGA Field-programmable Gate Array. 40, 45

FWHM Full Width at Half Maximum. iii, vii, xvi, 17, 18, 20, 21, 23, 29, 69, 89

GERDA Germanium Detector Array. xiii, 12, 16, 18, 19

HDPE High Density Polyethylene. xiv, 30, 37

HPXe High Pressure Gaseous Xenon. iii, 25, 26

IC Internal Conversion. xv, 51, 52

IFIC Instituto de Física Corpuscular. xiv, 1, 2, 28, 35

INFN National Institute of Nuclear Physics. 17

ITO Indium Tin Oxide. 30, 32, 36, 38, 82

KamLAND Kamioka Liquid Scintillator Antineutrino Detector. xiii, 12, 16, 19, 20

KATRIN Karlsruhe Tritium Neutrino Experiment. 7

LBNL Lawrence Berkeley National Laboratory. 29

LIP Laboratório de Instrumentação e Física Experimental de Partículas. 1

LNGS Laboratori Nazionali del Gran Sasso. 17, 86

LSC Laboratorio Subterráneo de Canfranc. 23, 30

LUCIFER Low-background Underground Cryogenic Installation For Elusive Rates. xii, xvii, 86

LXe Liquid Xenon. 26

MCCs Metallic Magnetic Calorimeters. 90

MM Micromegas. xiv, 29, 30

MNS Maki-Nakagawa-Sakata. 5

MOON Molybdenum Observatory Of Neutrinos. xii, xvii, 89

MPGDs Micro-pattern Gaseous Detectors. 29

NEMO Neutrino Ettore Majorana Observatory. xiii, 12, 16, 20, 21

NEW NEXT-White. iv, viii, xiv, 30–32, 35, 36, 66, 78, 83, 84

nEXO Next-generation Enriched Xenon Observatory. 18

NEXT Neutrino Experiment with a Xenon TPC. i, iii–v, vii–ix, xiv, 1, 2, 11, 23, 26–30, 32–38, 40–43, 45–47, 51, 52, 78, 79, 83, 84

PandaX Particle and Astrophysical Xenon Detector. 22

PMNS Pontecorvo-Maki-Nakagawa-Sakata. 5

PMTs Photomultiplier Tubes. iv, viii, xiii, xiv, 18, 20, 22, 26–30, 32, 34, 36, 37, 41, 42, 45–50, 52, 81, 83

PTFE Polytetrafluoroethylene. 36

RGA Residual Gas Analyser. 39

RWFs Raw Waveforms. xiv, 45–47

SDDs Silicon Drift Detectors. xvii, 89, 90

SDSS Sloan Digital Sky Survey. 6

SiPMs Silicon Photomultipliers. iv, viii, xiii, xiv, 26–28, 30–32, 34, 36, 37, 41, 42, 45, 47–51, 56, 82, 83

SM Standard Model. iii, 7, 9, 11, 13

SNO Sudbury Neutrino Observatory. xiii, 20, 21

SOFT Separated Optimised Function TPC. iv, viii, xiii, 26, 27

SQUIDs Superconducting Quantum Interference Devices. 90

TPB Tetraphenyl Butadiene. v, ix, xiv, 28, 30, 32, 36–38, 52, 82, 84

TPC Time Projection Chamber. iii–v, vii, ix, xiii, 11, 18, 22, 23, 26, 29, 30, 32, 36, 83

VUV Vacuum Ultraviolet. 25, 28, 38, 82

Y2L Yangyang underground Laboratory. 90

Introduction

Motivation and goals of the project

Since my first research project at LIP in the summer of 2017, I have developed an interest for gaseous radiation detectors. Although the portuguese heritage on this subject is extensive, specially in the research groups from University of Coimbra, I wanted to broaden my knowledge regarding this kind of detector and experience how "big" experiments use them.

For this, I applied for an ERASMUS+ scholarship to attend the University of Valencia, more specifically IFIC. IFIC is a well-known and important laboratory in the area of high-energy, nuclear, neutrino and astroparticle physics. It is also a member of the NEXT collaboration, like LIP, a neutrinoless double beta decay experiment. This experiment aims to prove that the neutrinoless double beta decay is a plausible decay to explain the matter-antimatter asymmetry.

I was very happy for being accepted! This would not only be a very good academic experience, but also would allow me to spend some months in another country, reinforcing my English and Spanish language skills and experiencing a different culture. More importantly, this would allow me to cooperate with an interesting and promising experiment!

* * *

This project was mostly done at IFIC in Valencia with Dr. Neus López and its goals are the following:

1. Operation of NEXT-DEMO++ and data taking in different electrical conditions.
2. Development and enhancement of the map production algorithm.
3. Evaluation of the quality of the calibration maps.

The NEXT collaboration

The NEXT collaboration involves several groups from:

- **Portugal** - University of Coimbra and University of Aveiro.
- **USA** - Harvard University, Fermilab, Argonne National Laboratory, Iowa State University, Lawrence Berkeley National Laboratories, Texas A&M University and University of Texas at Arlington.

- **Spain** - IFIC, DIPC, Autonomous University of Madrid, University of Girona, Polytechnic University of Valencia, University of Santiago de Compostela and University of Zaragoza.
- **Israel** - Ben Gurion University of the Negev.
- **Colombia** - Antonio Nariño University.

Thesis structure

This thesis will be structured in 6 chapters, conclusions and future work and 3 appendixes.

In **Chapter 1 - Neutrinos**, a brief explanation on how the neutrinos were discovered is presented, then neutrinos as particles with mass are introduced. After, the two possible natures of the neutrinos (Dirac and Majorana) are opposed in order to try to explain the origin of their mass, later introducing a theory to explain the observable baryon asymmetry.

The **Chapter 2 - Searching for neutrinoless double beta decays** is reserved to explain the double beta decay with and without emission of neutrinos and to describe the state of the art of the detectors searching for the neutrinoless double beta decay.

In **Chapter 3 - NEXT experiment**, the NEXT experiment will be introduced and also the reasons behind using xenon as a source and detection medium in the NEXT detector. The concept of the NEXT detectors is also presented. A detailed history of the different detectors, from the prototypes like NEXT-DEMO to the final goal, the NEXT-ton, is shown.

The **Chapter 4 - The NEXT-DEMO++**, a detailed description of the NEXT-DEMO++ detector is presented, not only in a instrumentation point of view, but also in a software and data taking angle. This is the detector where all data used for this project was taken.

In **Chapter 5 - Data processing algorithms**, the algorithms used in the NEXT experiment are disclosed, from the first steps of the raw data, to the fully processed and refined information.

In **Chapter 6 - Producing correction maps** the steps necessary to produce a correction map are detailed, from the initial data selection in order to remove unnecessary background showing several examples, the procedure in which the correction map is based upon, until the application of the map in the correction of the high energy events in caesium and thorium.

Finally, in **Conclusions and future work**, some final comments are presented with the future studies that are important to do. In **Appendix A** are summarised other experiments working on the neutrinoless double beta decay and their best results and in **Appendix B** some relevant demonstrations.

Chapter 1

Neutrinos

This chapter is directed to discussing the evolution of the physics behind the neutrinos, since the prediction of the electron neutrino in 1930 to the latest theories about the origin of their mass. Also, a brief discussion of matter over antimatter, ruling in the observable universe is included, relating it to the nature of the neutrinos.

1.1 Historical conception

"I have done a terrible thing: I have postulated a particle that cannot be detected."

Wolfgang Pauli

1.1.1 The origins

In 1914, the British physicist James Chadwick proved that the emitted electrons from a beta decay had a continuous energy spectrum unlike the alpha particles or the gamma photons which had a single energy. This would compromise the energy conservation law. Also, the conservation of the angular momentum was not guaranteed.

The neutrino[1] was postulated by Wolfgang Pauli in 1930. This hypothetical particle would be emitted at the same time as the electron and would carry out the necessary energy, momentum and spin to apply the conservation laws in a beta decay. This particle would also have a sufficiently high penetration depth to not be stopped in a calorimeter. The conservation of charge and spin would require this particle to be a neutral fermion (spin = 1/2).

1.1.2 The first neutrino

It was Enrico Fermi that baptised the particle with the name "neutrino" in 1932. He provided a solid theory about the beta decay, but his original paper was rejected by *Nature*. Fermi developed a relationship, now referred to as Fermi's Golden Rule, which states that the transition

---

[1] Actually named "neutron" at the time.

probabilities are proportional to the strength of the coupling between the initial and final states and also to the density of final states.

It was in 1954 that Cowan and Reines proved experimentally the existence of neutrinos. A nuclei containing Z protons and N neutrons may have one of its neutrons decay into the following:

$$(Z, N) \rightarrow (Z+1, N-1) + e^- + \overline{\nu}_e \tag{1.1}$$

This is called the β decay, where a neutron decays into a proton, emitting an electron and an antineutrino. Other possibility involving neutrinos is the inverse β decay where the antineutrino goes to the left side of equation 1.1 and becomes its antiparticle, the neutrino:

$$\nu_e + (Z, N) \rightarrow (Z+1, N-1) + e^- \tag{1.2}$$

The same logic stands for the the β^+ decay:

$$(Z, N) \rightarrow (Z-1, N+1) + e^+ + \nu_e, \tag{1.3}$$

where a proton decays into a neutron, emitting a positron and a neutrino. The inverse β^+ decay is:

$$\overline{\nu}_e + (Z, N) \rightarrow (Z-1, N+1) + e^+ \tag{1.4}$$

This last reaction was the one used to prove the existence of neutrinos by Cowan and Reines. This would be the first real proof of one of the neutrino versions (latter called flavours): electron neutrino [1, 2].

1.1.3 The second neutrino

Six years later, Jack Steinberger, Leon Lederman and Melvin Schwartz discovered the second type of neutrino. This novel neutrino was found in a pion decay in the collision of two protons and involving muons. For that, it was named muon neutrino [3]:

$$p + \text{Be} \rightarrow \text{hadrons} \rightarrow \mu + \nu_\mu + \text{X} \tag{1.5}$$

1.1.4 The third neutrino

Although the existence of a third neutrino type was conceived in 1970 by Martin Lewis Perl, due to the discovery of a new particle (tau), only in 2000 the DONUT collaboration at Fermilab announced its empirical existence [4]. This would be known as the tau neutrino.

1.2 Neutrinos as massive particles

“300 trillion neutrinos walk into a bar. Then walk through the bar.”

Bossy Boson, a webcomic about particle physics

Neutrinos, like electrons, muons and tau particles, are leptons, which means that they have half-integer angular momentum and do not undergo strong interactions. However, unlike other leptons, they are neutrally charged. Their resulting cross section is around 1.2×10^{-43} cm^2 in the inverse β^+ decay which means that to have a good probability of an interaction with a neutrino, around 10 light-years of material must be available [5].

Neutrinos are the lightest of all fermions and past experiments have shown that three flavours of neutrinos exist. Moreover, experiments related to neutrino oscillations have proved that neutrinos have mass [6–8]. These experiments can only measure the mass difference between the flavour oscillations. Thus, being massive particles that only undergo weak interactions, their flavour eigenstates ν_α are linear combinations of the mass eigenstates ν_i. The mathematics associated are similar to the mathematics of a rotation:

$$|\nu_\alpha\rangle = \sum_{i=1}^{3} U^{\star}_{\alpha i} \, |\nu_i\rangle \, , \qquad \alpha = e, \mu, \tau, \tag{1.6}$$

where U is a 3×3 *neutrino mixing matrix*, often called as the Pontecorvo-Maki-Nakagawa-Sakata (PMNS) or Maki-Nakagawa-Sakata (MNS) mixing matrix, different from the identity matrix[2]. One of the implications of equation 1.6 is the violation of the individual lepton charges, but not necessarily of the sum of these values.

Regarding neutrinos, there are still three major unknowns: the neutrino mass ordering, the absolute value of the lightest neutrino and the origin of the neutrino mass[3].

For the first one, there are two possibilities: *normal* and *inverted mass orderings*, as seen in figure 1.1.

As for the normal mass ordering, the small mass difference (Δm^2_{sol}) corresponds to the gap between the two lightest mass eigenstates, measured in solar experiments (electron neutrinos produced in the thermonuclear reactions in the stars). On the other hand, for the inverted mass ordering, the gap (Δm^2_{atm}) corresponds to the large mass difference, which is measured by atmospheric experiments (cosmic rays interacting with air in the atmosphere produce pions and kaons that decay into electron and muon neutrinos and antineutrinos).

The absolute value of the lightest neutrino (m_{light}) can be investigated via cosmological observations, beta decay experiments and neutrinoless double beta decay searches (the last will be discussed in the following chapter).

---

[2] If $U = I$, then the flavour eigenstates would be the mass eigenstates.

[3] This will be discussed in next section.

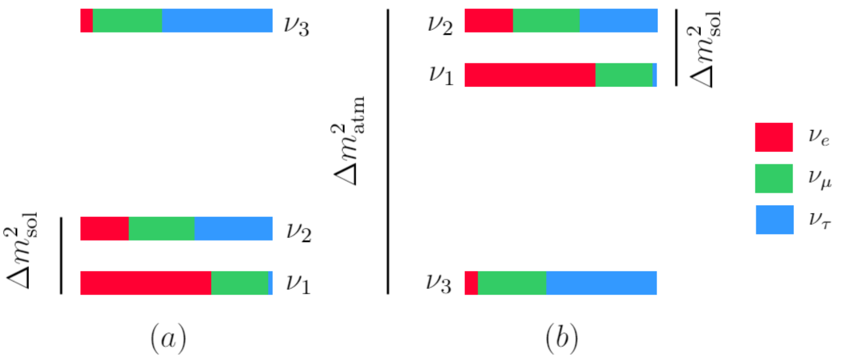

Figure 1.1: Normal (a) and inverted mass orderings (b), with the increase of neutrino masses from bottom to top (adapted from [9]).

From cosmological observations, we can get the sum of the three neutrinos masses:

$$m_{\rm cosmo} \equiv \sum_{i=1}^{3} m_i \tag{1.7}$$

The relationship between the $m_{\rm cosmo}$ and $m_{\rm light}$, which corresponds to m_1 in the case of the normal mass ordering and to m_3 in the case of the inverted mass ordering, can be seen in figure 1.2 (a).

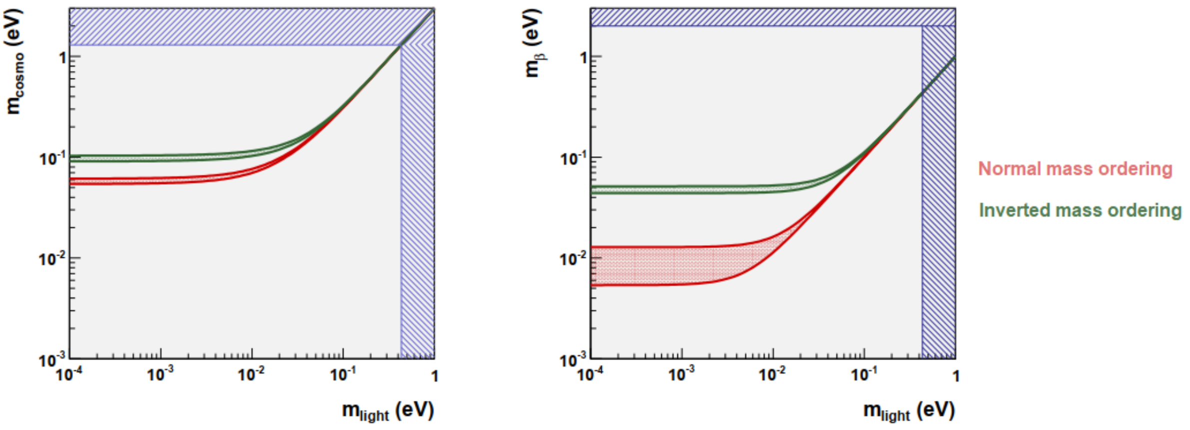

(a) (b)

Figure 1.2: Constraints on the $m_{\rm light}$ from (a) cosmological and (b) β decay experiments. The $m_{\rm cosmo}$ upper bound in panel (a) is from [10]. The cosmological constraint on $m_{\rm light}$ is also shown in panel (b), together with the upper limit on m_β from tritium β decay experiments [11].

More recent studies published by Sloan Digital Sky Survey [12] produced the following value, with a Confidence Limit (CL) of 95 %:

$$m_{\rm cosmo} = 0.11 \pm 0.03 \ \text{eV} \tag{1.8}$$

As for the beta decay experiments, we can write the mass m_β as a combination of the mass eigenstates, represented both in figure 1.2 (b) and equation 1.9.

$$m_\beta^2 \equiv \sum_{i=1}^{3} |U_{ei}|^2 \, m_i^2 \tag{1.9}$$

The most accurate results are based on the decay of tritium and the combined limit of Troitsk [13] and Mainz [14] experiments is [15], with a CL of 95 %:

$$m_\beta < 2 \text{ eV} \tag{1.10}$$

It is expected that the Karlsruhe Tritium Neutrino Experiment (KATRIN) experiment [16] to reach a sensitivity of 0.30 eV (3σ) and 0.35 eV (5σ).

1.3 Dirac *versus* Majorana: origin of neutrino mass

"I made a decision that has become unavoidable. There isn't a bit of selfishness in it, but I realise what trouble my sudden disappearance will cause you and the students (...) I will keep a fond memory of them all at least until 11 pm tonight, possibly later too."

Ettore Majorana to Antonio Carrelli

In the Standard Model (SM), neutrinos are introduced as massless particles. However, we now know that neutrinos are massive particles and therefore changes in the SM must be made. Fermion masses result from the Yukawa interactions with the Higgs field [17], which involve the existence of fermions with left and right-handed chirality. However, only left-handed neutrinos have been experimentally detected [18] (and also only right-handed antineutrinos). To explain the existence of mass, we introduce two mass terms: Dirac and Majorana.

A Dirac neutrino mass term can be generated by only introducing right-handed chirality terms in the SM of the neutrino fields. This model is often called *minimally extended Standard Model* and the right-handed neutrino fields are called *sterile*, meaning that they only interact by gravitational forces. In contrast, the left-handed neutrino fields are called *active* since they also interact with the weak force. However, this mass term by itself does not explain the smallness of neutrino Yukawa couplings.

Ettore Majorana proposed, in 1937[4] [19], another way of adding the neutrino mass term to SM. He stated that for neutral particles, like neutrinos, two of the four degrees of freedom can be discarded from the massive spinor field, a condition that implies we only need one field to describe neutrino and antineutrino states:

$$\nu^c = \nu, \tag{1.11}$$

---

[4] One year before his tragic disappearance.

where ν^c is the charge-conjugate of ν which, by decomposition [17], gives:

$$\nu_R = (\nu_L)^c \tag{1.12}$$

The major conclusion of equation 1.12 is that the right-handed chirality term of the Majorana neutrino field ν_R is obtained from its left-handed counterpart ν_L. Moreover, these mass terms are not only forbidden for the other electrically charged fermions due to the charge conservation, but also imply the violation of the conservation of the lepton number by two units due to the possibility of conversion of a neutrino into a antineutrino. In other words, a Majorana neutrino is identical to its antiparticle.

For Majorana neutrinos, the detection of different sign muons in a scattering experiment, as shown in figure 1.3, would give a clear confirmation on the neutrino's nature, but the cross-section in such process would be very small and the muons virtually undetectable. For example, for a beam of $E_\nu = \mathcal{O}(1)$ GeV and a neutrino mass of $m_\nu \sim \mathcal{O}(1)$ eV, the resulting cross-section would be 10^{-18} times the usual charged-current neutrino cross-section [20].

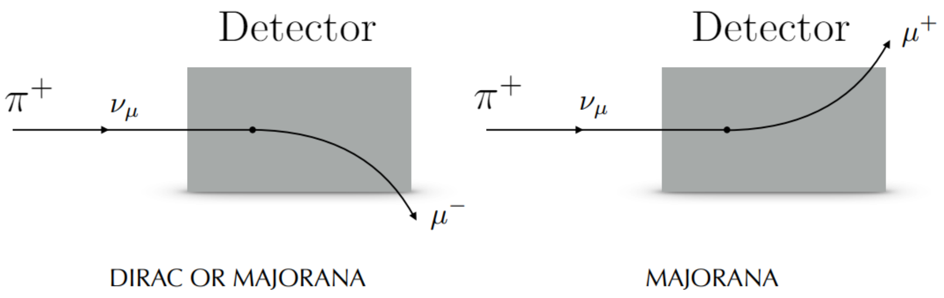

Figure 1.3: Scattering experiment to assess neutrino nature: a muon neutrino beam is sent to a large magnetised detector and the observation of different sign muons would be a signature of Majorana neutrinos. Adapted from [17, 20].

1.4 Leptogenesis

"In the beginning there was nothing, which exploded."

John Pratchett

The models of formation of the universe predict the same amount of matter and antimatter in the beginning of time. However, from several observations such as Big Bang Nucleosynthesis (BBN) and Cosmic Microwave Background Radiation (CMB), we can deduce a small baryon asymmetry that have left us in a matter-dominated universe today. The asymmetry has already been precisely measured [9]:

$$\eta \equiv \frac{n_B - n_{\bar{B}}}{n_\gamma} = (6.19 \pm 0.15) \times 10^{-10}, \tag{1.13}$$

with $n_B, n_{\bar{B}}$ and n_γ as the densities of baryons, antibaryons and photons.

One of the theories to explain this baryon asymmetry states that it was induced by a lepton asymmetry called *leptogenesis* [21]. Basically, if neutrinos are Majorana particles, the decays of these heavy particles into leptons would provide the conditions for leptogenesis.

To have leptogenesis, there are some conditions that have to be met which are named *Sakharov's conditions* [22, 23]:

1. Existence of a process that violates the lepton number conservation which, as previously mentioned, may happen in the decay of heavy Majorana neutrinos.
2. CP violation sources beyond the SM, also present in these decays ($\Delta L = 2$).
3. Departure from thermal equilibrium, which will occur if the decay rate is slower than the universe's expansion rate.

Table 1.1 shows a compilation of processes where the lepton number conservation is violated. As we can see, the process $\beta\beta^{0\nu}$, corresponding to the neutrinoless double beta decay, discussed in detail in the next chapter, is the one that yields a lower effective Majorana mass.

Table 1.1: Most recent boundaries on effective neutrino masses according to total lepton number violating processes taken from from [9, 11, 24]. $T_{1/2}$ is the decay half-life and Γ is the decay rate.

Flavours	Experimental Technique	Experimental bound	Mass (eV)
(e, e)	$\beta\beta^{0\nu}$	$T_{1/2}\left({}^{76}\mathrm{Ge} \to {}^{76}\mathrm{Se} + 2e^-\right) > 1.9 \times 10^{25}$ yr	$< 3.6 \times 10^{-1}$
(e, μ)	$\mu^- \to e^+$	$\dfrac{\Gamma\left(\mathrm{Ti} + \mu^- \to e^+ + \mathrm{Ca_{gs}}\right)}{\Gamma\left(\mathrm{Ti} + \mu^- \text{ capture}\right)} < 1.7 \times 10^{-12}$	$< 1.7 \times 10^{7}$
(e, τ)	Rare τ decays	$\dfrac{\Gamma\left(\tau^- \to e^+\pi^-\pi^-\right)}{\Gamma_{\mathrm{tot}}} < 8.8 \times 10^{-8}$	$< 2.6 \times 10^{12}$
(μ, μ)	Rare kaon decays	$\dfrac{\Gamma\left(K^+ \to \pi^-\mu^+\mu^+\right)}{\Gamma_{\mathrm{tot}}} < 1.1 \times 10^{-9}$	$< 2.9 \times 10^{8}$
(μ, τ)	Rare τ decays	$\dfrac{\Gamma\left(\tau^- \to \mu^+\pi^-\pi^-\right)}{\Gamma_{\mathrm{tot}}} < 3.7 \times 10^{-8}$	$< 2.1 \times 10^{12}$
(τ, τ)		Non-existing	

Chapter 2

Searching for neutrinoless double beta decays

In this chapter, the focus will be on the double beta decay with and without the emission of neutrinos, summarising the best results for both cases. Since the subject of this thesis relies on the neutrinoless mode, a state of the art discussion on the ongoing experiments (excluding the NEXT experiment) will be made.

2.1 Double beta decay

"Neutrinos have mass? I didn't even know they were Catholic!"

Dan Brown

In 1935, Maria Goeppert-Mayer [25] considered the double beta decay $\left(\beta\beta^{2\nu}\right)$ as a rare nuclear transition where two neutrons decay into two protons, with simultaneous two beta decays. This decay comprises the total lepton number conservation, thus it is allowed in the SM.

$$(Z, N) \rightarrow (Z+2, N-2) + 2e^{-} + 2\,\overline{\nu}_e \tag{2.1}$$

This decay is only possible if the initial nucleus is less bound than the final one, and both more bound than the intermediate one, as we can see in figure 2.1. This condition is present in 35 nuclides. 15 years later, this decay was indirectly observed by Mark Inghram and John Reynolds using the isotope ^{130}Te [26]. However, only in 1987 was there a direct evidence for $\beta\beta^{2\nu}$ decays by S. R. Elliott, A. A. Hahn and M. K. Moe, using a Time Projection Chamber (TPC) with ^{82}Se [27].

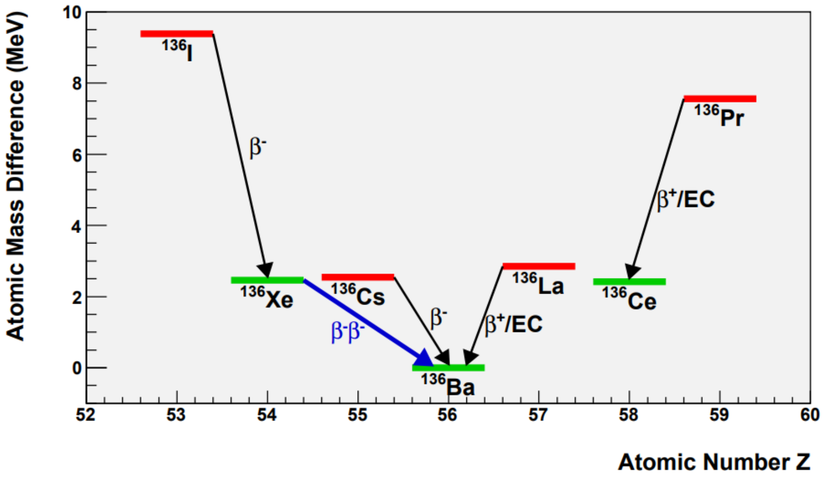

Figure 2.1: Atomic masses of $Z + N = 136$ isotopes. The atomic mass differences are with respect to the most bound isotope, ^{136}Ba. The red levels indicate odd-odd nuclei, while the green ones indicate even-even nuclei (Electron Capture (EC)) [9].

The typical half-life for this type of decay is around $10^{18} - 10^{22}$ years. In table 2.1 we can see a list of the most reliable direct measurements for $\beta\beta^{2\nu}$, obtained from [17, 28].

Table 2.1: Weighted-average half-life values for $\beta\beta^{2\nu}$ decays from the best direct measurements.

Isotope	$T_{1/2}$ ($\times 10^{21}$ years)	Experiment
^{48}Ca	$0.064^{+0.007}_{-0.006} \pm^{+0.012}_{-0.009}$	NEMO-3 [29]
^{76}Ge	1.926 ± 0.094	GERDA [30]
^{78}Kr	$9.2^{+5.5}_{-2.6} \pm 1.3$	BAKSAN [30]
^{82}Se	$0.0939 \pm 0.0017 \pm 0.058$	NEMO-3 [29]
^{96}Zr	$0.0235 \pm 0.0014 \pm 0.0016$	NEMO-3 [29]
^{100}Mo	0.00693 ± 0.00004	NEMO-3 [29]
^{116}Cd	$0.0274 \pm 0.0004 \pm 0.0018$	NEMO-3 [29]
^{128}Te	7200 ± 400	Geochemical [29]
^{130}Te	$0.82 \pm 0.02 \pm 0.06$	CUORE-0 [31]
^{134}Xe	> 0.87	EXO-200 [32]
^{136}Xe	$2.38 \pm 0.02 \pm 0.14$	KamLAND [32]
^{150}Nd	$0.00934^{+0.00062}_{-0.00060} \pm 0.00022$	NEMO-3 [29]
^{238}U	2.0 ± 0.6	Radiochemical [29]

2.2 Neutrinoless double beta decay

> "Neutrinos alone, among all the known particles, have ethereal properties that are striking and romantic enough both to have inspired a poem by John Updike and to have sent teams of scientists deep underground for 50 years to build huge science-fiction-like contraptions to unravel their mysteries."
>
> *Lawrence M. Krauss*

The neutrinoless double beta decay $\left(\beta\beta^{0\nu}\right)$ was proposed in 1939 by Wendell H. Furry [33] to try to apply Majorana's postulates to neutrinos. In this decay, there would be no emission of neutrinos:

$$(Z, N) \rightarrow (Z+2, N-2) + 2e^{-}, \tag{2.2}$$

which violates the conservation of the total lepton number, in disagreement with the SM, and linked to the possibility of neutrinos being Majorana particles.

Since the energy related to the nuclear recoil is negligible in the case of the $\beta\beta^{2\nu}$ decay, the energy spectrum of the two emitted electrons is continuous. However, for $\beta\beta^{0\nu}$, it consists of a single line at $Q_{\beta\beta}$ which is at the mass difference between the parent and daughter nuclides. In figure 2.2 we can see the energy spectrum for both decays.

$$Q_{\beta\beta} \equiv M\left(Z, N\right) - M\left(Z+2, N-2\right) \tag{2.3}$$

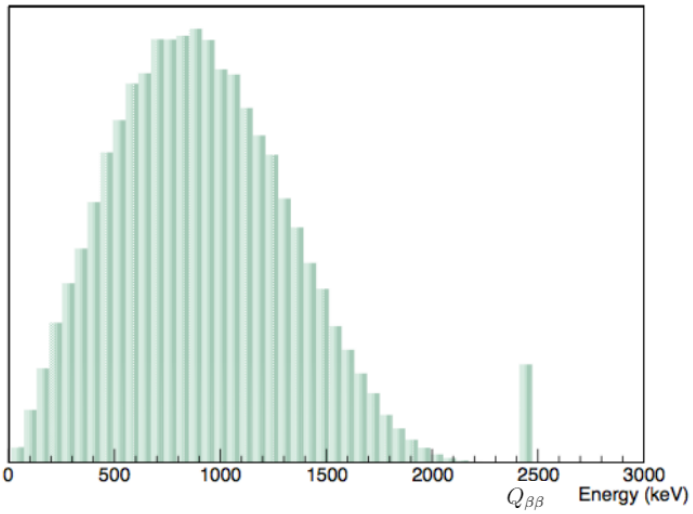

Figure 2.2: Kinetic energy distribution of the two emitted electrons in the double beta decay. The continuum spectra are events where neutrinos are involved and the peak at $Q_{\beta\beta}$, scaled to make it visible, from the neutrinoless mode [34].

The neutrinoless double beta decay can also be explained by Feynman diagrams (figure 2.3). The first nucleus emits a pair of virtual W bosons that exchange a Majorana neutrino in order to produce the electrons. [35] states the following relationship:

$$\frac{1}{T_{1/2}^{0\nu}} = G_{0\nu}\left|M^{0\nu}\right|^{2}\left(\frac{m_{\beta\beta}}{m_e}\right)^{2}, \tag{2.4}$$

where $T_{1/2}^{0\nu}$ is the half-life for the $\beta\beta^{0\nu}$ process, $G^{o\nu}$ is the phase-space factor for the emission of two electrons (analytically calculated from [36, 37]), $M^{0\nu}$ is the nuclear matrix element of the transition, which can be evaluated from [38–41], m_e is the mass of the electron and $m_{\beta\beta}$ is the effective Majorana mass of the electron neutrino, derived from equation 1.6:

$$m_{\beta\beta} = \left| \sum_{i=0}^{3} U_{ei}^2 m_i \right| \tag{2.5}$$

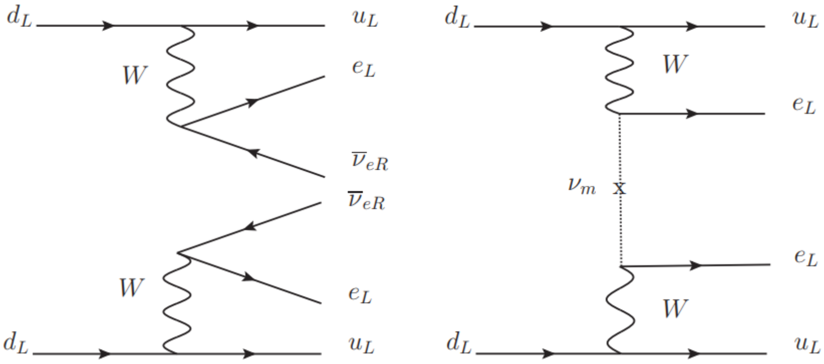

Figure 2.3: Feynman diagrams for the $\beta\beta^{2\nu}$ (left) and $\beta\beta^{0\nu}$ (right).

From both equation 2.4 and 2.5, we can infer the absolute value of $m_{\beta\beta}$ in a measurable $\beta\beta^{0\nu}$ decay, although the other parameters introduce uncertainties. On the other hand, if we do not observe a $\beta\beta^{0\nu}$ decay, an upper bound on the effective neutrino mass can be inferred.

The unknown mass ordering, discussed previously, will also introduce uncertainties, as well the unknown phases in the neutrino mixing matrix.

2.3 Experimental constraints

> “The scientist describes what is; the engineer creates what never was.”
>
> *Theodore von Kármán*

The unquestionable detection of rare double beta decays has proven to be a great challenge due to the large mass of decaying isotope needed and the very long lifetimes involved. The goal is to measure the total energy of the emitted electrons. As a consequence of the finite energy resolution of any detector, events around $Q_{\beta\beta}$ follow a Gaussian distribution centered at that value, but other processes can compromise the sensitivity of the detector.

There are several background processes that can originate an event similar to the neutrinoless double beta decay process. The first one is the intrinsic background related to the $\beta\beta^{2\nu}$ decay. This may result from measuring the energies of both emitted electrons since neutrinos are not detected. Therefore, in order to fully distinguish the energy peak of the neutrino and neutrinoless modes, a good energy resolution is essential. A careful selection and location of the used material is also necessary, to avoid other possible sources of events similar to the neutrinoless decay.

The sensitivity of a detector, in this case to $m_{\beta\beta}$, is described by the following expression:

$$S\left(m_{\beta\beta}\right) = A\sqrt{\frac{1}{\varepsilon}}\left(\frac{B\Delta E}{Mt}\right)^{1/4}, \tag{2.6}$$

where A is a constant, ε is the detection efficiency, B is the background rate around the region of interest, ΔE is the energy resolution, M is the isotope mass and t is the running time of the detector.

2.3.1 Detection efficiency

With neutrinoless double beta decay being an extremely rare decay, one of the most important features of a suitable detector is a high detection efficiency. The general rule is that, the simpler the detector, the higher the detection efficiency. For example, in detectors where the detection medium is also the double beta decay emitter, the detection efficiency is probably higher than in detectors that have different materials for detecting and emitting the decay.

2.3.2 Background

As already said, the natural radioactivity of the components of the detector is most of times the main background source. Radon, for example, an intermediate product of the uranium and thorium decays, can be a problem if the energy of its decay is close to the energy released in the double beta decay being detected. It is a noble gas, not very reactive and diffuses easily in the detector. One of the solutions is flushing the detector surroundings with pure nitrogen or installing radon traps.

The external sources of background are also a problem. The muons and neutrons hitting the Earth are an additional source of background, which can be avoided placing the experiment underground. But the natural radioactivity from underground sites will also result in gamma-rays and neutrons. This can be dealt by properly shielding the apparatus with lead, copper or water.

Other ways of reducing the background include pulse-shape discrimination, reconstruction of the event topology and detection of the event signature.

2.3.3 Energy resolution

The energy resolution measures the ability of a detector to distinguish close energy events: the better the energy resolution, the better the distinction. Searching for neutrinoless double beta decay requires a high energy resolution close to the intrinsic limit of gas detectors resolution to distinguish the event from the two neutrino double beta decay process.

2.3.4 Isotope selection

Considering the best option of having the detection medium and the radioactive source the same material, isotope selection is crucial, not only because just 35 nuclides undergo this decay, but because the half-life of the process, as seen from equation 2.4, depends on the phase-space factor $G^{0\nu}$, which in its turn varies with $Q^5_{\beta\beta}$ [36]. A good selection would be an isotope with large $Q_{\beta\beta}$, which also increases the signal to noise ratio. For this reason isotopes with $Q_{\beta\beta} > 2$ MeV are chosen.

2.3.5 Mass and exposure

Large double beta isotope source mass is required for these experiments due to the very long half-life, but not all experiments can be scaled without any constraint. One of the problems is acquiring such large mass of these rare isotopes, which require isotopic enrichment in order to obtain concentrated source masses. One possibility is using centrifugal separation [42], only feasible in elements with a stable gas compound, like xenon. This is one of the reasons xenon is a serious candidate.

2.4 Ongoing experiments

> "The proper method for inquiring after the properties of things is to deduce them from experiments."
>
> *Isaac Newton*

The most reliable limits for the neutrinoless double beta decay are summarised in table 2.2. The next subsections will describe some of the different techniques implemented as well as in the Appendix A.

Table 2.2: Best present results on $\beta\beta^{0\nu}$ decay, with 90 % CL. Adapted from [34, 43]

Isotope	$Q_{\beta\beta}$ (keV)	$T^{0\nu}_{1/2}$ (yrs)	$\langle m_\nu \rangle$ (eV)	Experiment
^{48}Ca	4267.98	$> 5.8 \times 10^{22}$	$< 3.1 - 15.4$	CANDLES [44]
^{76}Ge	2039.00	$> 3.5 \times 10^{25}$	$< 0.18 - 0.48$	GERDA-I + GERDA-II [45]
^{82}Se	2997.9	$> 3.6 \times 10^{23}$	$< 1 - 2.4$	NEMO-3 [46]
^{96}Zr	3355.85	$> 9.2 \times 10^{21}$	$< 3.6 - 10.4$	NEMO-3 [47]
^{100}Mo	3034.40	$> 1.1 \times 10^{24}$	$< 0.33 - 0.62$	NEMO-3 [48]
^{116}Cd	2813.50	$> 1.9 \times 10^{23}$	$< 1 - 1.8$	AURORA [49]
^{128}Te	866.6	$> 1.5 \times 10^{24}$	$< 2.3 - 4.6$	Geochemical [50]
^{130}Te	2527.52	$> 4 \times 10^{24}$	$< 0.26 - 0.97$	CUORE-0 [51]
^{136}Xe	2457.83	$> 1.07 \times 10^{26}$	$< 0.09 - 0.24$	KamLAND-Zen [52]
^{150}Nd	3371.38	$> 2 \times 10^{22}$	$< 1.6 - 5.3$	NEMO-3 [53]

2.4.1 CUORE

Some crystals, when cooled down up to cryogenic temperatures, are very sensitive to interactions occurring inside them, producing a temperature change proportional to the deposited energy. These devices are highly sensitive to small energy depositions. A bolometer, an example of these devices, works at low temperatures to achieve greater sensitivity. It consists of two main components: an energy absorber and a sensor. The energy of the particle is deposited in the absorber, converted into excitations (phonons) and then to a signal by the sensor.

The Cryogenic Underground Observatory for Rare Events (CUORE) is an experiment working with TeO_2 crystal bolometers to search for the neutrinoless double beta decay with ^{130}Te [54]. This technique was first used in 2003 by MiDBD experiment [55]. Then, from 2003 to 2008, CUORICINO [56] and CUORE-0 between 2013 and 2015 [57,58] have achieved the limit on the half-life of the neutrinoless double beta decay: 4×10^{24} years, with 90 % CL.

CUORE is already constructed and installed in the Laboratori Nazionali del Gran Sasso (LNGS) of National Institute of Nuclear Physics (INFN) in Italy and is the successor of the previous detectors. It consists of 988 bolometers, with a total mass of 741 kg (206 kg of ^{130}Te), organised in 19 vertical towers that will be contained in a cryostat made of six nested copper vessels, as shown in figure 2.4. It is expected that, with the sensitivity of this experiment, the half-life of the decay will reach the value of 9×10^{25} years, with 90 % CL, within 5 years of data acquisition [59,60]. In this experiment, the expected energy resolution is 0.2 % (FWHM) around the Q value of ^{130}Te (2528 keV) [61].

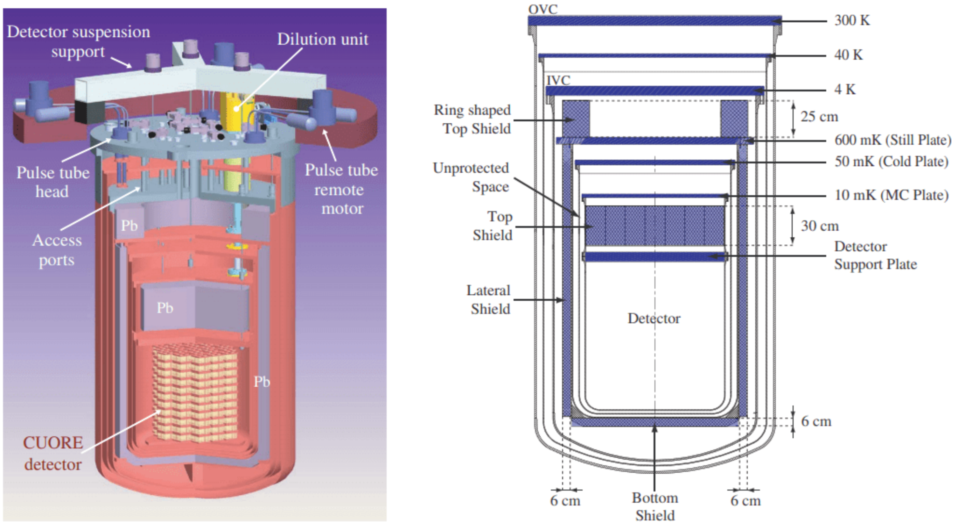

Figure 2.4: CUORE cryostat and internal shields [54].

2.4.2 EXO

The Enriched Xenon Observatory (EXO) is an experiment running since 2011 that uses liquid xenon, enriched in ^{136}Xe, to search for the neutrinoless double beta decay. The first phase of the experiment, EXO-200, uses 200 kg of xenon in a cylindrical TPC with 44 cm of height and 40 cm of diameter. By simultaneously collecting the scintillation light and charge, it is possible to measure the three-dimensional coordinates and energy of the ionisation event. In figure 2.5 we can see two cutaway views of the EXO-200 TPC setup. The current limit of the ^{136}Xe neutrinoless double beta decay half-life is set at 1.1×10^{25} years, with an exposure of 100 kg·yr, which corresponds to an upper limit on the Majorana neutrino mass of 190 - 450 meV. The energy resolution (FWHM) of this setup is 3.0 % at $Q_{\beta\beta}$ [62].

They have also been developing a multi-tonne liquid experiment called Next-generation Enriched Xenon Observatory (nEXO) [63].

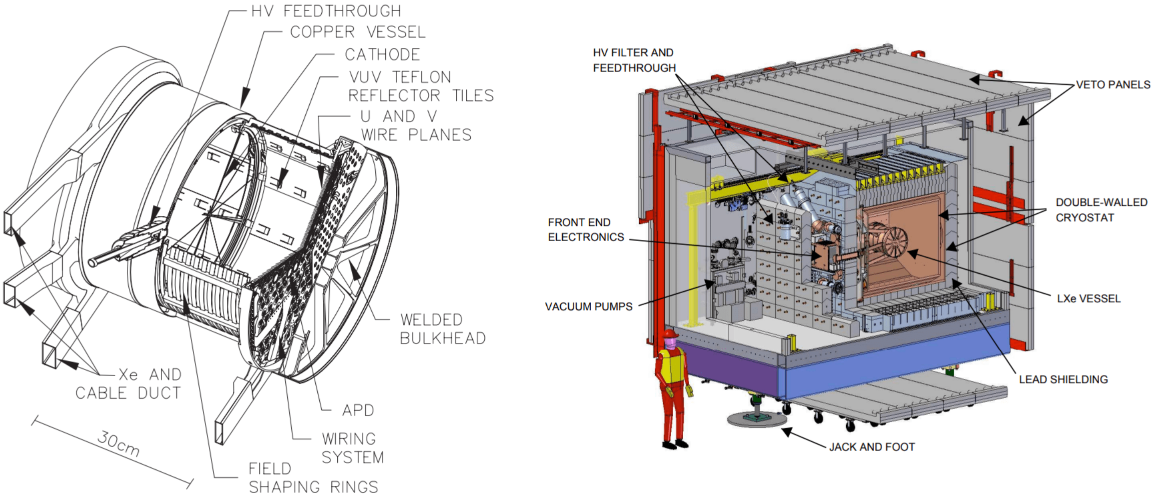

Figure 2.5: Cutaway views of the EXO-200 TPC setup. Adapted from [64].

2.4.3 GERDA and MAJORANA

The Germanium Detector Array (GERDA) is an experiment that uses germanium crystals as both source and detector [65]. These crystals are enriched to ~ 86 % of the isotope ^{76}Ge. It is mounted with strings suspended inside a cylindrical cryostat with 8.9 m of height and 4.2 m of diameter filled with 70 tons of liquid argon that acts as a shield for the external radiation and cooling device. The setup is shown in figure 2.6. The shielding from photons and neutrons is also achieved by a surrounding 590 m^3 water tank. On the top of the experiment, there are several scintillator panels and 66 PMTs [17] to detect Cherenkov light.

The Phase-I of this experiments ran from 2011 to 2013, with a total exposure of 21.6 kg·yr and an exposure-averaged energy resolution of 0.1 to 0.2 % (FWHM) at the $Q_{\beta\beta}$ value (2019 keV). The lower limit for the half-life of the neutrinoless double beta decay in this isotope was set at $> 2.1 \times 10^{25}$ years, with a 90 % CL [66]. In 2015 began Phase-II, with an upgrade that doubled the exposure, and the goal is a 10 times increase in the sensitivity and an lower limit of the half-life $> 5.3 \times 10^{25}$, with a 90 % CL [67]. In the long term a third phase is projected to use $\sim$ 1 tonne of this isotope with increased background reduction [9].

The MAJORANA experiment is similar to GERDA. It consists of a modular setup with natural (10 kg) and enriched germanium (30 kg) detectors that is surrounded by two cryostats build with ultra-pure copper. It has set a lower half-life limit of $> 2.7 \times 10^{25}$ years [68].

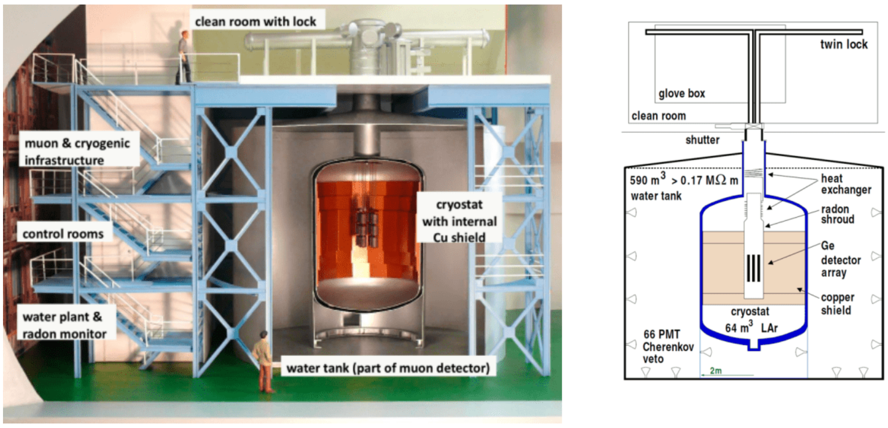

Figure 2.6: Schematic views of the GERDA setup. Adapted from [17, 69]

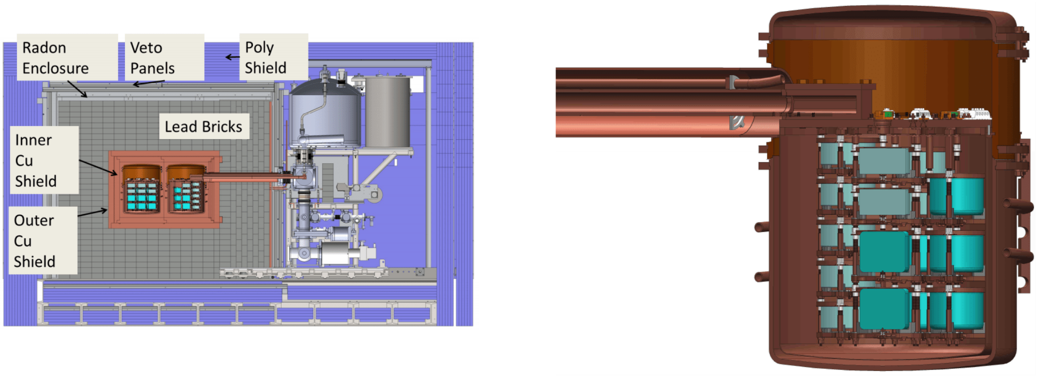

Figure 2.7: The Majorana Demonstrator as both active and passive shielding in place with an outer surface of the inner Cu shield (left) and a cross sectional view of a cryostat (right) [70].

2.4.4 KamLAND-Zen and SNO+

The KamLAND-Zen is an upgraded experiment based on the Kamioka Liquid Scintillator Antineutrino Detector (KamLAND) detector [71] located at the Kamioka mine in Japan. It uses enriched xenon dissolved in a liquid scintillator, a material that absorbs energy when a particle interacts within it and re-emits it in the form of light, proportional to the deposited energy. The schematics of the detector are shown in figure 2.8. The detector consists of two concentric and transparent balloons. The inner one contains about 300 - 350 kg of ^{136}Xe and the outer balloon contains 1000 tons of pure liquid scintillator that will act as a shield for gamma-rays.

The oil buffer, located between the outer balloon and a spherical tank, acts as a shield for external radiation.. The scintillation is recorded by 1879 PMTs that provide a 34 % solid angle coverage [17].

The first phase of KamLAND-Zen began in 2011 and the second was from 2013 to 2015, and estimated a half-life of the neutrinoless double beta decay of $> 1.07 \times 10^{26}$ years, which corresponds to a $m_{\beta\beta}$ of $< (61 - 165)$ meV [52].

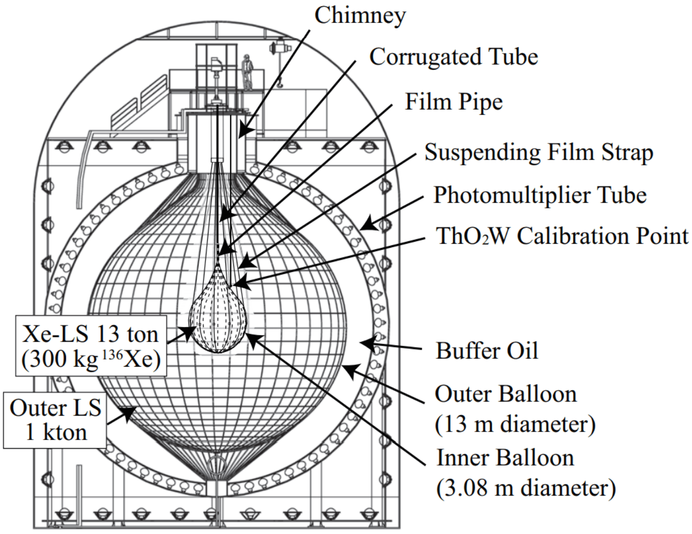

Figure 2.8: Schematic diagram of the KamLAND-Zen detector [72].

Sudbury Neutrino Observatory (SNO)+ is another liquid scintillator experiment located in Canada that uses 780 kg of isotope ^{130}Te. It consists of a 12 m diameter acrylic vessel immersed in ultra pure water, surrounded by 9500 PMTs. The first phase began in 2018, with an expected operation time span of 5 years. The expected energy resolution around the $Q_{\beta\beta}$ (FWHM) is 10.5 %, aiming to reach a half-life of $> 2 \times 10^{26}$ years, with 90 % CL, which corresponds to a $m_{\beta\beta}$ of $< (40 - 90)$ meV [73]. The detector is represented in figure 2.9.

2.4.5 SuperNEMO

Neutrino Ettore Majorana Observatory (NEMO) is an international collaboration located in France. This experiment, unlike other similar detectors, uses a different isotope as the emitter and detection medium, thus providing results with different isotopes with the same detector. It consists in 20 sectors each one consisting a thin source foil in the center surrounded by a tracker and a calorimeter.

This experiment is based on three phases: NEMO-1 and NEMO-2 were prototype detectors used until 1997, and NEMO-3 demonstrator collected data from 2003 to 2011. The best energy resolution achieved was 14 % (FWHM) [74] in NEMO-3. The detector is shown in figure 2.10.

SuperNEMO is the next upgraded version of the experiment and it is being currently assembled. Its tracking method is more accurate, which enables the detection of false-positive results and

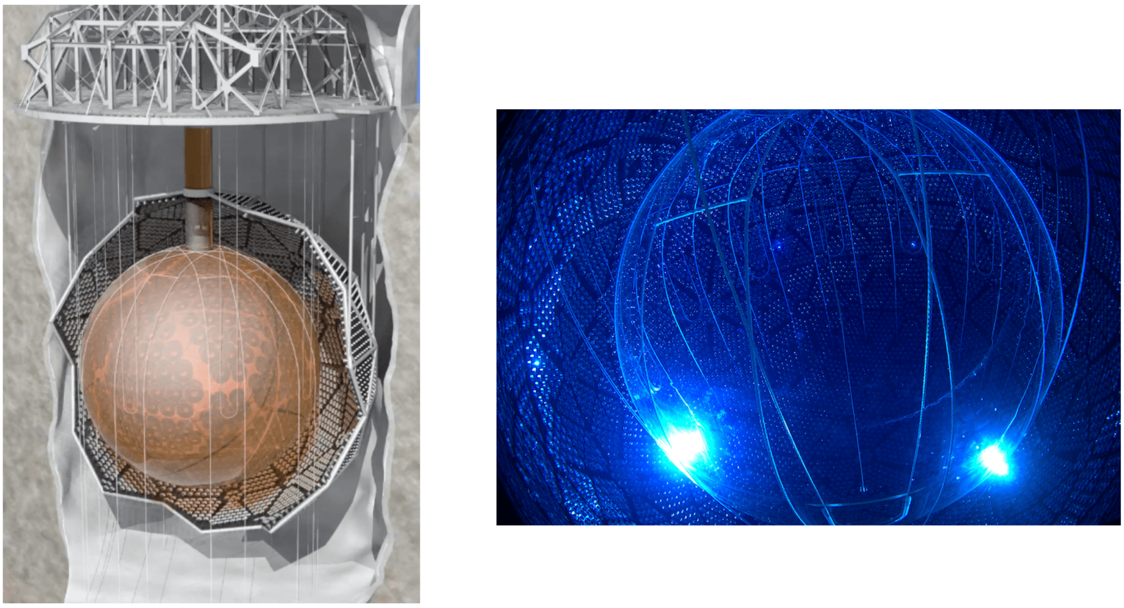

Figure 2.9: Artist's drawing of the SNO+ detector (left) and a photo of the detector (right) [73].

to discriminate different particles. It is expected that the sensitivity would be enough to achieve a lower half-life limit of $\sim 10^{26}$ years, for the neutrinoless double beta decay, with an energy resolution of 4 % (FWHM) [75].

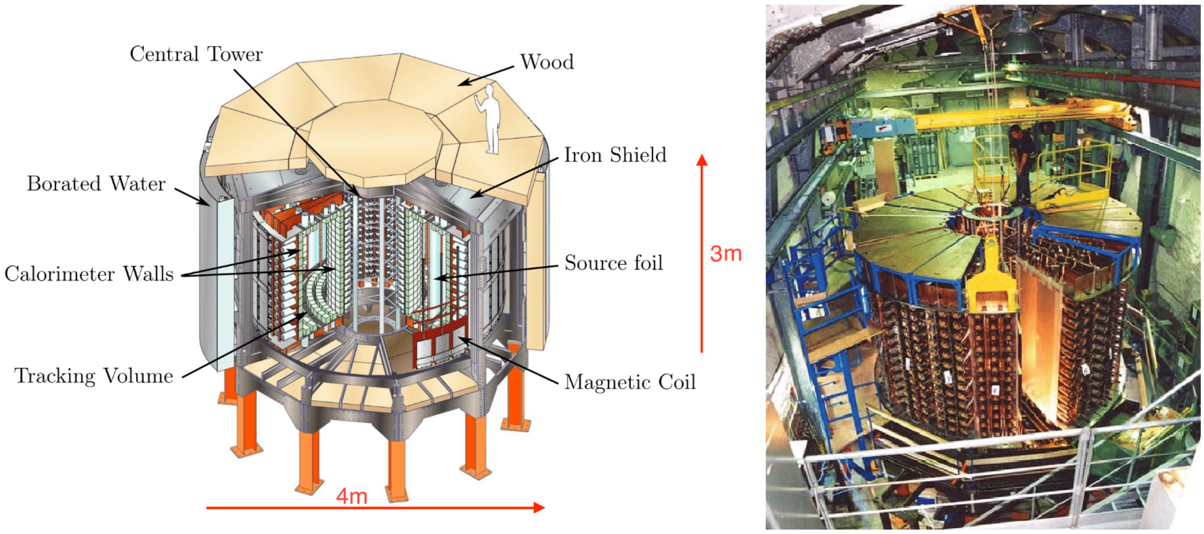

Figure 2.10: Schematics of NEMO-3 (left) and view before the installation of the last sector (right) [76].

2.4.6 PandaX

The Particle and Astrophysical Xenon Detector (PandaX) is the deepest underground detector in the world, located in China. It consists of a dual-phase TPC which allows the location of events, and uses liquid and gaseous xenon. It is dual-purpose: to search for dark matter events and to detect neutrinoless double beta decays.

The phase-I of this experiment had a total xenon mass of 400 kg, with only 125 kg sensitive mass, with 143 PMTs positioned at the top of the detector and 37 at the bottom (see figure 2.11). The phase-II increased the sensitive mass of xenon up to 500 kg. The future phase-III, beginning with a prototype with 200 kg of sensitive mass, will have 1000 kg of xenon. The expected half-life limit is $\sim 10^{27}$ years (after running 3 years), which corresponds to 20 to 50 meV of effective Majorana neutrino mass [77].

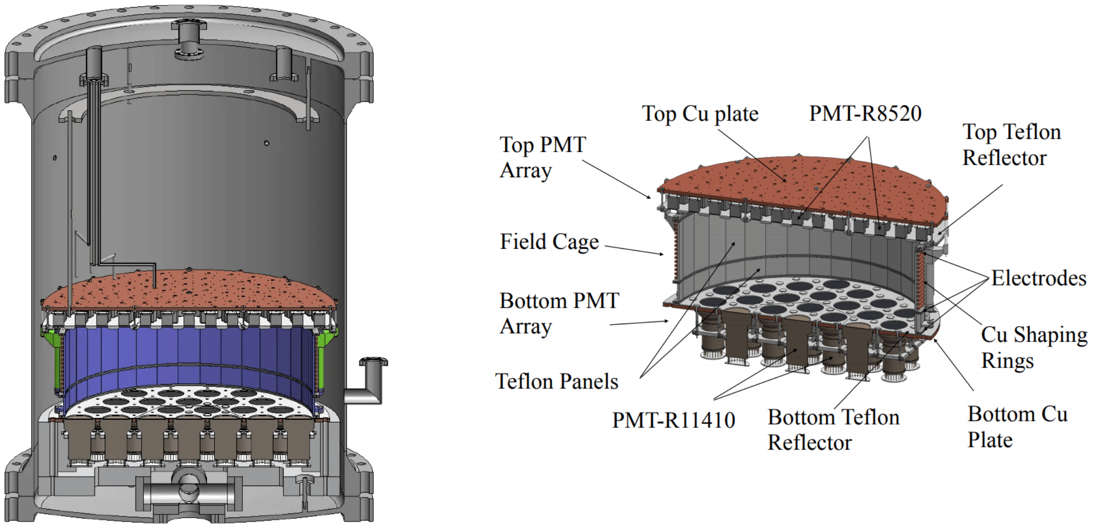

Figure 2.11: Full view of the detector (left) and cross-section of the top PMT array, the field cage and the bottom PMT array (right). Adapted from [78, 79].

Chapter 3

NEXT experiment

The Neutrino Experiment with a Xenon TPC (NEXT) is an international collaboration that uses an electroluminescent high pressure Time Projection Chamber (TPC) filled with gaseous xenon enriched in ^{136}Xe. It is located at the Laboratorio Subterráneo de Canfranc (LSC), in Spain, 850 m deep below the Tobazo Mountain.

The TPC was invented by David Nygren in the 1978 [80] and consists of a detector that combines electric and eventually magnetic fields in a gas or liquid (or both), to record a three-dimensional track of a particle by measuring the initial position of the event and the time it takes to reach one of the detector ends. When used in double beta decay experiments, usually the source and detector medium are the same to optimise the compactness, scalability and energy resolution.

3.1 Xenon as the source and filling gas

> "When I was a boy, I read with great interest but scepticism about a magic lamp which was used with success by a certain Aladdin. Today I have no scepticism whatsoever about the magic of the xenon flash lamp which we use so effectively for many purposes."
>
> *Harold Edgerton*

The isotope ^{136}Xe is widely used as a filling medium for neutrinoless double beta decay studies because:

1. It has a rather high natural abundance: ~ 9 %.
2. Isotopic enrichment is simple and cheap when comparing to other double beta decay isotopes.
3. High Q value: 2458 keV [81,82].
4. The double beta decay is slow: $T^{2\nu}_{1/2} = 2.2 \times 10^{21}$ years [71].
5. In gaseous xenon, the energy resolution can below 0.5 % (FWHM) at the Q value [83].

Electrons can undergo several processes in xenon, until they reach a sub-excitation energy (see figure 3.1). The energy deposited by any particle that interacts with xenon is divided between excitation (an electron is transferred to a higher energy state, followed by a de-excitation), ionisation (an electron is ejected from the atom, forming an electron-ion pair) and elastic collisions. The recombination of the electron-ion pairs and de-excitation both lead to the emission of scintillation photons.

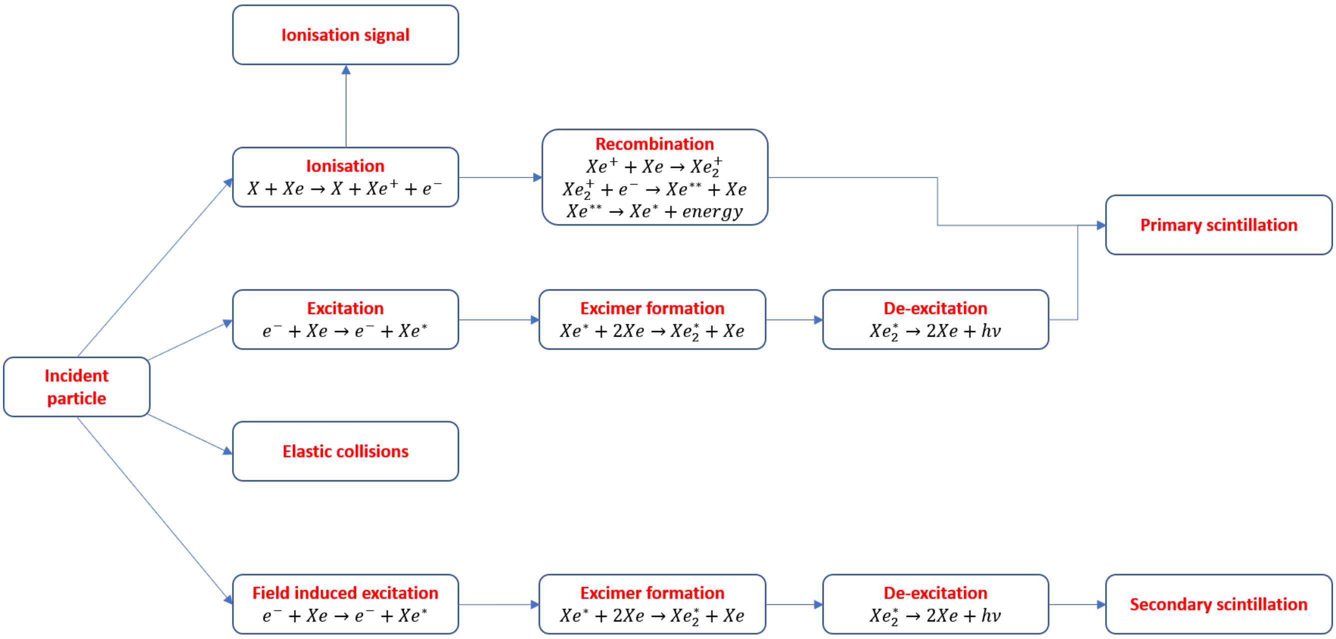

Figure 3.1: Main processes in xenon, where X stands for the ionising radiation.

We can deduce from [17] the formula for the average energy required to produce an electron-ion pair (W_i) and a scintillation photon (W_{sci}) as the following:

$$W_i \equiv \frac{E_\beta}{N_i} = \langle E_i \rangle + \langle E_{sci} \rangle \frac{N_{sci}}{N_i} + \langle \varepsilon \rangle \tag{3.1}$$

$$W_{sci} \equiv \frac{E_\beta}{N_{sci}} = \langle E_{sci} \rangle + \frac{N_i}{N_{sci}} \left(\langle E_i \rangle + \langle \varepsilon \rangle \right). \tag{3.2}$$

where E_β is the energy deposited in the gas, N_i is the number of primary electrons produced by means of an average ionisation energy $\langle E_i \rangle$, N_{sci} is the number of excited atoms with an average de-excitation energy $\langle E_{sci} \rangle$ and $\langle \varepsilon \rangle$ is the averaged kinetic energy of the thermalised electrons. In table 3.1 we can find a summary of these parameters in gaseous and liquid xenon.

To detect an ionisation signal, electrons must be guided (by an applied electric field) towards the anode. In spite of the high energy deposited, with the caveats the charge collected at the anode may not be enough to produce a good enough signal for the purpose. Moreover, during the drift process, two shortcomings may occur: the electrons can normally diffuse or can be attached by unavoidable electronegative impurities in the gas.

Table 3.1: Energy to produce an electron-ion pair (W_i) or electroluminescence photon (W_{sci}) and number of primary electrons (N_i) and photons (N_{sci}) produced with the energy for gaseous and liquid phases of Xe at $Q_{\beta\beta} = 2.458 \times 10^6$ eV. Data obtained from [84–87].

Phase	W_i (eV)	N_i (primary electrons)	W_{sci} (eV)	N_{sci} (photons)
Gaseous	21.9	1.1×10^5	39.2 ± 3.2	6.3×10^4
Liquid	15.6	1.6×10^5	13.8	1.8×10^5

The solution to this problem is amplification. In this type of gas detector two choices are available - either charge multiplication or electroluminescence (EL) production. The second method, achievable by applying a controlled electric field (above the excitation potential and below the ionisation threshold of the gas), gives the best detector performance. The electric field, between these boundaries, ensures that electrons, while gaining enough energy between collisions to excite, cannot ionise the atoms in the medium. These excited atoms undergo a de-excitation process by means of which a secondary scintillation or electroluminescence photon is emitted. Thus, the signal obtained is proportional to the incident energy, but with a gain, since one electron originates several photons during its drift in the EL region.

The absolute EL gain η, when applying a uniform and constant reduced electric field E/p in kV cm^{-1} bar^{-1}, is described by the following formula [88]:

$$\eta = 140 \cdot (E/p - 0.83) \cdot p \cdot \Delta x \qquad \left(\text{photons/e}^-\right), \tag{3.3}$$

where p is the pressure in bar and Δx is the drift path in the scintillation region, in cm. The scintillation photons emitted by noble gases are in the Vacuum Ultraviolet (VUV) region, therefore hard to detect because they are absorbed by most materials and the efficiency of detection of most sensors is poor. In order to improve detection, wavelength shifters are deposited on the surfaces of the detector to transform these photons into visible (or near-visible) more detectable light.

Ugo Fano, an Italian American physicist demonstrated in 1947 [89] that the processes that lead to the creation of ionisation pairs are not independent from one other, introducing the Fano factor F in the variance σ_i^2 of the fluctuations, that deviate from the purely statistical Poisson behaviour expected:

$$\cancel{\sigma_i^2 = N_i} \qquad \text{but} \qquad \sigma_i^2 = F N_i, \tag{3.4}$$

where N_i is the average number of produced electron-ion pairs for a certain energy. Therefore, the best energy resolution achievable (also called intrinsic resolution) is expressed as:

$$\left(\frac{\delta E}{E}\right)_{int} = 2\sqrt{\frac{2\ln 2 \cdot \; F \cdot W_i}{Q_{\beta\beta}}}, \tag{3.5}$$

with $F < 1$ for noble gases. From the experimental study in [90], the Fano factor for High Pressure Gaseous Xenon (HPXe) is:

$$F_{HPXe} = 0.170 \pm 0.007 \tag{3.6}$$

As for liquid xenon (LXe), the initial predictions in 1976 [91] stated that the $F_{LXe} \approx 0.05$, but recent experiments in 2003 [92] showed that:

$$F_{LXe} \approx 20, \tag{3.7}$$

mostly due to the many inelastic collisions in the high density liquid phase. From these results, we can calculate the numeric value of the intrinsic resolution for both phases:

$$\left(\frac{\delta E}{E}\right)_{int_{HPXe}} \approx 0.27\,\% \;\; \text{(FWHM)} \tag{3.8}$$

$$\left(\frac{\delta E}{E}\right)_{int_{LXe}} \approx 2.35\,\% \;\; \text{(FWHM)}\,, \tag{3.9}$$

which is clearly better for HPXe, although it has a higher W_i value. In fact, all detectors are also affected by losses, noise and fluctuations, which introduce another factor G in the real energy resolution expression:

$$\frac{\delta E}{E} = 2\sqrt{\frac{2\ln 2 \cdot \;(F+G)\cdot W_i}{Q_{\beta\beta}}} \tag{3.10}$$

3.2 SOFT as the working principle

“The evolution of the TPC ideas followed a somewhat more tortuous path than could be presented in this article (...).”

David Nygren, in the TPC conception paper of 1978

In the NEXT cylindrical TPC filled with gas, a voltage is applied across the top and bottom surfaces, producing a uniform electric field. The primary electrons generated due to the ionising radiation are guided towards the anode. Their two-dimensional track is recorded in a readout plane and the transverse coordinate is obtained from the time of arrival, thus this detector allows for a three-dimensional track reconstruction and energy deposition pattern (dE/dx).

SOFT stands for Separated Optimised Function TPC and the concept is shown in figure 3.2. In this approach, the energy and tracking information is obtained from different planes to achieve the best possible performances in each function. The association of PMTs, which determine the time of arrival providing a trigger to the $t = 0$ of the event and the energy resolution, and the SiPMs, located after the anode, that allow a two-dimensional track reconstruction, has proven a successful arrangement in the detection of the two-blob event signature of the $\beta\beta^{0\nu}$ decay (discussed in next section), improving the background rejection.

3.3 The two-*blob* event signature

As mentioned in Section 2.2, the kinetic energies of the released electrons in the $\beta\beta^{0\nu}$ decay adds up to the respective $Q_{\beta\beta}$ value. The tracks of the electron begin at the same point and end in two *blobs*, one at each end. Figure 3.3 on the left shows the characteristic two-*blob* signature of the neutrinoless double beta decay.

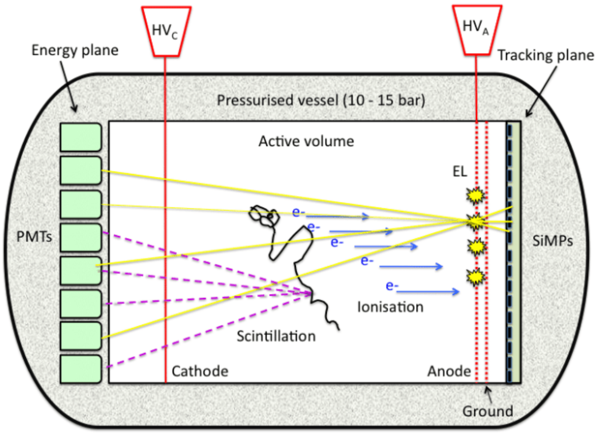

Figure 3.2: SOFT concept: the primary scintillation is recorded by PMTs in the energy plane located near the cathode and EL is recorded by several SiPMs for tracking located behind the parallel meshes and by the PMTs.

Near the $Q_{\beta\beta}$ value, the main sources of background are high-energy photons coming from the natural radioactive decays of the detector components. However, when these photons interact in the gas, they produce a track with the similar energy and length, but with only one *blob*, as can be seen in figure 3.3 on the right. This different topological behaviour allows the distinction between real signals and background events once the track reconstruction is made.

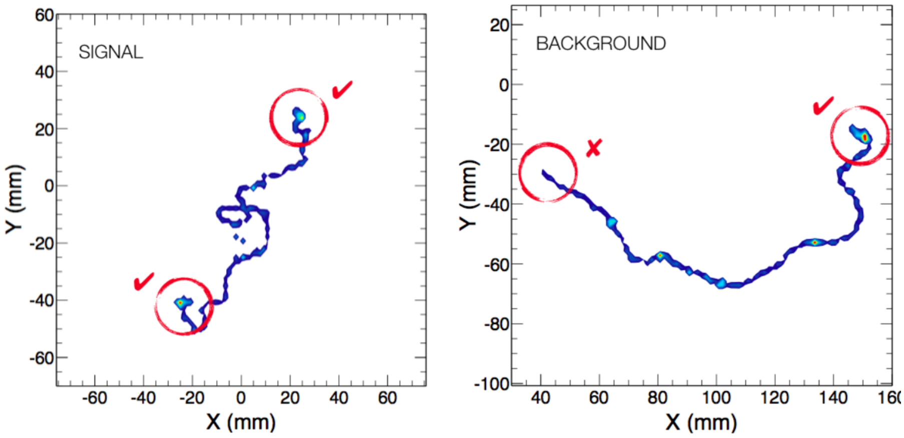

Figure 3.3: Two-*blob* signature of the $\beta\beta^{0\nu}$ decay (left) and one-*blob* signature of background events (left) in NEXT. These events were obtained using a Monte Carlo simulation in xenon at 15 bar [93].

In order to achieve a good background rejection, it is crucial to faithfully recognise the *blobs*, as the electron tracks are bended and can overlap between themselves, creating regions where the high-energy depositions can be similar to low-energy *blobs* and, for that, good spatial resolutions are essential. Above this, high-energy electrons, in their first stages of propagation, can produce secondary electrons (δ-rays) or emit *bremsstrahlung* photons that may reconvert to other electrons near the main electron track. Another challenge comes from the fact that the electrons have intrinsic transverse and longitudinal diffusions, making the tracks blurred.

3.4 Detector prototypes (2009 - 2014)

"A good scientist is a person with original ideas. A good engineer is a person who makes a design that works with as few original ideas as possible. There are no *prima donnas* in engineering."

Freeman Dyson

3.4.1 NEXT - DEMO

The first detector designed within this collaboration to prove the feasibility of the technology was NEXT - DEMO. It started running in November of 2010, at IFIC, Spain.

It consists of a cylindrical vessel with 30 cm of diameter and 60 cm of height, with a drift distance of 300 mm and an EL region of 5 mm between three grids: cathode, gate and anode. While the anode is at the ground voltage, the gate has a negative voltage to ensure an electric field in the EL region > 0.86 kV cm^{-1} bar^{-1} (excitation threshold of xenon) and the cathode is also at a negative voltage to have an electric field of 0.5 kV cm^{-1} bar^{-1} in the drift region.

Several metal rings enclose the volume and six reflecting panels are placed in these rings forming an hexagonal pattern. These panels are coated with a wavelength shifter: Tetraphenyl Butadiene (TPB). The 256 SiPMs, also coated with TPB, are placed about 5 to 10 mm away from the anode and distributed in four planes of 64 sensors each. The energy plane is placed 10 cm behind the cathode and it is made up of 19 PMTs with a quantum efficiency of 19 % in the VUV region, but higher for the wavelength shifter emission region (25 %), with a gain of 5×10^6.

Gaseous xenon is purified in a separated system that removes the electronegative impurities before and after operation and the signal acquisition and processing is done by a specially designed circuit [94]. The detector is shown in figure 3.4.

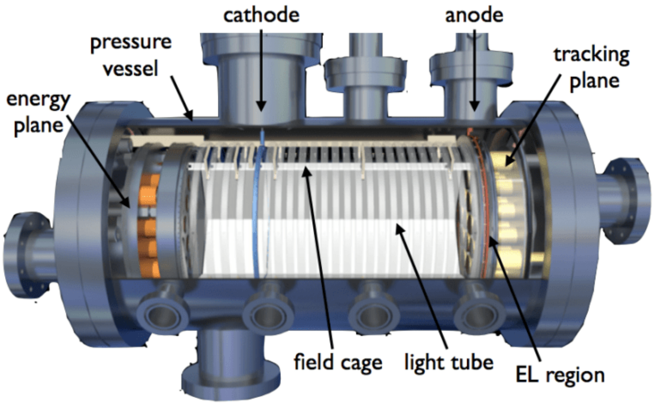

Figure 3.4: Cross-section of the NEXT-DEMO [17].

3.4.2 NEXT - DBDM

The NEXT - DBDM (Double Beta Dark Matter) was build and operated in LBNL, in the USA, and it consists of a cylindrical stainless steel vessel with 20 cm of diameter and 33.5 cm of height with a TPC and a array of 19 PMTs inside, in a hexagonal pattern. It is placed 5 cm behind the cathode. The drift region has 8 cm of length. The TPC is a hexagonal field cage, like the one shown in figure 3.5, with the faces connected through 100 MΩ resistors to produce a uniform electric field.

The vessel is connected to a gas system with constant recirculation and purification of the gaseous xenon through a hot getter to remove electronegative impurities [17].

The extrapolated energy resolution for ^{136}Xe neutrinoless double beta decays, for a $Q_{\beta\beta} = 2458$ keV, is 0.5 % (FWHM), which is very close to the intrinsic limit seen in equation 3.8 and was, at the time [95], a factor of 7 to 20 times better than other experiments using liquid xenon.

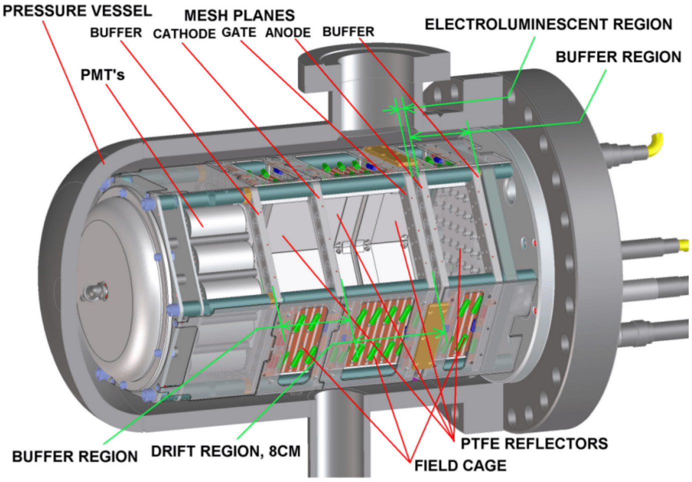

Figure 3.5: Schematic of the NEXT-DBDM prototype [96].

3.4.3 NEXT - MM

The NEXT - MM (Micromegas) was a prototype initially designed to test the possibility of using charge multiplication instead of EL with Micro-pattern Gaseous Detectors (MPGDs), but having been discarded, serves now as a detector to test novel gas mixtures for the main detector upgrades [97]. It is located in University of Zaragoza, in Spain.

Its TPC has 35 cm of drift length and 28 cm of diameter. The schematics are shown in figure 3.6, but the main differences reside in the amplification process and readout plane.

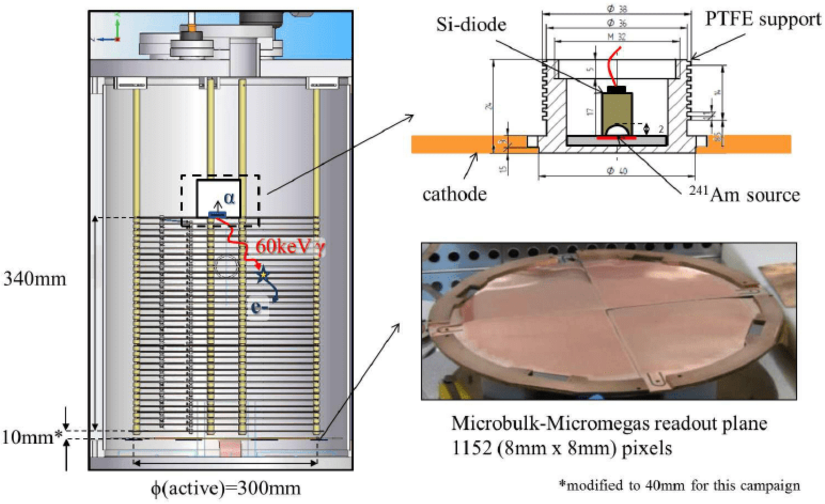

Figure 3.6: Experimental setup used for the characterisation of NEXT - MM (Micromegas) [98]

3.5 NEW (2015 - now)

The NEXT-White (NEW) began the second phase of the NEXT collaboration and it is located in LSC, in Spain. Its TPC has a length of 664.5 mm and a diameter of 522 mm [99].

The main characteristics of the detector are summarised in figure 3.7. The main body of the field cage is a cylinder made of High Density Polyethylene (HDPE) to ensure insulation between the components, and defines three regions: buffer, drift and EL region.

The drift region (cathode to gate) is the active volume of the volume and it is 52.7 cm long. The insulating shell is lined with several copper strips to help maintaining a uniform electric field. TPB lines are deposited in a teflon cylinder on the inner side of the field cage to increase the light collection efficiency.

The buffer region is 11.2 cm long and it defined from the energy plane to the cathode. Since the PMTs are very sensitive to high voltages, the buffer reduces the high voltage of the cathode to zero, in a uniform pace.

The EL gap is 6 mm long extending from the gate to the anode and was designed to withstand a maximum of 20 kV. The anode is coated with both Indium Tin Oxide (ITO) to make its surface conductive and TPB to shift the light to a more detectable wavelength.

The energy plane is made up of 12 PMTs arranged in two rings, the inner one with 3 and the outer with 9, and is placed 13 cm behind the cathode mesh. The PMTs are coupled with sapphire windows to protect them from high pressures and coupled with optical gel to ensure the matching of refraction indexes. The windows are also coated with TPB.

As for the tracking plane, it is made up of 1792 SiPMs arranged in sets of 8 x 8, with an efficiency of 50 % in the wavelength region of the TPB reemission zone, low dark count rate and high radiopurity. Each set of 8 x 8 SiPMs is connected to a kapton dice board connected to one voltage supply, ensuring similar gains to SiPMs connected to the same dice board.

The pressure vessel, seen in figure 3.7, is a cylindrical titanium-stainless steel container that can hold up to 20 bar of pressure. It is enclosed in an ultra pure copper shield.

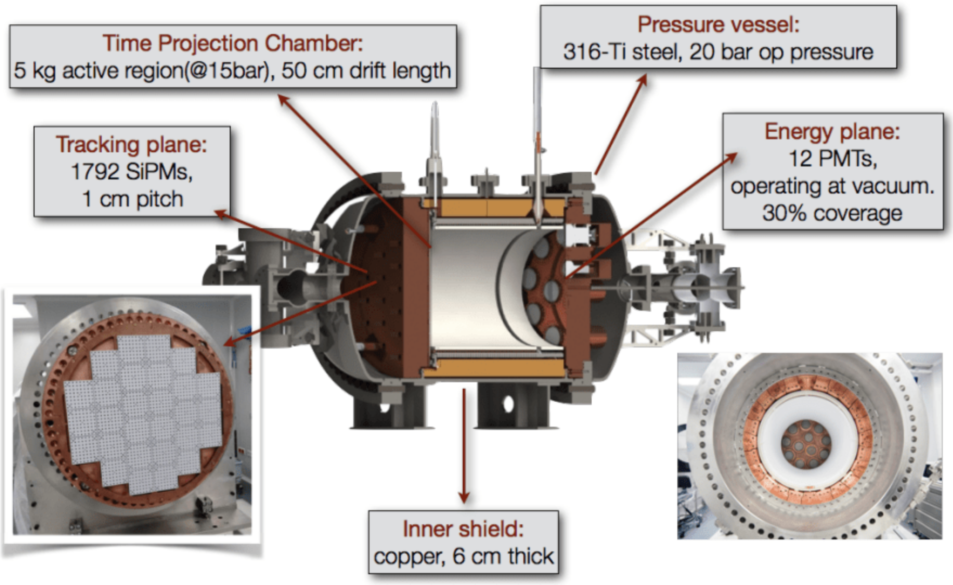

Figure 3.7: Detailed cross-section drawing of the NEW detector

Still, the detector needs to be shielded from the natural background coming from the underground laboratory. The shielding consists of lead (with an activity lower than 0.4 mBq/Kg) with 195 cm of width, 265 cm of height and 293 cm of length. The walls have a thickness of 20 cm and the total structure weights 65 tonnes. The shielding is mounted on a system of movable rails.

The gas system purifies the gas in three phases, eliminating its impurities (specially electronegative compounds such as atmospheric oxygen and carbon dioxide) and has three different phases:

1. Depressurisation in which the system is brought to a vacuum level of 10^{-5}.
2. Pressurisation and recirculation in which the detector is filled with xenon and which then is forced to circulate through cold and hot getters: the cold getters remove water and oxygen, while the hot ones remove nitrogen and methane.
3. Recovery in the case the gas needs to be evacuated. A recovery bottle is placed in liquid nitrogen and connected to the system, creating a gradient of pressure allowing for a slow recovery of the gas. There is also a connection to a expansion tank in case of an emergency.

3.6 NEXT - 100 (202x - ...)

NEXT - 100 is the final demonstrator for the goal of the NEXT collaboration: building a 1 tonne scale detector. It was proposed in 2009 [17, 100], the detector design was revealed in 2011 [101] and endorsed in a final version in 2012 [102]. It shares most of the technology and design from NEW. A cross-section of the detector is shown in figure 3.8 on the left side.

The cylindrical field cage has 107.5 cm of inner diameter, 148 cm of length and its walls are 2.5 cm thick to ensure electrical insulation. Like in NEW, copper rings are used to shape the electric field and a TPB deposit helps to improve the light collection efficiency. A window with 1 cm of thickness is placed at one of the ends of the cylinder and its inner surface acts as the TPC anode since it has ITO and TPB, as previously mentioned.

The cathode and the EL gate, built with a high-transparency stainless steel mesh, are, respectively, 106.5 and 0.5 cm from the anode. The electric field in the drift region is 0.3 - 0.5 kV cm^{-1} and in the EL gap 2 - 3 kV cm^{-1}.

The energy plane, shown in figure 3.8 on the right side, consists of 60 PMTs behind the cathode, covering 30 % of its area. The quantum efficiency of the PMTs is above 30 % for the region of interest. The windows of the PMTs are 5 mm thick, silver brazed and optically coupled to the PMTs using an optical gel to ensure the same refraction indexes. The external surface of the windows are also coated with TPB.

The total number of SiPMs in the tracking plane is 7168, distributed in 112 kapton boards in sets of 8 x 8 per circuit board.

The pressure vessel has 136 cm of inner diameter, 160 cm of length and 1 cm wall thickness, with two torispherical heads with the same diameter and thickness as the body, but with 35 cm of height. It is made up of Type 316Ti stainless steel ensuring low level of radioactivity. An inner copper shield 12 cm thick reduces by three orders of magnitude the gamma radioactivity in the vessel. The gas system is very similar to the previous demonstrator, with a few technical upgrades, as well as an external lead shield.

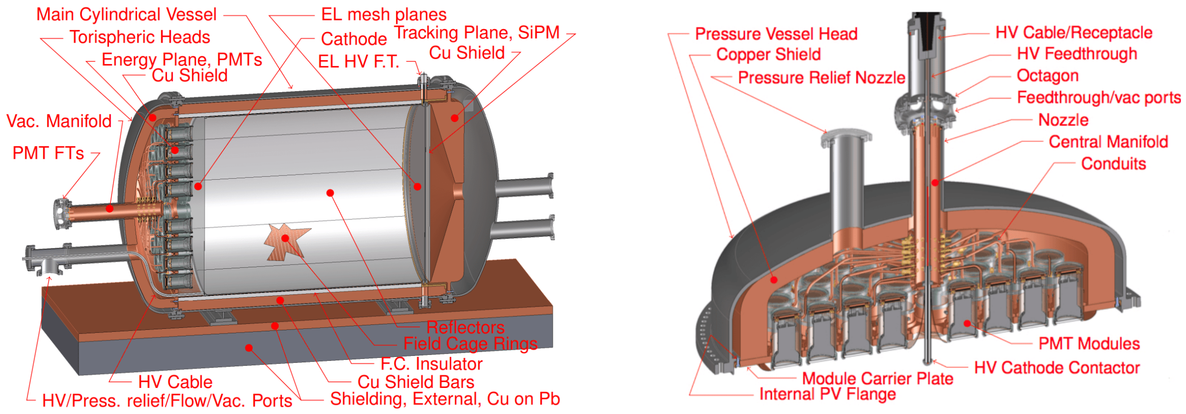

Figure 3.8: Detailed cross-section of the NEXT-100 detector (left) and energy plane (right) [102].

3.7 Expected sensitivity of NEXT-100

The total background rate estimated for this detector is:

$$< 4 \times 10^{-4} \text{ counts keV}^{-1} \text{ kg}^{-1} \text{ year}^{-1} \tag{3.11}$$

which comes mostly from detector components (the other sources contribute with at least one order of magnitude less).

The sensitivity to the half-life and effective neutrino mass, with 90 % CL, is shown in figure 3.9, left side, as a function of the exposure, assuming a 28 % signal detection efficiency. On the right side, the sensitivity is shown as a function of the background rate, for an exposure of 275 kg· yr.

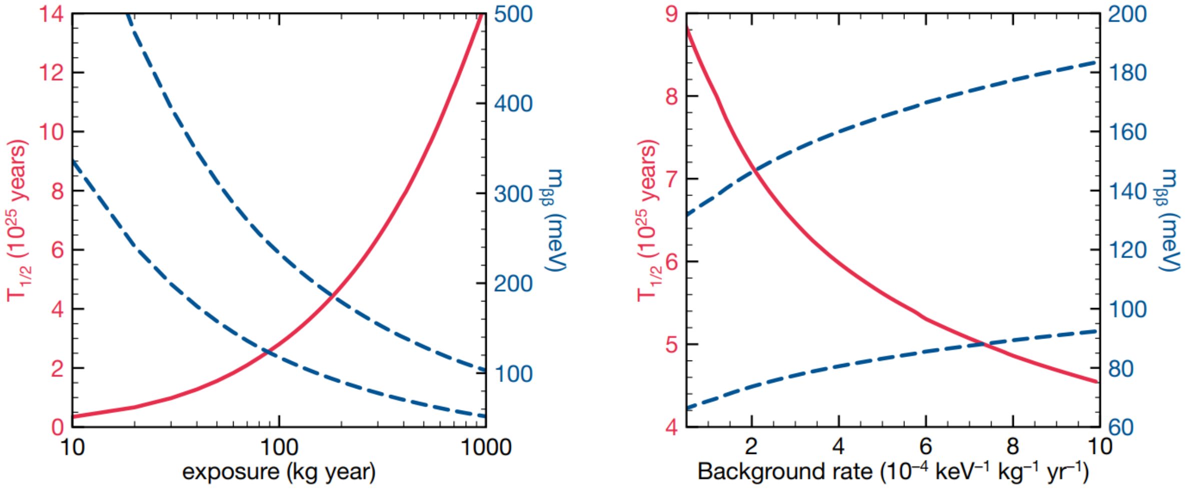

Figure 3.9: Sensitivity for the NEXT-100 to $\beta\beta^{0\nu}$. The red solid curves represent the half-time sensitivity. The dashed curves correspond to the largest and smallest estimates: the left in terms of the accumulated exposure for an estimated background rate of 4×10^{-1} counts (keV^{-4} kg^{-1} yr^{-1}) and the right is after an effective 3-year run (equivalent to an exposure of about 275 kg·yr) as a function of the achieved background rate [103].

With the background rate presented in equation 3.11, the detector is expected to reach a half-life sensitivity of 2.8×10^{25} years, for an exposure of 100 kg· yr, or 6.0×10^{25} years after 3 running years. This results in an effective neutrino mass of 80 - 160 meV [103].

3.8 NEXT - ton (future)

The NEXT - ton is the final goal and prime jewel of the collaboration. It is still in the planning phase, but some information on it has already been disclosed in [104]. There are two phases working in parallel.

The first one is improving the previous technology, by enhancing the energy resolution and topological signature, removing the PMTs and use large SiPMs in the energy plane, with a potential background reduction by cooling the detector.

The second phase is focused on the tracking and energy measurement around the anode and on the implementation of a barium tagging system on the cathode. The idea is tagging a barium ion via fluorescence every time one is produced from ^{136}Xe double beta decay. This would allow to reject all backgrounds produced by gamma rays.

The expected sensitivity, with 90 % CL, is shown in figure 3.10. From the phase 1, the expected background rate is 2.59×10^{-2} cts keV^{-1} ton^{-1} year^{-1}, whereas from the phase 2 it is expected to be virtually zero.

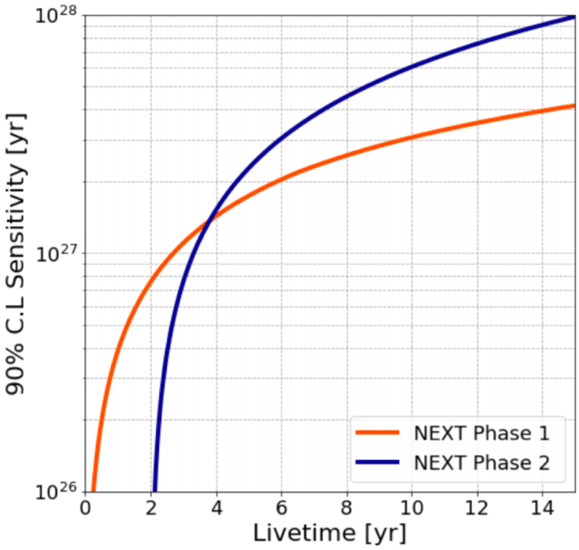

Figure 3.10: Expected sensitivity for both phases of the development, as a function of the detector's running time [104].

Chapter 4

The NEXT-DEMO++

The NEXT-DEMO prototype, described in Subsection 3.4.1, which was essential during the first phase of the project, was remodelled during 2018 to provide an ideal test-bench to develop future NEXT detectors, giving way to the new NEXT-DEMO++. In particular, this detector was designed to study several gas mixtures that could potentially reduce the diffusion of the electrons during their drift towards the anode. In addition, as the NEXT-DEMO++ uses the same sensors as NEW and NEXT-100 it is currently a perfect prototype to fine-tuning the current design of the NEXT-100 detector.

4.1 Detector overview

The detector is located in a clean-room at the laboratories of IFIC, in Valencia.

Figure 4.1: NEXT-DEMO++ detector at the laboratories of IFIC.

4.1.1 Energy plane

The NEXT-DEMO++ energy plane consists of 3 *Hamamatsu R11410-10* PMTs [105], the same model as in NEW and NEXT-100. Their increased radiopurity makes them suitable for experiments that require low background. They are placed in a stainless steel plate with 3 copper windows surrounded with brazed sapphire windows that cover the apertures. The optical coupling of the PMTs to the sapphire windows is made using *Nusil LS1-3252*. In addition, the sapphire windows are coated with TPB in order to improve the light collection efficiency and with a conductive layer of ITO to electrically protect the PMTs from the electric field in the TPC. The energy plane of NEXT-DEMO++ is shown in figure 4.2, on the left side. On the right side, it is shown the quantum efficiency of the PMTs as a function of the wavelength. The TPB coating allows an improvement on the light detection efficiency through the quartz windows.

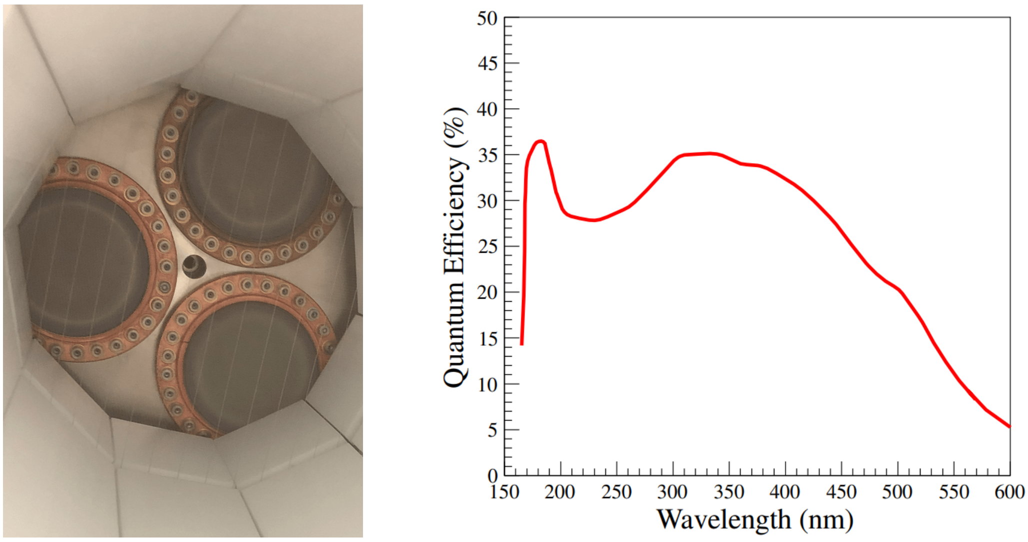

Figure 4.2: Closer look at the energy plane (left) and quantum efficiency as a function of the wavelength for the PMTs obtained in [106].

4.1.2 Tracking plane

The NEXT-DEMO++ tracking plane is composed of 4 *kapton* boards named dice boards, and each board is a 8 × 8 array of SiPMs (*SensL MicroFC-10035-SMT-GP*), resulting in a total number of 256 sensors in the tracking plane, each with 1 mm^2 active area and a pitch of 1 cm. The SiPMs are placed at a distance of $\sim$ 3 mm from the anode. The dice boards are covered by PTFE masks in order to improve the reflectivity of the sensors and light collection efficiency.

4.1.3 Field cage

The field cage is used to ensure the uniformity of the electric field that guides the electrons away from the interaction point. This electric field needs to be strong enough so electron recombination is negligible. Moreover, the drift field should be homogeneous to avoid electron loss to the vessel walls.

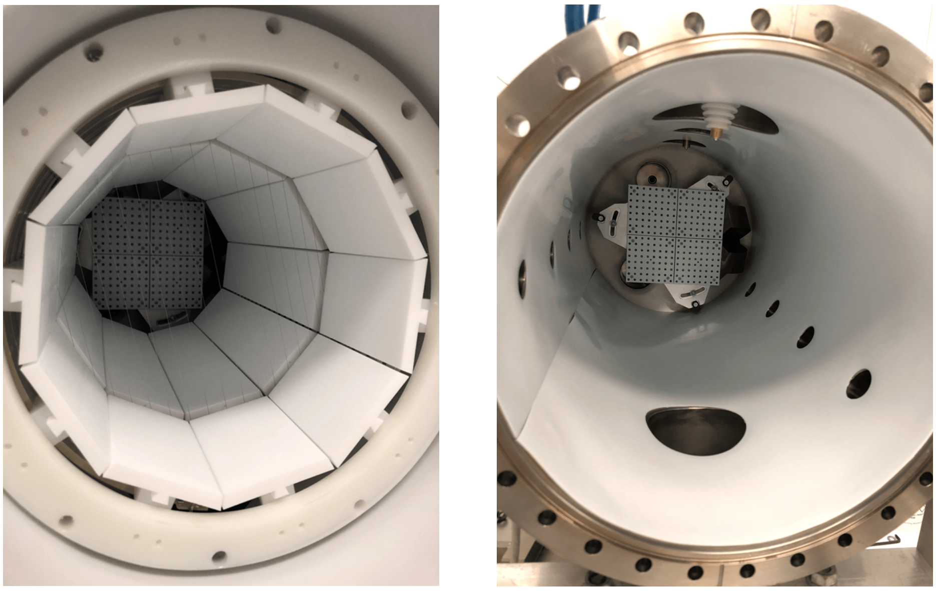

Figure 4.3: Closer look of the 4 dice boards where 256 SiPMs are placed. The HDPE is also used to electrically isolate the inner region of the vessel and it is coated with TPB to further improve the light collection efficiency.

The field cage is divided into 2 sections: buffer (between the PMTs and the cathode) and drift (between the cathode, anode and the gate), with 4 and 19, respectively, uniformly distributed aluminium rings. The rings are held in place by HDPE pillars that hold the reflective panels. Connecting the rings are also 2 sets of resistor chains of the model *Ohmite HVF 2512*, making the electrical potential drop uniform between them. For the case of the buffer section, the total resistance is 4.5 GΩ and it is shared between 9 resistances in parallel-series configuration, while for the case of the drift section is 10 GΩ and it is shared between 20 resistances in series. The field cage is shown in figure 4.4 and the individual resistor chains are shown in figure 4.5.

4.1.4 Cathode

The cathode of NEXT-DEMO++ is a stainless steel grid with a high transmission of the EL light where the voltage is the highest, assuring an electric field towards the gate but also a strong electric field between energy plane and cathode. In order to gradually decrease it, the buffer region is set so that the voltage at the PMTs windows is almost null. The cathode grid is shown in figure 4.6 on the left picture.

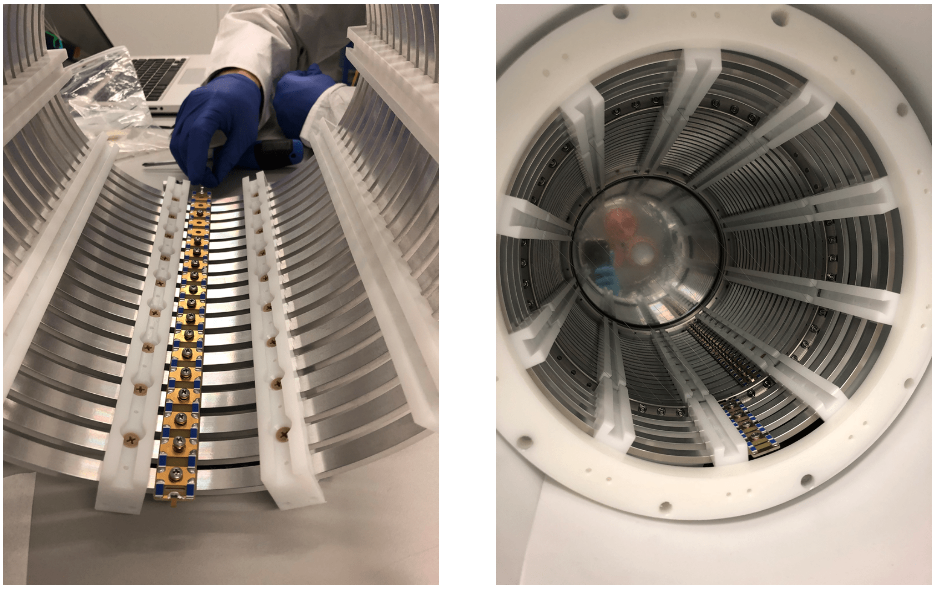

Figure 4.4: Copper rings for the drift section attached to the resistor chain (left) and field cage installed inside the vessel (right).

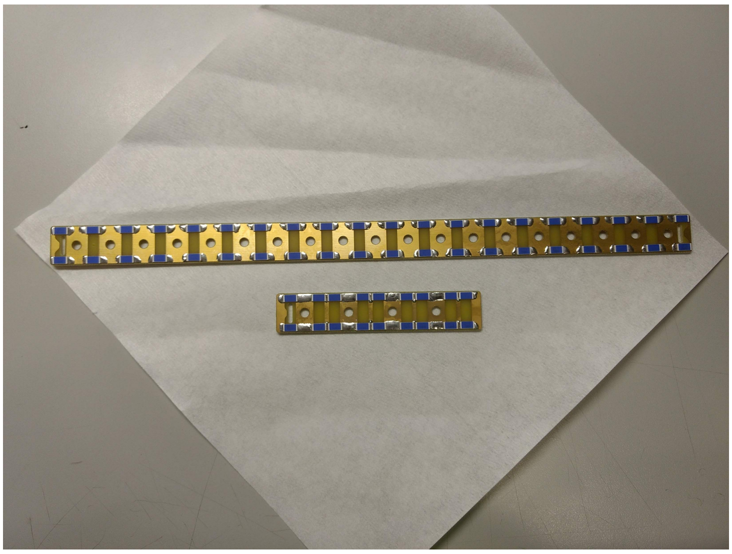

Figure 4.5: Resistor chains used in the field cage of NEXT-DEMO++.

4.1.5 EL region, gate and anode

The gate and the anode are a combination of an stainless steel mesh and a crystal plate coated with ITO and TPB on top. The anode conductive coating allows for a high transparency $\sim 90\ \%$ [107] and the possibility of applying a voltage to the surface of the plate to create an electric field in the EL region. The TPB shifts the VUV light from xenon EL to a more convenient wavelength (in the blue region) to be detected by the tracking plane. The crystal plate protects the tracking plane from sparks. The gate mesh and the anode glass plate are shown in figure 4.6

on the middle and right picture, respectively. The anode is at ground potential, while the gate is at a varying voltage to produce the desired EL electric field that will depend on the pressure and the width of the EL region.

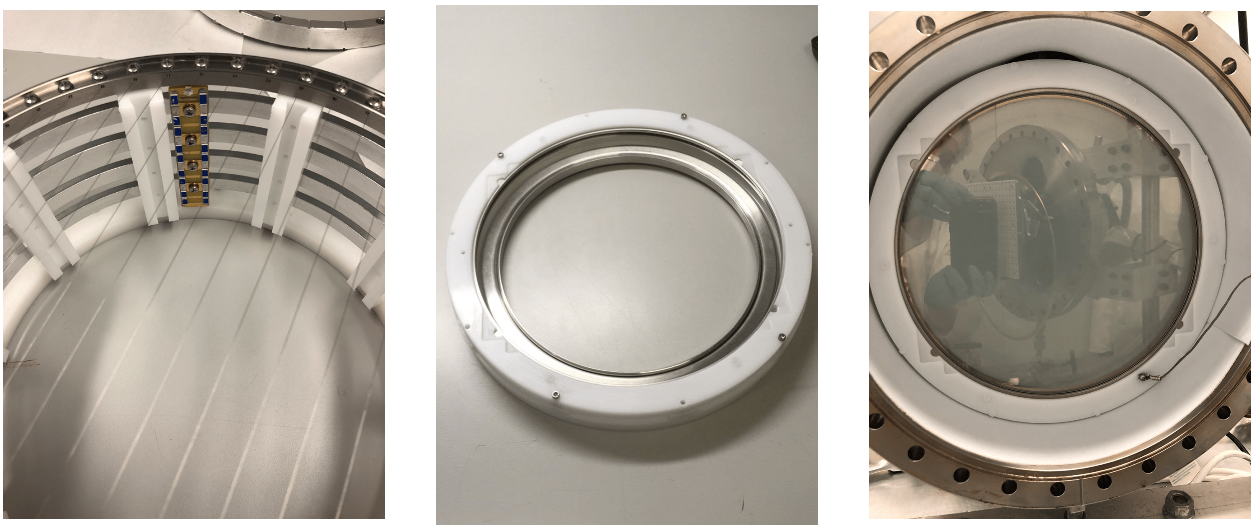

Figure 4.6: Closer look of the cathode grid (left), gate mesh (center) and the anode glass plate (right).

4.1.6 Gas system

The main goal of the gas system is to purify the xenon gas by removing electronegative impurities like O_2 and CO_2 that may be present in the gas, and recirculate it. If not removed, the electrons coming from gas ionisation may attach to these impurities and reduce the electron collection efficiency of the detector. The schematic of the gas system is shown in figure 4.7. Some important details deserve being acknowledged, namely:

- **Position of the rubidium source**: the rubidium source is placed inside the gas system and, when the gas flows through that section, krypton flows also with the gas, which is optimal to have an homogeneous distribution of decays.
- **Hot getters**: a getter is a reactive material that is placed in a vacuum system to remove certain types of atoms/molecules from it. It is used to remove impurities that come within the gas or from the vessel walls of a detector that would otherwise compromise the results. This removal may be done due to a chemical process or simply by adsorption.
- **The Residual Gas Analyser (RGA)**: this mass spectrometer monitors the existence of impurities in the gas.

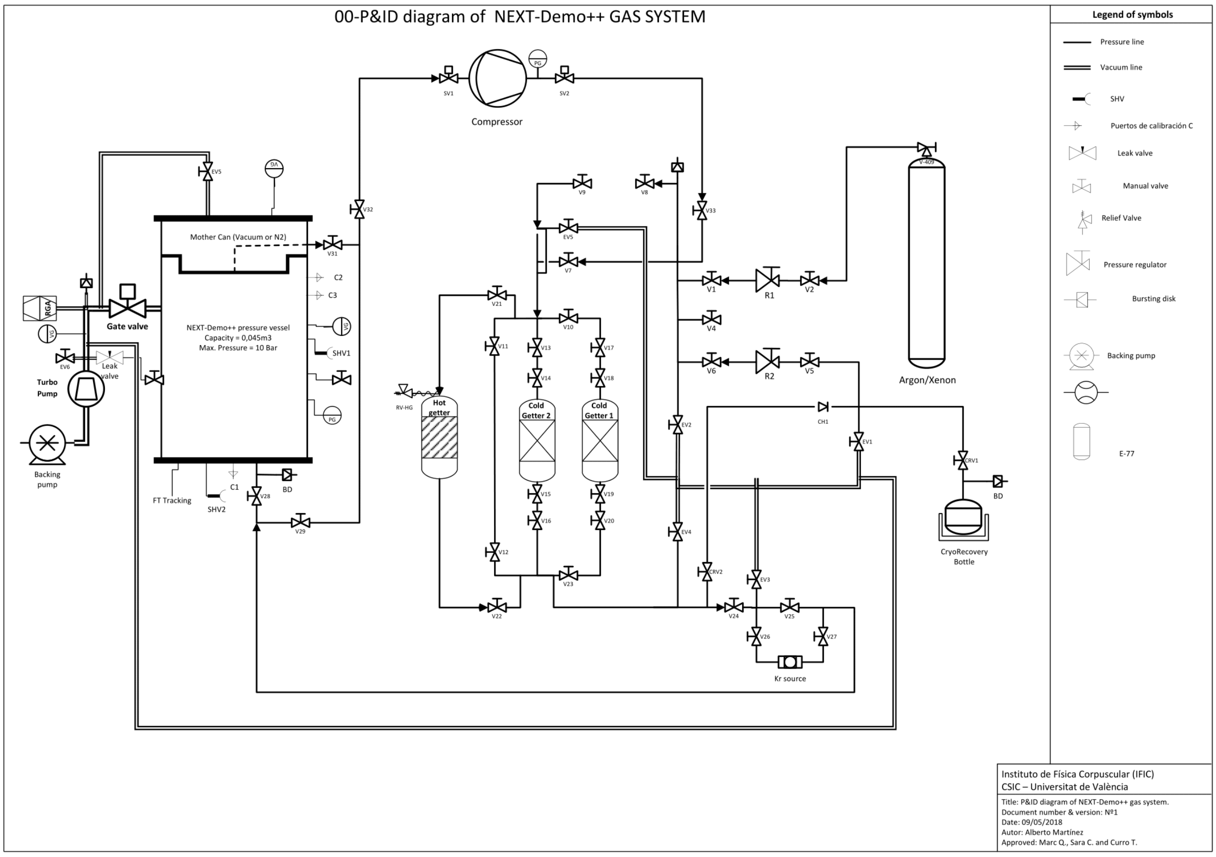

Figure 4.7: Gas system schematic of NEXT-DEMO++.

4.2 Slow controls

The NEXT-DEMO++ detector can be fully operated remotely by 3 main control systems, namely:

- **Gas system**
- **Sensors**
- **High voltage (cathode and gate)**

4.2.1 Gas system

The gas system control is automated using *CompactRIO*, a real-time embedded industrial controller made by *National Instruments* that runs in *LabVIEW*. It is a combination of a real-time controller, reconfigurable IO Modules, FPGA module and an Ethernet expansion chassis. It controls several monitoring devices like pressure and vacuum gauges, valves and the compressor, generating alarms and reports. The display interface of the gas system control is shown in figure

4.8. In this interface, we can check the pressure values of the different pressure gauges, as well of the vacuum gauges. Moreover, as a safety measure, a minimum value for the pressure gauges can be applied. We can also check the state in which the gas system is: purification state or recirculation, and also commute between them. Another relevant information we can check is the state of the compressor.

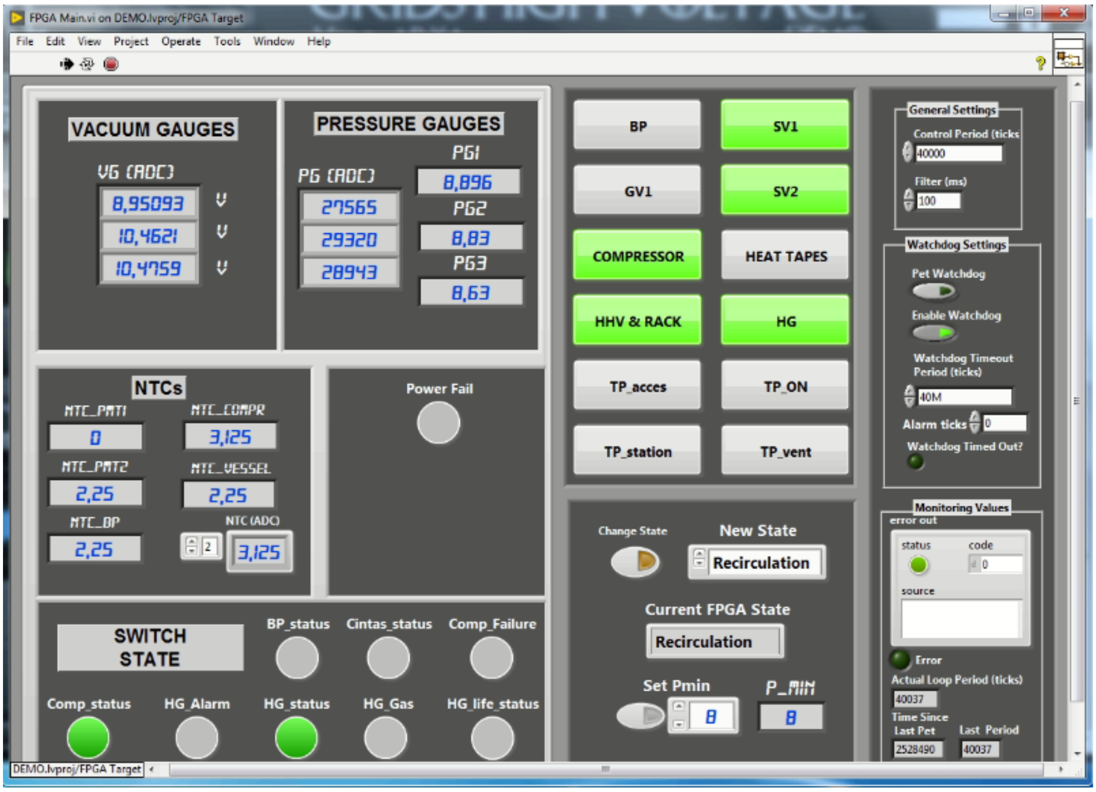
FPGA Main.vi on DEMO.lvproj/FPGA Target

VG (ADC): 8,95093 V; 10,4621 V; 10,4759 V

PG (ADC): 27565; 29320; 28943

PG1: 8,896

PG2: 8,83

PG3: 8,63

NTC_PMT1: 0

NTC_COMPR: 3,125

NTC_PMT2: 2,25

NTC_VESSEL: 2,25

NTC_BP: 2,25

NTC (ADC): 2; 3,125

New State: Recirculation

Current FPGA State: Recirculation

Set Pmin: 8

P_MIN: 8

Control Period (ticks): 40000

Filter (ms): 100

Watchdog Timeout Period (ticks): 40M

Alarm ticks: 0

code: 0

Actual Loop Period (ticks): 40037

Time Since Last Pet: 2528490

Last Period: 40037

DEMO.lvproj/FPGA Target

Figure 4.8: *LabVIEW* of the gas system display slow controls for NEXT-DEMO++.

4.2.2 Sensors

Both tracking and energy plane power supplies are monitored and controlled by custom *LabVIEW* applications, which continually check the proper voltage and current consumption of each of the PMTs and dice boards. In figures 4.9 and 4.10 it can be seen the front panel of both applications, where the former controls the SiPMs bias supplies among other electronic power supplies, while the later is exclusively dedicated to the PMTs power monitoring and control.

The voltage applied to the individual dice boards and also their current and temperature of operation is also shown on the right panel of figure 4.9. On the bottom right panel there is the option to turn on or off all or any combination of dice boards. On the left panel are shown the state and voltages of the several power supplies and front-end and as well the option to turn on or off the electronics of these sensors. On the top panel there is a safety mechanism that only allows interaction with the slow controls with password access.

As seen in figure 4.10, the state of each of the PMTs can be checked and controlled through the left panel which allows the setting of the voltage of operation. On the right panel there is the representation of the voltage (top) of each of the sensors and of the current (bottom). A password is also needed to access these slow controls.

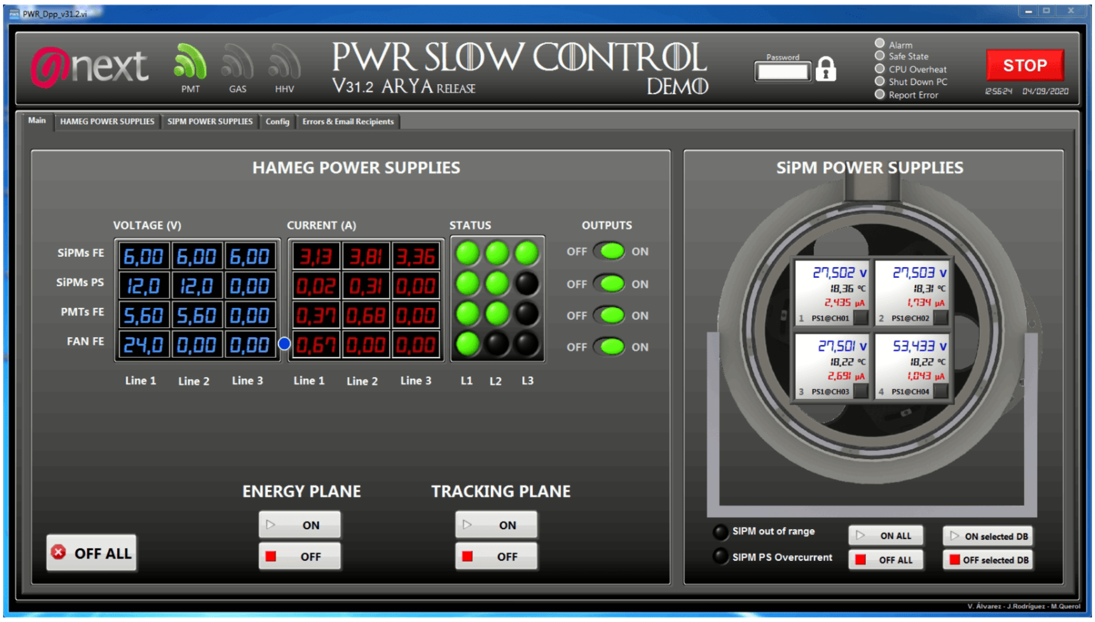

	VOLTAGE (V) Line 1	Line 2	Line 3	CURRENT (A) Line 1	Line 2	Line 3
SiPMs FE	6,00	6,00	6,00	3,13	3,81	3,36
SiPMs PS	12,0	12,0	0,00	0,02	0,31	0,00
PMTs FE	5,60	5,60	0,00	0,37	0,68	0,00
FAN FE	24,0	0,00	0,00	0,67	0,00	0,00

1 PS1@CH01: 27,502 V, 18,36 °C, 2,435 µA
2 PS1@CH02: 27,503 V, 18,31 °C, 1,734 µA
3 PS1@CH03: 27,501 V, 18,22 °C, 2,691 µA
4 PS1@CH04: 53,433 V, 18,22 °C, 1,043 µA

Figure 4.9: SiPMs display slow controls of NEXT-DEMO++.

	Set (V)	Voltage (V)	Current (uA)	Trip
PMT 1	1230	1229,0	33,0	○
PMT 2	1230	1230,0	33,0	○
PMT 3	1230	1230,0	33,0	○

Figure 4.10: PMTs display slow controls of NEXT-DEMO++.

4.2.3 High voltage (cathode and gate)

As explained in the last section, the anode is at ground potential, so there is no need for a slow control. The gate and the cathode are supplied with a negative voltage carefully calculated to achieve a sufficiently strong electric field in the drift region to avoid recombination and enough scintillation in the EL region.

The slow control display for the gate (left) and cathode (right) is shown in figure 4.11. In each display, for each component, a voltage can be set and increased over time, and also both voltage and current can be monitored. A complete list of the events is shown on the bottom panel and, as for the other slow controls, a password is needed to operate the power supplies. This particular slow control software is a test-bench for the next NEXT detectors. When a certain critical event is detected, an email is sent to a centralised email describing the event and the measures taken. For example, if a spark is detected, the software tries to restore the voltage previously set. If there are more sparks, the software, for safety, turns off the voltages applied to the gate and cathode in order to protect the detector but, most important, the sensors.

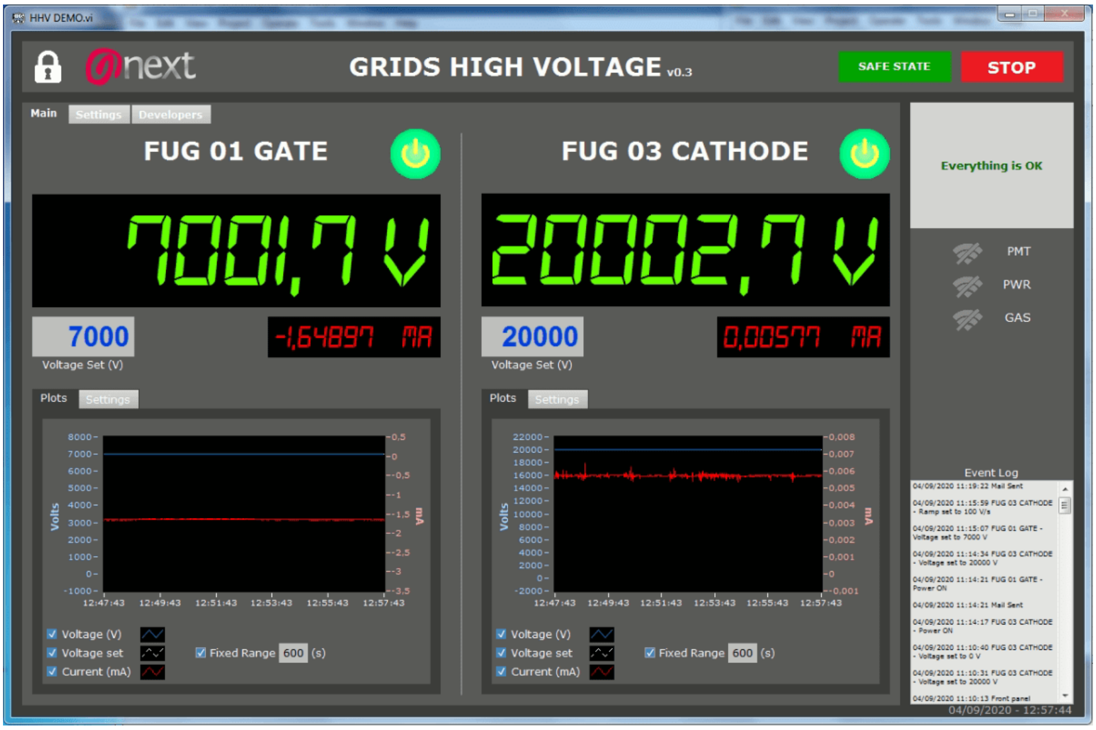

```
04/09/2020 11:19:22 Mail Sent
04/09/2020 11:15:59 FUG 03 CATHODE - Ramp set to 100 V/s
04/09/2020 11:15:07 FUG 01 GATE - Voltage set to 7000 V
04/09/2020 11:14:34 FUG 03 CATHODE - Voltage set to 20000 V
04/09/2020 11:14:21 FUG 01 GATE - Power ON
04/09/2020 11:14:21 Mail Sent
04/09/2020 11:14:17 FUG 03 CATHODE - Power ON
04/09/2020 11:10:40 FUG 03 CATHODE - Voltage set to 0 V
04/09/2020 11:10:31 FUG 03 CATHODE - Voltage set to 20000 V
04/09/2020 11:10:13 Front panel
```

Figure 4.11: High voltage display slow controls for the gate (left) and cathode (right) of NEXT-DEMO++.

Chapter 5

Data processing algorithms

In this chapter we go through a summary of the data processing algorithms used in the NEXT experiment, although the detail of them is not in the scope of this project. The first section lists the methods of transforming the *raw data* into *Raw Waveforms*, a collection of waveforms for each type of sensor corresponding to the same event.

In the second section, the *Raw Waveforms* are processed: first, the waveforms of the PMTs are deconvoluted, then all waveforms are baseline-subtracted and calibrated. Later, the signal is divided into small time intervals and the waveforms are sliced in the corresponding intervals. This creates a structure called *PMap*.

The next stage of the processing is dependent on the type of event and two different approaches are considered. The third section is reserved to events with a point-like energy deposition, in which the algorithm merges the information to a single point with a related energy. However, if the event produces a long track energy deposition, a different algorithm creates a set of discretised track points called *hits*. This will be discussed on the fourth section.

The fifth section is reserved to the explanation of an algorithm that makes use of a procedure that will be introduced in the next chapter, the correction map, together with the result of the previous stage to produce energy corrected events.

5.1 Production of *Raw Waveforms*

The FPGA modules format the *raw data*, the so-called *Raw Waveforms* (RWFs), which are basically time-ordered signal amplitudes for each of sensor measure in ADC counts. The RWFs have two properties:

- **Data acquisition window**: identifies the size of the waveform.
- **Sampling time**: specifies the length of the time interval that is used to measure the signal amplitude. The time interval depends on the type of sensor: 25 ns for PMTs, crucial for optimising the energy resolution measurement, and 1 μs for the SiPMs. The different time sampling allows to distinguish the true signal from the inherent electronic noise.

The RWFs are stored in an *hdf5* file format, with the different sensor waveforms stored in independent nodes in each file.

5.2 Production of *PMaps*

5.2.1 Waveform processing and deconvolution of the PMTs RWFs

The PMTs RWFs are not the real signal, but its derivative due to the configuration of the PMTs bias [107]. The output current from the PMTs is stable around the sensor baseline and produces a constant number of ADC counts. When light hits the PMTs, the converted photons increase the current making the output voltage and ADC amplitude to decrease. Yet, when the received light decreases, the opposite effect happens: the current decreases and the output voltage and ADC amplitude increase.

The signal, with an equal area above and below the baseline, has a null total area. The baseline of each signal is calculated by averaging the amplitude of its waveform. The noise does not bias the baseline calculation since it is equally distributed across the waveform.

A deconvolution (or baseline restoration, BLR) algorithm is an essential tool in order to recover the input pulse area of the PMTs signals, allowing the measurement of the associated energy. The algorithm consists on the accumulation (sum) of the waveform samples above a predefined threshold until it reaches a value below a specified limit. Then, the accumulator enters a discharge state and a smooth curve is applied to ensure that the reconstructed signal is continuous. The results are positive-only, zero-baseline signals called *Corrected Waveforms* (CWFs). An example of the action of this algorithm is illustrated in figure 5.1 (right).

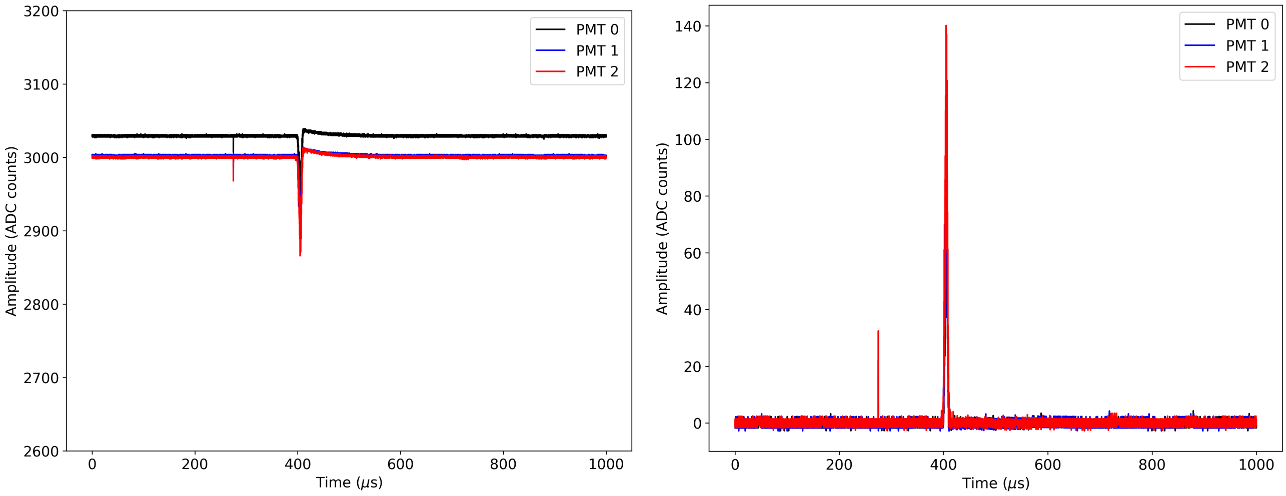

Figure 5.1: RWFs (left) and deconvoluted version (right) of the NEXT-DEMO++ PMTs for a candidate krypton event.

The result for a krypton event is a waveform consisting of two visible peaks ($S1$ and $S2$), with $S1$ coming always first and up to the maximum drift time before the second peak. As for $S2$, since it also serves as trigger, it comes centered in the spectra.

The SiPMs' waveforms, unlike the PMTs', are positive when compared to a non-null baseline and, in this case, their value is measured using the modal value of the waveform instead of the average, resulting in an unbiased measurement. An example of the RWFs and baseline-subtracted waveforms for the SiPMs for a candidate krypton event can be seen in figure 5.2.

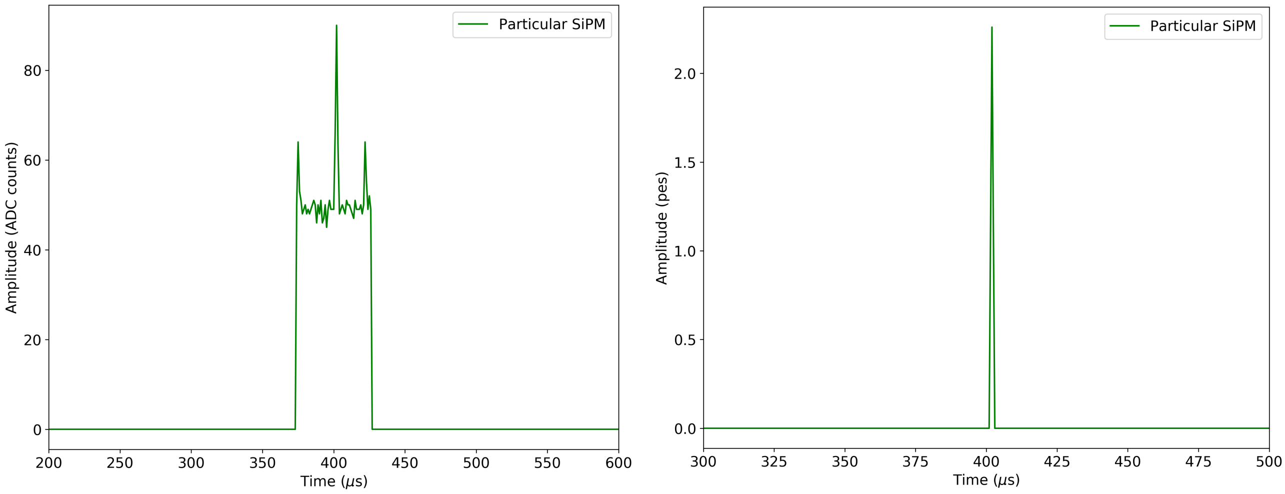

Figure 5.2: RWFs (left) and baseline-subtracted version (right) of the NEXT-DEMO++ SiPMs for a candidate krypton event.

5.2.2 Waveform calibration

The waveforms must also be calibrated due to the non-homogeneous response in all sensors. This calibration consists of a constant for each of the sensors that indicates how many ADC counts represent a single photoelectron. Then, each waveform is scaled according to the calibrations, producing a set of *Calibrated Corrected Waveforms* (CCWFs).

5.2.3 Peak finding and waveform slicing

In order to unarguably detect two signals, the best method is to apply a peak finding and waveform slicing algorithm. The objective is to find two types of signals ($S1$ and $S2$) independently, while precisely establishing the time limits on those signals in order to maintain the energy resolution capabilities of the detector.

The PMTs waveforms (CCWFs) are sampled each 25 ns, to achieve an accurate description of the original waveforms. In addition, the waveforms for the different PMTs are summed to increase the signal-over-noise ratio. This is due to the fact that the noise of a waveform is considered gaussianly distributed around the baseline with a certain standard deviation σ_{pmt}. By summing n_{pmt} waveforms, the result[5] will have a standard deviation of $\sqrt{n_{pmt}} \cdot \sigma_{pmt}$. Still, the signal increases linearly with the number of waveforms, resulting in a signal-to-noise ratio improvement with $\sqrt{n_{pmt}}$.

---

[5] From the error propagation formula.

A peak finder algorithm takes the sum of the PMTs waveforms and searches for samples above a certain threshold This threshold may depend on the signal and the type of event. However, fluctuations in the signal of the PMTs near this value may lead to a split in an otherwise single peak, an effect particularly relevant for $S1$ peaks due to their small amplitude. In order to mitigate this effect, signal time regions separated by an adjustable short time (called *stride*) are joined back together. The search is also restricted to certain buffer times in order to reduce the number of non-physical peaks. The resulting peaks are then filtered using another value of threshold, which further improves the efficiency of the algorithm. The beginning and end of the signal is kept for each peak and all this information is used to slice each waveform.

For the $S1$ peaks, since the signal is too weak to be detected in SiPMs, only PMTs waveforms can be taken into account. Then each waveform is sliced in the region defined by the previous algorithm and its information is stored. As for the $S2$ peaks, the SiPMs waveforms can be used, but the PMTs waveforms, due to the different sample rate, need to be resampled at 1μs. Moreover, since most of the SiPMs do not see the light from a given event but do have an inherent photoelectron emission pulses, another threshold is defined. Furthermore, only the sensors that have a $S2$-integrated signal above a certain number are considered. Finally, the PMTs and the SiPMs peaks are matched and stored.

5.3 Production of *kDSTs*

Low-energy electrons, like those from ^{83m}Kr decays, produce a short ionisation track. Therefore, in this case, the event can be considered to have a point-like energy deposition with unique (X, Y, Z) coordinates associated.

A specific structure to study these events is created in which all relevant information regarding energy and tracking is stored. For every $S1$ and $S2$ pair, the following information is stored:

- **Width**: time of the signal over a predefined threshold, in ns for $S1$ and μs for $S2$.
- **Height**: maximum amplitude of the peaks.
- **Time**: time corresponding to the sample with the highest signal.
- **Energy**: integral in time of the sum of the PMTs waveforms.

The drift time of the electrons producing a given $S2$ peak is calculated by the time difference between $S2$ and $S1$ signals. In fact, $S1$ is a prompt signal, produced at the instant of absorption while, to produce $S2$, the electron cloud must drift through the drift region until the EL region. The Z-coordinate of a certain signal is defined as the drift time divided by the drift velocity of electrons in the detector.

For SiPMs, which contain the tracking information, we have:

- $\mathbf{N_{min}}$: minimum number of SiPMs with a time integrated signal above a previously defined threshold.

- **Charge**: sum of the signal of the waveforms.

- $\mathbf{X}, \mathbf{Y}$ **coordinates**: these values are obtained from a barycenter determination algorithm which allows the computation of a weighted average of the sensor positions taking into account the relative charges measure by the triggered SiPMs.

All this information is stored in the so-called *kDST* in a table with 25 fields that can be summarised into four groups:

- The variables that describe the event as a whole: event number, time stamp of the event, number of **S1** and **S2** peaks (**nS1** and **nS2**, respectively).

- The variables associated with the PMTs: the **S1** and **S2** peak number, their time within buffer (**S1t** and **S2t**), their width (**S1w** and **S2w**), their maximum amplitude (**S1h** and **S2h**) and the integrated signal (**S1e** and **S2e**).

- The variables associated with the SiPMs (tracking information of the $S2$ peak): the total charged measured (**S2q**), the number of sensors with signal above a certain threshold (**Nsipm**), the reconstructed ($\mathbf{X}, \mathbf{Y}, \mathbf{R}$) and $\boldsymbol{\phi}$ positions and the standard deviation of the signal long the **X** and **Y** axis. The RMS values of **X** and **Y** are also calculated.

- The variables associated with the drift information: the drift time (**DT**), the reconstructed **Z** position (and its RMS value) with the associated standard deviation.

An event may have multiple $S1$ and $S2$ signals caused by a pile-up in the buffer, bad identification of $S1$ signal or just by producing many interactions. Therefore, all combinations of $S1$ and $S2$ signals are possible and therefore stored in each row of the table.

5.4 Production of *hDSTs*

High-energy electrons produce long and bended ionisation tracks. In order to achieve a better background rejection capability, it is required to accurately reproduce the electron's path.

As mentioned in Subsection 5.2.3, a first cut of 1 pes (photoelectrons) is applied on the SiPMs charge in order to eliminate dark current and electronic noise. In addition, only SiPMs with an integrated charge above 5 pes are considered. Then, the SiPMs charge is rebinned into time slices (usually 2 μS slicing) and, for each slice, the charge pattern obtained. If the charge is higher than a designated value, a 3D *hit* is generated with the X and Y coordinates given by the SiPM, and Z obtained by the result of the product of the difference in time between the $S1$ signal and the slice and the electron's drift velocity. The threshold is chosen in order to eliminate the effects of the diffusion and light spread that is noticeable in the SiPMs charge pattern by removing the charge far from the center of the *hit* and keeping the information of the position of the light source. If in a given slice there are no SiPMs with charge above the value, the energy of that slice is distributed between the closest slice belonging to the same $S2$ signal.

The PMTs waveforms are rebinned into 2 μs time slicing and the measured energy in each time slice is divided among the reconstructed *hits* proportionally to the charge of the SiPMs used to created the *hits*.

This information is stored in individual files called *hDSTs* with 11 fields in each file. Each row has the information of a single *hit*: the event number, the time stamp of the event, the peak number, the energy, charge and spatial coordinates with the standard deviations of the transverse coordinates of a *hit*.

5.5 Production of *cDSTs*

The last step of data processing takes the *hDSTs* and the *Correction Maps* that will be extensively addressed in the next chapter.

The algorithm is as follows:

1. Correcting the *hits*:
    (a) Apply a new charge threshold to the *hits*. The energy of the *hits* that do not pass this limit is redistributed among the *hits* that have the same time slice.
    (b) The energy of the *hits* that do not pass the threshold is redistributed by the closest valid *hits*.
    (c) From the correction map, the energy is properly corrected (a detailed description is presented in the next chapter).
2. Reconstructing the tracks:
    (a) The *hits* are grouped into tracks by dividing the gas volume into 3D pixels known as *voxels*. These *voxels* have an exact maximum dimension and an energy corresponding to the sum of the *hits* grouped in that particular *voxel*.
    (b) Then, adjacent *voxels* are group into separated sets (that will be considered the particle tracks) using a Breadth First Search (BFS) algorithm [108]. This procedure identifies the pair of *voxels* with the longest distance between them, the so-called end-point of the track. The dimension of the *voxels* is not set and may be optimised from event to event by avoiding having only one *hit* on the boarder of a *voxel*. The minimum size of the *voxel* is limited by the distance between two adjacent SiPMs and can not be smaller than that value.

Chapter 6

Producing correction maps

One of the requirements of the last step of the data processing is the production of correction maps. A correction map, also called calibration map, is a data structure used to normalise the energy of the events that occur in different regions of a detector. Their need comes from the fact that the coverage of light sensors is limited and there may be some photons that are reflected or lost in the detector edges. Due to the high complexity of the physical phenomena, like multiple reflections of the light, they can not be analytically computed.

These maps also contain information about the lifetime of the drifting electrons, an important feature that monitors the level of impurities in the gas, or the existence of any regions on the detector where there is no proper gas circulation.

6.1 Krypton calibrations

A rubidium source is placed in a dedicated section of the gas system, as described in Subsection 4.1.6, and when it decays to its final isotope, it flows inside the chamber. It is used as a low-energy point-like calibration source in NEXT detectors and one of its uses is to produce correction maps.

Figure 6.1 shows the decay scheme of the exotic isotope ^{83}Rb. First, it decays to $^{83\mathrm{m}}$Kr by capturing one electron and emitting one neutrino (Electron Capture, EC), with an half-life of 86.2 days. Then, this nucleus decays to the stable ground state by two consecutive Internal Conversions (IC), a process where an excited nucleus transfers its excess energy to an inner shell electrons, that is emitted with a very well known defined kinetic energy that corresponds to the difference between the energy released by the nucleus and the electron binding energy. The half-life of the decay is dominated by the first conversion (1.83 h compared to 154.4 ns) and the energy released on these decays is 41.5 keV. This decay results in a point-like distribution of charge with evenly-distributed events.

The position of the events is computed by measuring the time difference between the detection of the primary scintillation signal ($S1$) and the secondary scintillation signal ($S2$), multiplied by the drift velocity of the electrons, yielding the Z-coordinate of the ionising event. The X, Y spatial coordinates are obtained in the SiPMs tracking plane by the reconstruction algorithms.

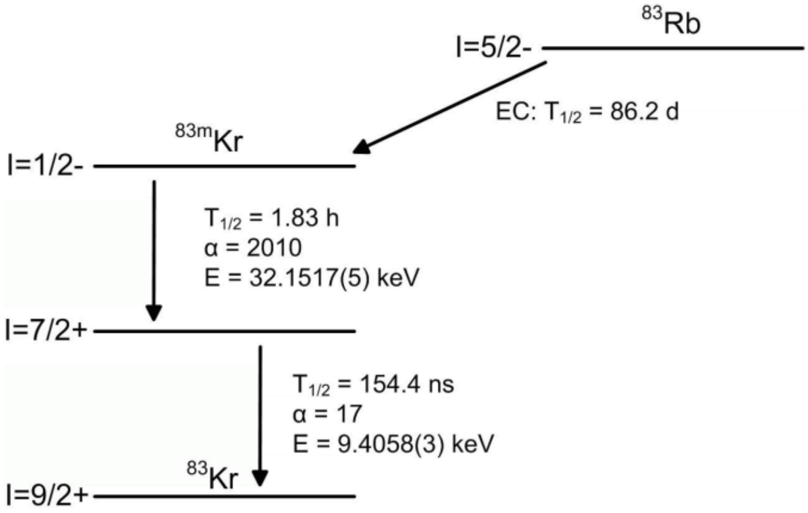

Figure 6.1: ^{83}Rb decay scheme [109]. EC stands for electron capture, E for the energy of the released on the decay, l for the spin of a state, $T_{1/2}$ for the half-life of the given process and α is the IC coefficient.

However, the measured energy of these events needs to be corrected mainly due to the following two effects:

1. **The finite electron lifetime** - the electrons that drift towards the cathode can be captured by impurities in the gas. This effect can be described by the following equation:

$$q\left(X,Y,Z,t\right) = q_0 \exp\left(-\frac{t}{\tau(X,Y,Z)}\right), \tag{6.1}$$

   where $q\left(X,Y,Z,t\right)$ and q_0 are the charge collected at a drift time t and the charge initially produced, respectively, and $\tau(X,Y,Z)$ is the lifetime. The lifetime may depend on the spatial coordinates (X,Y,Z) due to non-homogeneous recirculation of the gas and the ensuing increase in impurity levels.

2. **The light detected by the PMTs is dependent on the $(\mathbf{X},\mathbf{Y})$ position of the event** - since the collected light depends on the variation of the solid angle covered by the PMTs, losses in the detector edges and reflections in the TPB coated vessel walls[6], the map will normalise the energy of the events in the different regions of the detector.

6.2 Data acquisition and occurrences

During the NEXT-DEMO++ data taking period, from the 12th of March until the 6th of June, several sources were placed on top of the detector to study its performance at low and high energies and with different triggering conditions.

---

[6] Imperfections like different TPB widths will affect the reflection.

In table 6.1 a summary of each run, its duration and electrical conditions, is presented:

- The first run (I - 1 and I - 2) only differs in the position of the thorium and caesium sources.
- As for run II, it only used trigger 2.
- For run III, the triggering conditions were different, allowing a sample rate about 4 times higher than previous runs.
- As for run IV, a thorium source was added, increasing the sample rate for both triggers.
- In run V, the voltages applied to the cathode and the gate were reduced.

Figure 6.2 shows the evolution of the pressure over time and the associated Y/P. The Y/P values are calculated with a formula obtained in [110]:

$$Y/P = 140 \cdot (E/P) - 116 \qquad (\mathrm{ph/e^-/cm/bar}) \tag{6.2}$$

Also represented is the Y/P for the beginning of run III and ending of run IV (these value will be used in a later section) and the occurrences of sparks (dotted lines).

A total of 13 different maps were produced in the scope, each one using at least 4 days of data taking.

Table 6.1: Data taking for map production. The total duration of data taking is 87.17 days.

Run	Duration (days)	$V_{cathode}$ (kV)	V_{gate} (kV)	Sources	Trigger(s)	Rate (Hz)
I - 1	5.72	28.0	13.5	Th at side Cs at top	Both triggers	Trigger 1: 42 Trigger 2: 6
I - 2	25.79	28.0	13.5	Th at top Cs at top	Both triggers	Trigger 1: 42 Trigger 2: 6
II	11.58	28.0	13.5	Th at top Cs at top	Trigger 2 only	Trigger 1: 0 Trigger 2: 25
III	17.36	28.0	13.5	Th at top Cs at top	Both triggers	Trigger 1: 152 Trigger 2: 20
IV	21.26	28.0	13.5	2 Th at top Cs at top	Both triggers	Trigger 1: 169 Trigger 2: 25
V	5.46	23.5	10.5	2 Th at top Cs at top	Both triggers	Trigger 1: 185 Trigger 2: 21

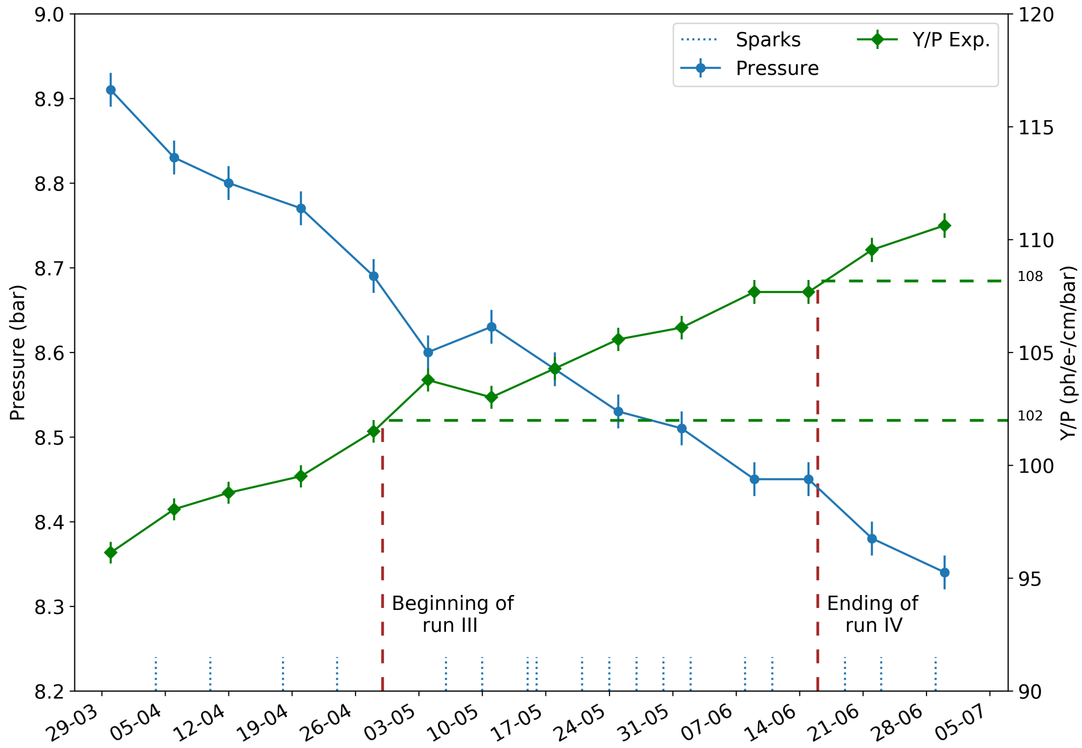

Figure 6.2: Pressure over time and associated Y/P. The dashed brown lines correspond to the beginning of run III and ending of run IV and the dashed green lines correspond to the associated value of Y/P. The dotted lines represent the occurrence of sparks.

6.3 Data selection

6.3.1 Multiplicity of $S1$ and $S2$ signals

The produced *kDSTs* have a multiplicity of $nS1$ and $nS2$ signals so, in order to analyse the krypton peak, the first step is to select the events with 1 $nS1$ and 1 $nS2$ signals to make sure that a particular $S2$ signal corresponds to a particular pair $S1$ and $S2$ coming from the same event.

Figure 6.3 (left) shows the fraction of $nS1$ candidates over the total number of events and figure 6.3 (right) the fraction of $nS2$ events over the events where $nS1 = 1$ for a set of data from run IV. The events that have 1 $nS1$ represent around 35 % of the total number of events. Moreover, the fraction of events that have 1 $nS2$ for a single $nS1$ is around 25 %, which means that the relevant events for the production of the map represent around 9 % of the total number of events.

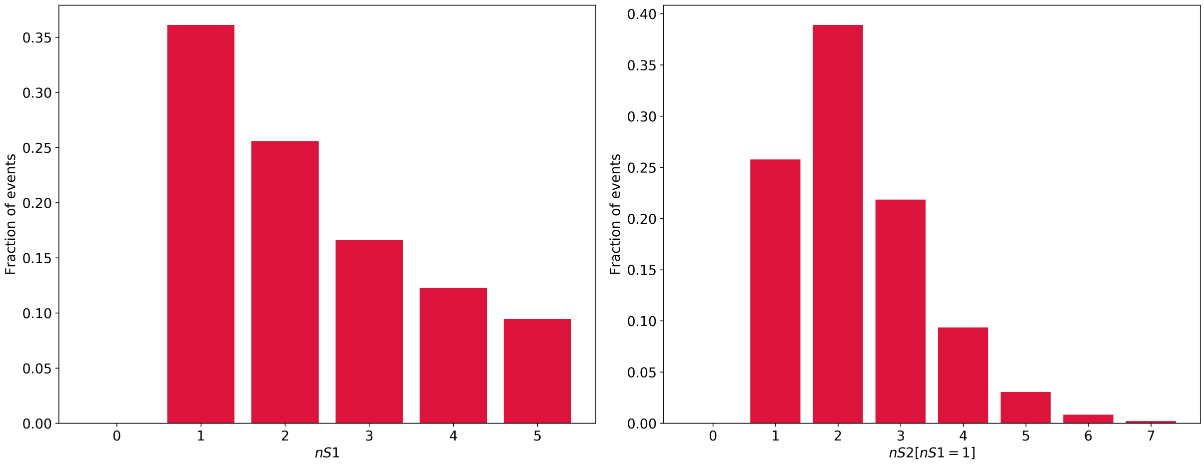

Figure 6.3: Fraction of $nS1$ events (left) and fraction of $nS2$ events where $nS1 = 1$ (right).

6.3.2 Checking the distribution of events over time

In order to study the stability of the detector, it is important to check the rate of events. An example of such distribution is shown in figure 6.4. It can be seen that there are several gaps in the distribution. These result from sparks in the detector. By removing the files after the spark, in order to make sure that there is no bias in the map production, some gaps appear with several hours duration. The gaps also reflect the recovery of the high voltage applied to the cathode and anode after a spark. On a later stage of the map production, a time evolution of the relevant quantities will be computed and, for these time bins that do not have data, it will not be possible to produce any results.

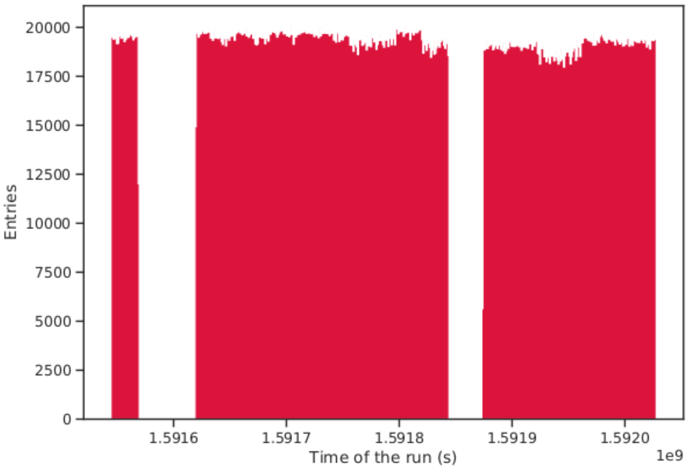

Figure 6.4: Example of a distribution of events over time. The gaps correspond to the time in which a spark happened and the detector recovered.

6.3.3 Spatial selection

With the aim of assessing the non-homogeneity of the detector, it is relevant to analyse the distribution of events in the XY plane to check if there is any favourable region where more/less events are located, which may indicate some inoperative or defective SiPMs or wrongly reconstructed events. An example of a XY distribution is presented in figure 6.5 for $X, Y \in [-70, 70]$ mm. It can be seen that the distribution of events if roughly uniform for a radius of less than 60 mm. The regions outside that radius may have poorly reconstructed events due to the fact that the barycenter is not properly computed in the boarders of the vessel due to the undercoverage of the tracking plane as seen in figure 4.3 (right).

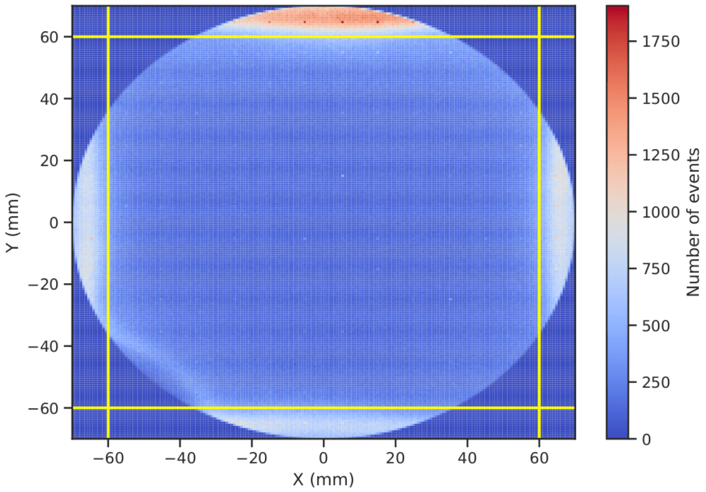

Figure 6.5: Example of a distribution of events in XY plane. The yellow lines are placed at $X, Y = -60$ mm and $X, Y = 60$ mm.

The distributions of events in the X and Y coordinates are presented in figure 6.6. As can be seen, there is a small difference between them which might be explained by the relative position of the high energy sources in the detector. As presented in table 6.1, both thorium and caesium sources are placed at the top, resulting on a higher concentration of X-rays directed to the top of the detector, as confirmed by the top corner concentration of events in figure 6.5. This will introduce then a higher deposition of events for a higher Y value.

Due to the fact that the distribution can be considered uniform for the radial region below 60 mm, a first cut is applied:

$$\boxed{R < 60 \text{ mm}}$$

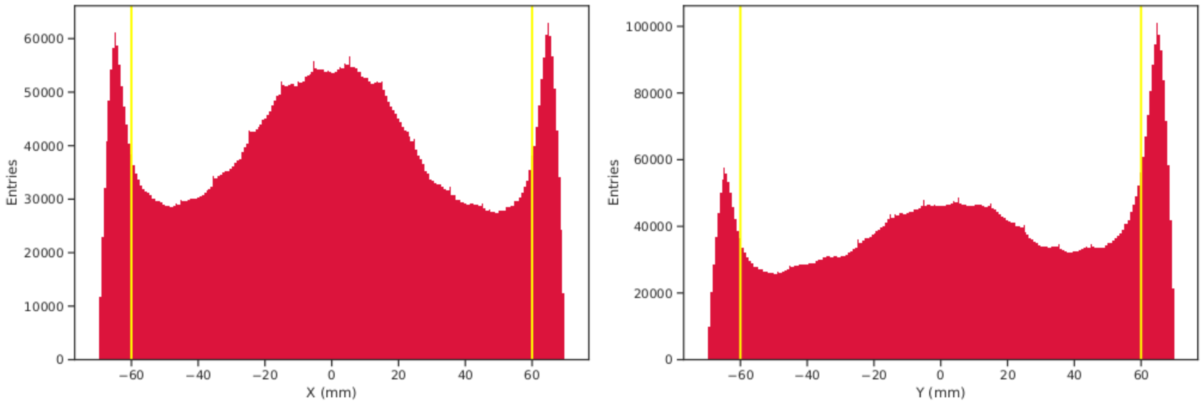

Figure 6.6: Example of a X (left) and Y (right) distributions. The yellow lines are placed at $X, Y = -60$ mm and $X, Y = 60$ mm.

The drift time distribution, which corresponds to the time difference between the $S2$ and $S1$ signals, is shown in figure 6.7. As can be seen, there is a clear drop in the number of events around 330 μs and another drop around 400 μs. The distribution must be cutted in two different datasets, one to be used for the computation of the calibration map and another for the calculation of the drift velocity. The first one requires a cut near the drift region length, the second requires to have the additional plateau illustrated in figure 6.7 (right). So, another data selection is considered, with DT_{map} and DT_{dv} as the drift time data used for the map production and time evolution computation, respectively:

$$\boxed{\begin{array}{c} 15 < DT_{map} < 320 \ \ \mu\text{s} \\ 15 < DT_{dv} < 400 \ \ \mu\text{s} \end{array}}$$

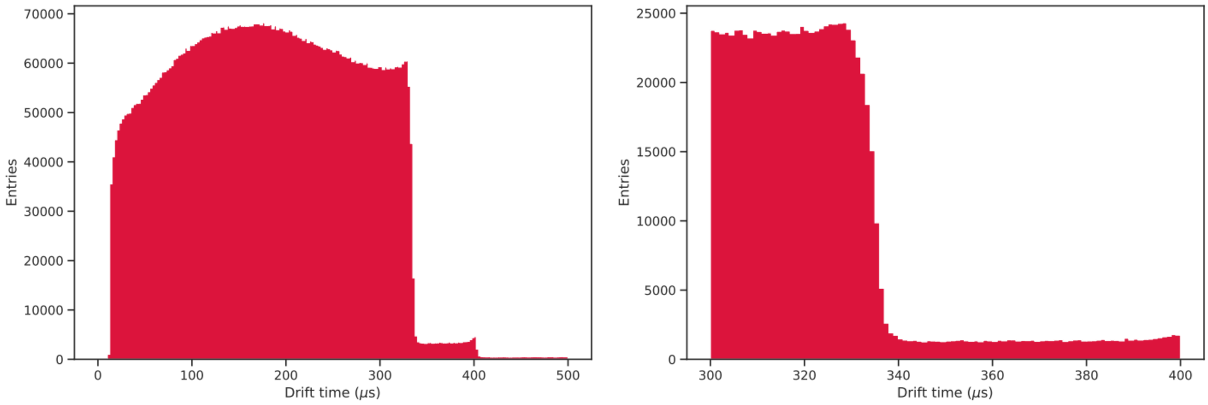

Figure 6.7: Example of a drift time distribution, from 0 to 500 μs (left) and a zoom in the region of 300 to 400 μs (right).

6.3.4 Krypton energy selection

Figure 6.8 shows the energy distribution with the 1 $S1$ and 1 $S2$ selection already applied. There are 3 peaks. The first and second peaks are related to the xenon X-rays from the K_α and K_β emissions, with an energy of 29.7 and 33.8 keV, respectively [111]. The third peak is the krypton peak, with an energy of 41.5 keV. The objective is to only use the krypton peak for the calibration map, minimising the influence of the other two peaks. In order to find a suitable energy range to select krypton events, a study of the spectra for different regions is performed. Figure 6.9 shows the energy distribution in several drift time intervals. As can be seen, the krypton peak position is quite stable in the different drift time intervals.

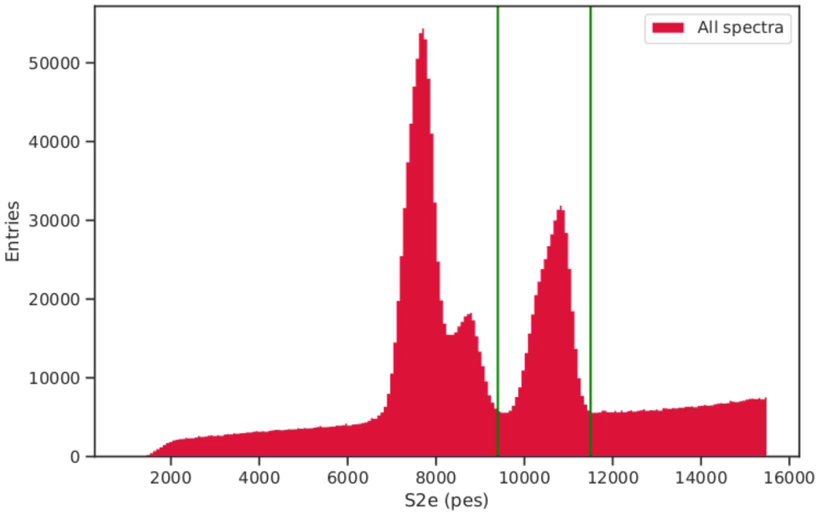

Figure 6.8: Example of the energy distribution. The green lines are at 9400 and 11500 pes.

Then, in order to assess if the krypton peak shifts radially in the detector, the same distributions are plotted with several radial selections. The result is illustrated in figure 6.10. It can be seen that the krypton peak position decreases for higher radial selections, with this behaviour being noticeable for every drift time interval.

The energy distributions as a function of the drift time are also important in order to evaluate the lifetime of the electrons. As illustrated in figure 6.11, for a radius less than 40 mm, the energy distribution in the krypton peak is more sharply defined than when no radius selection is considered. To produce the map without biasing the krypton peak, a judicious cut on $S2e$ is applied:

$$\boxed{9400 < S2e < 11500 \text{ pes}}$$

This interval, however, will change for different datasets due to the increase of $S2e$ over time, a subject that will be addressed in a later section.

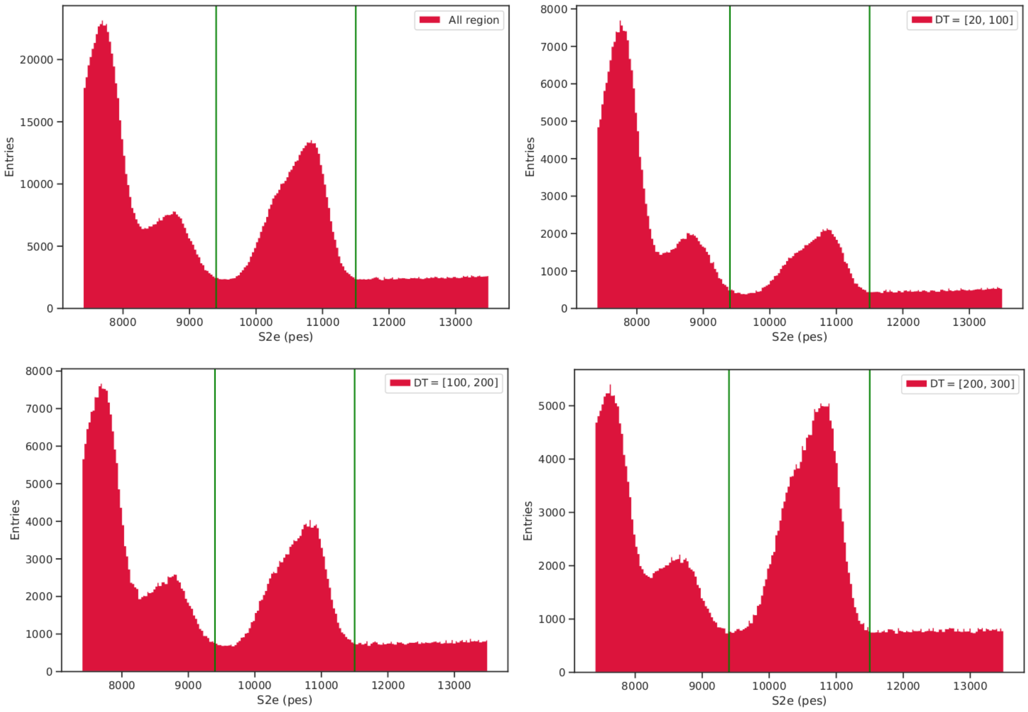

Figure 6.9: Example of the energy distribution considering several drift time regions: all detector (top left), from 0 to 100 μs (top right), from 100 to 200 μs (bottom left) and from 200 to 300 μs (bottom right). The green lines are at 9400 and 11500 pes.

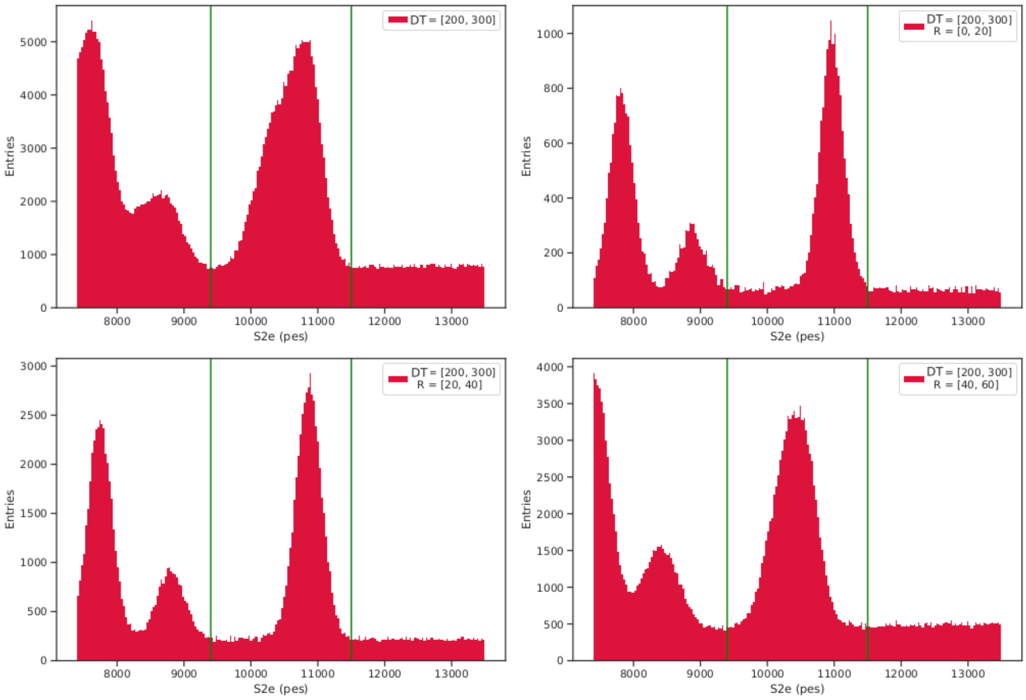

Figure 6.10: Example of the energy distribution considering several radial regions of the detector, with a drift time between 200 and 300 μs: all detector (top left), radial selection from 0 to 20 mm (top right), radial selection from 20 to 40 mm (bottom left) and radial selection from 40 to 60 mm (bottom right). The green lines are at 9400 and 11500 pes.

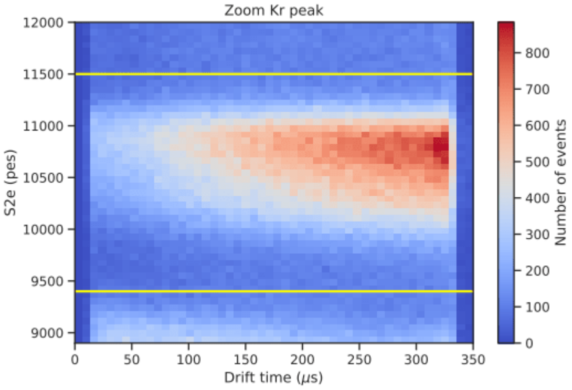

Figure 6.11: Example of the energy distributions as a function of the drift time: zooming on the krypton peak (left) and on a radial selection of 0 to 40 mm also zooming on the krypton peak (right). The yellow lines are at 9400 and 11500 pes.

6.3.5 Other variables selection

The data sample for the calibration map computation can be further restrained by looking at other quantities, such as $S1e$, $S2w$, $S2q$ and $Nsipm$. Figure 6.12 shows the distributions of those different variables as a function of $S2e$.

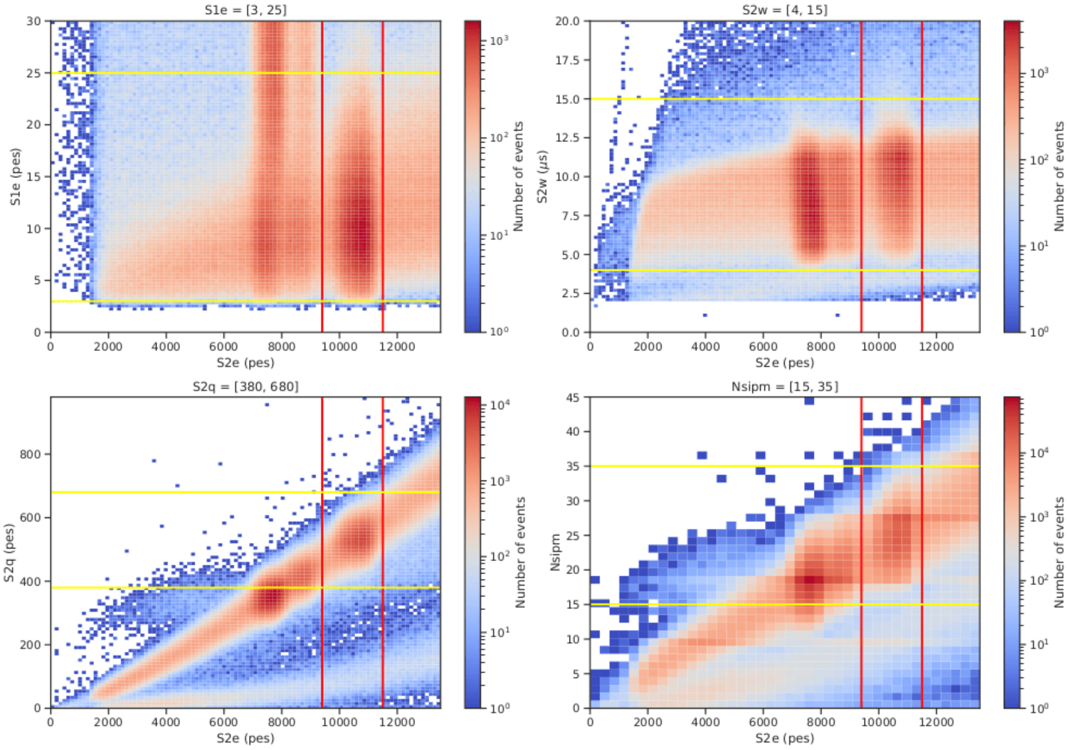

Figure 6.12: Example of the $S1e$, $S2w$, $S2q$ and $Nsipm$ distributions as a function of $S2e$. The red lines represent the $S2e$ cut, while the yellow ones represent the intended cut in the several variables.

For the distributions showed in figure 6.12, the following cuts were considered:

$$\boxed{\begin{array}{c} 3 < S1e < 25 \ \text{pes} \\ 4 < S2w < 15 \ \mu\text{s} \\ 380 < S2q < 680 \ \text{pes} \\ 15 < Nsipm < 35 \end{array}}$$

6.3.6 Distribution of events

With the data judiciously selected, there is still one more thing to consider before producing a map which is related to the distribution of events. The first step is to divide the map into **N** $\times$ **N** bins. Generally, the more bins are considered, the more trustworthy will the correction map be. This caveat is having less events per bin, which may have repercussions in the statistical meaning and the fits obtained. Therefore, a compromise between the number of bins and number of events per bin must be found.

The best trade-off leads to a production of a map with 40×40 (X, Y) bins, with a total of 1600 bins. Each bin will represent 3 mm of the tracking plane, since the data is selected for a radial region of less than 60 mm. Knowing this, it must be determined the minimum number of events per bin.

Figure 6.13, on the left side, shows an example of the distribution of the number of events per bin and, on the right side, the same distribution but computed in (X, Y) bins. A clear peak around 320 events per bin is seen and the 2D plot shows a uniform distribution of events per bin. The outer radius of the map has less events due to the binning effects.

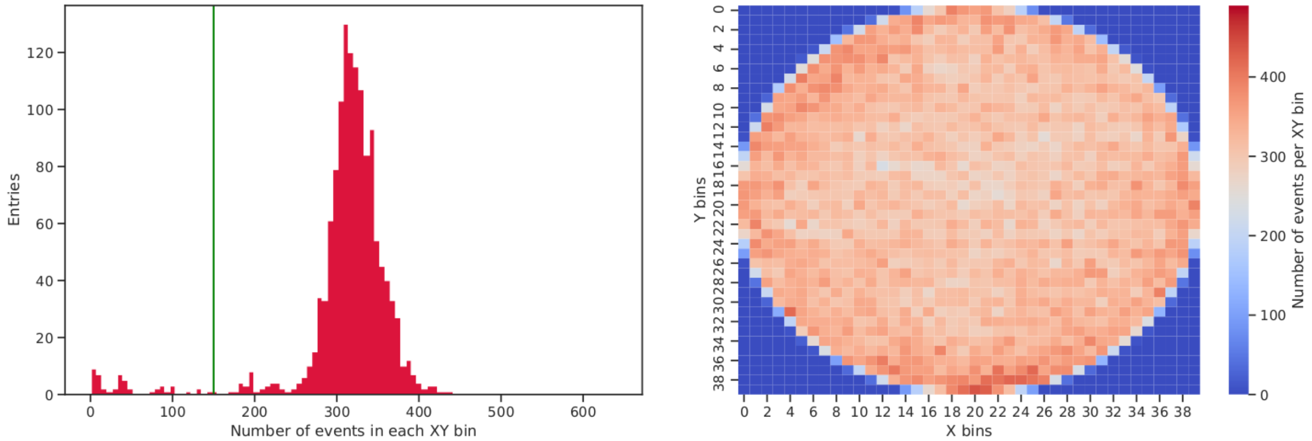

Figure 6.13: Example of the distribution of the number of events per bin for a binning of 40×40 (left) and 2D distribution of the number of events per bin. The green line on the left represents the minimum number of events in a bin required to do a fitting. More than 99 % of the events are after the green line.

The general procedure chosen to determine the minimum number of events per bin is having at least 99 % of all events per map. This was considered for all maps. For this example, a minimum number (n_{min}) of 150 events per bin was considered for the particular distribution.

6.3.7 Summary of data selection

The summary of data selection is presented in table 6.2.

Table 6.2: Summary of all variable selection.

Variable	Minimum	Maximum	Observation
$nS1$	1		Applicable for all maps
$nS2$	1		Applicable for all maps
R (mm)	0	60	Applicable for all maps
DT_{map} (μs)	15	320	Applicable for all maps
DT_{dv} (μs)	15	400	Applicable for all maps
$S2e$ (pes)	9400	11500	May vary
$S1e$ (pes)	3	25	May vary
$S2w$ (μs)	4	15	May vary
$S2q$ (pes)	380	680	May vary
$Nsipm$	15	35	May vary
n_{min}	150		May vary

6.4 Correction map production procedure

Having the data carefully selected, the minimum number of events per bin and the intended binning considered, the map production can proceed. The general idea is to display, for each bin, the energy distribution as a function of the drift time DT and fit the exponential function:

$$S2e(DT) = e_0 \exp\left(-\frac{DT}{\tau}\right), \tag{6.3}$$

with e_0 the produced charge in the decay and τ the electrons' lifetime. Then, in order to produce a map, the following steps are considered:

1. Data preparation and fitting procedure:
   (a) With the distribution of events per bin prepared, like the one shown in figure 6.13 (right), the number of events n_{evt} is assessed so as to be greater than the minimum number of events n_{min} chosen.
   (b) If $n_{evt} \leq n_{min}$ in a particular bin, the algorithm displays a warning sign stating that a fit can not be produced and it fills up a matrix with zeros for each of the fitting parameters for that bin.
   (c) If $n_{evt} > n_{min}$ in a particular bin, a mask is passed with the selection parameters of the energy and drift time range to the data. Then, an exponential fit to the profile distribution of $S2e$ as a function of the drift time is performed and the e_0, τ and χ^2 parameters are obtained for each bin. An example of the fit is presented in figure 6.14.

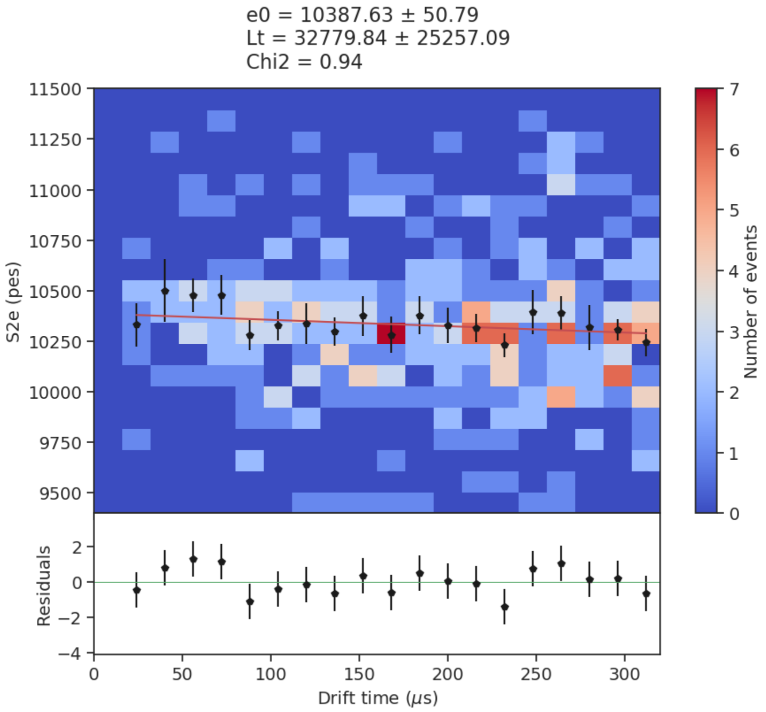

Figure 6.14: Example of a fit: the energy distribution as a function of the drift time with the data points representing the profile of the distribution and the red line the exponential fit. The subplot below shows the residuals, computed as the ratio of the difference between the red fit line and the profile points and the errors associated with the points.

2. Map regularisation:
   (a) For the bins that did not produce a fit or in which the χ^2 is outside of the desired range, the values of e_0 and τ are obtained from the average value of e_0 and τ from the surrounding bins.
3. Add information to the map: the X and Y range in which the map is based on (X_{range} and Y_{range}, respectively), the run number and number of bins.

An example of a correction map is presented in figure 6.15. As can be seen, the distribution of e_0 is uniform and smooth, with lower e_0 values for higher radius. The 1D distribution of e_0 and its uncertainty can be seen in figure 6.16.

Figure 6.17 shows the distribution of lifetime (left) and respective uncertainty (right). In figure 6.18 it is shown the distribution of the lifetime as a function of the e_0 value (left) and the distribution of the lifetime as a function of the significance of the lifetime obtained (right), i.e., how does the lifetime evidentiates from the respective error. As can be seen from the distribution on the left in figure 6.18, the majority of fits produce a positive lifetime between 0 and 50 ms. Also, from the plot on the right, the distribution of events is concentrated in the region of higher and positive significance, from a 0.5 to 3. In addition, it points towards to a lifetime value around 40 - 50 ms. Having very high and negative values of lifetime or big errors is mostly a statistical issue and not necessarily a problem with the fit equation. As explained later in the time evolution section, the lifetime is positive-only and concentrated around a central value, since it uses larger time intervals, thus having more statistics.

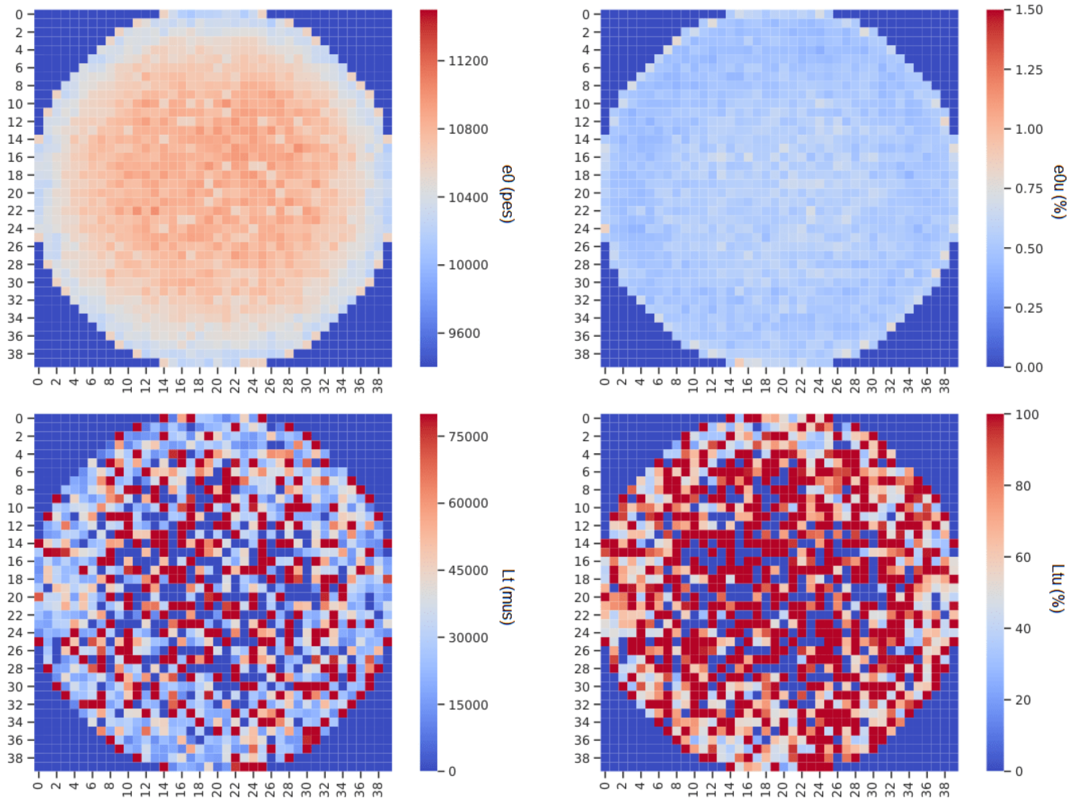

Figure 6.15: An example of a map, with the e_0 on the top left, its uncertainty in % on the top right, the lifetime value at the bottom left and its uncertainty in % an the bottom right.

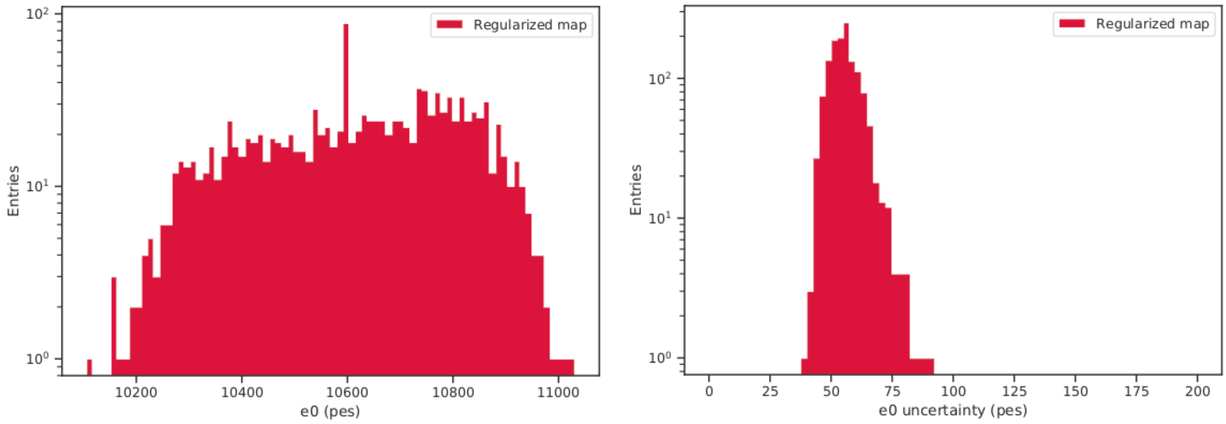

Figure 6.16: e_0 (left) and its uncertainty (right) distribution for the map in figure 6.15.

In order to check the merit of the fits, one can look at the χ^2 distribution in figure 6.19. As shown, the majority of the fits have a $\chi^2 < 4$. In figure 6.20, example of fits for different bins are shown. The residuals presented below are computed by subtracting the mean energy in each bin (the point position) by the value of energy obtained through the fit and then dividing the result by the error associated with the point. Most of the values are within -2 and 2, indicating once again that the fits are adequate.

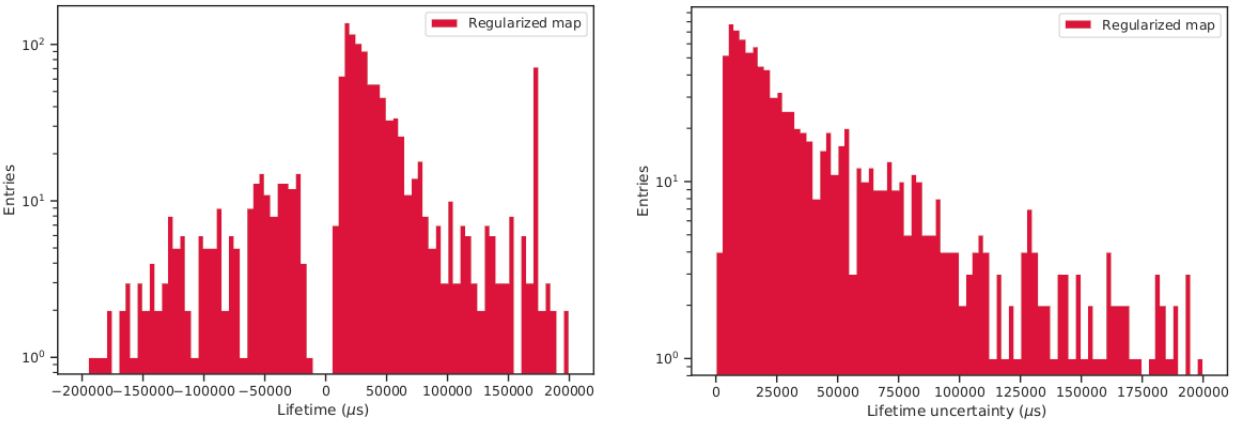

Figure 6.17: Lifetime (left) and its uncertainty (right) distribution for the map in figure 6.15.

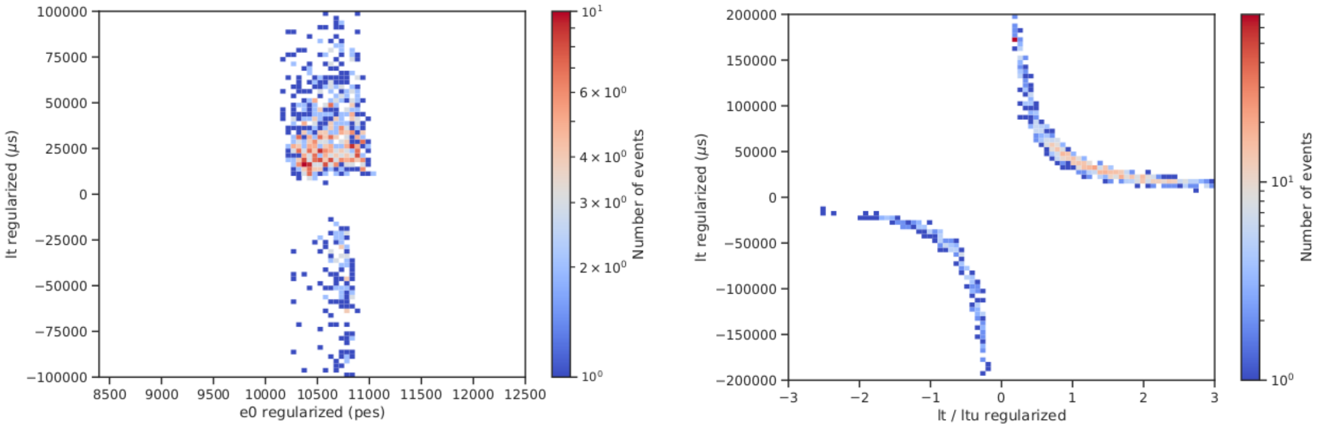

Figure 6.18: Lifetime distribution as a function of the e_0 parameter (left) and lifetime distribution as a function of the ratio of the lifetime and its uncertainty (right) for the map in figure 6.15.

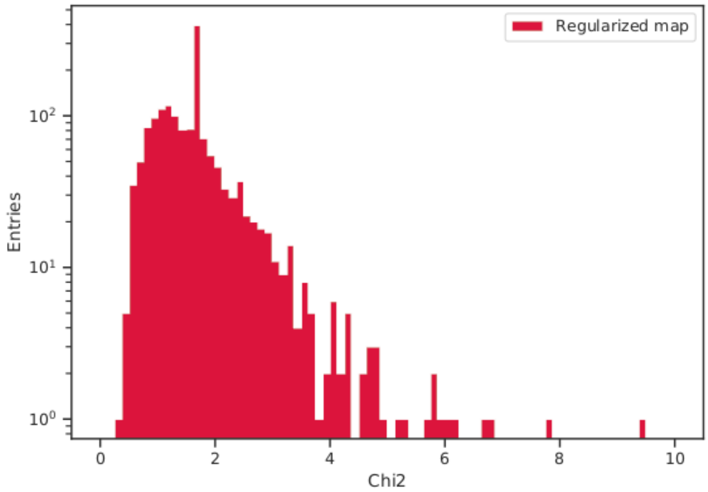

Figure 6.19: χ^2 distribution of the fits for the map in figure 6.15.

6.5 Time evolution computation

One important feature of the calibration maps is to evaluate how the relevant quantities evolve over run time. To compute this evolution, the next steps are followed:

1. The distribution of events over time is divided in time intervals, usually 2 hours long.
2. In each time bin, the average of the variables $S1w$, $S1h$, $S1e$, $S2w$, $S2h$, $S2e$, $S2q$, $Nsipm$, $Xrms$ and $Yrms$ is taken.
3. A fit to the corrected $S2e$ distribution as a function of the drift time is made, similarly to those in Section 6.4, in order to obtain e_0 and τ.
4. A new variable is computed - the drift velocity of the electrons under the drift field. A fit to the drift time distribution is performed using a sigmoid function:
$$f(DT) = \frac{\alpha}{1 + \exp\left(-\beta \cdot (DT - \gamma)\right)} + \delta \quad \Rightarrow \quad v = \frac{Z_{cath}}{\gamma}, \tag{6.4}$$
where α is the scale, β is the slope, γ is the inflection point and δ is the offset related to the first plateau. These variables come from the fit. Then, the drift velocity v is obtained by dividing the cathode position Z_{cath} (310 mm) by the inflection point. An example of the fit is presented in figure 6.21.
5. The energy resolution and its uncertainty is also computed by doing a gaussian fit to the corrected energy distribution.

The time evolution distribution for some variables is shown in figure 6.22. Two gaps in each distribution can be seen, which relate to the distribution presented in figure 6.4. Most of the variables have a small variation over time, specially e_0, the v and $S2e$, which fluctuate less that 0.5 % in respect to the mean value. The lifetime value over time is centered at 48 ms, a value around 10 times higher than in NEW [112], indicating that few electrons are lost. For the $S1e$, the variation is within ± 5 % and for the energy resolution is within ± 10 %. The following value for v was obtained:

$$v = 0.93076 \pm 0.00013 \ \text{mm}/\mu\text{s} \tag{6.5}$$

6.6 Applying the correction map to the data

The energy E of an event is also corrected using the correction map. The corrected energy E_{corr}, taking into account the time evolution of e_0 and τ (corr_{e_0} and corr_{τ}, respectively) coming from the correction map, is given by the following formula:

$$E_{corr} = E \times \frac{1}{e_0 \cdot \text{corr}_{e_0}} \times \exp\left(\frac{DT}{\tau \cdot \text{corr}_{\tau}}\right), \tag{6.6}$$

The time evolution correction factor of a parameter is given by the ratio of the linear interpolation of the parameter divided by its mean value.

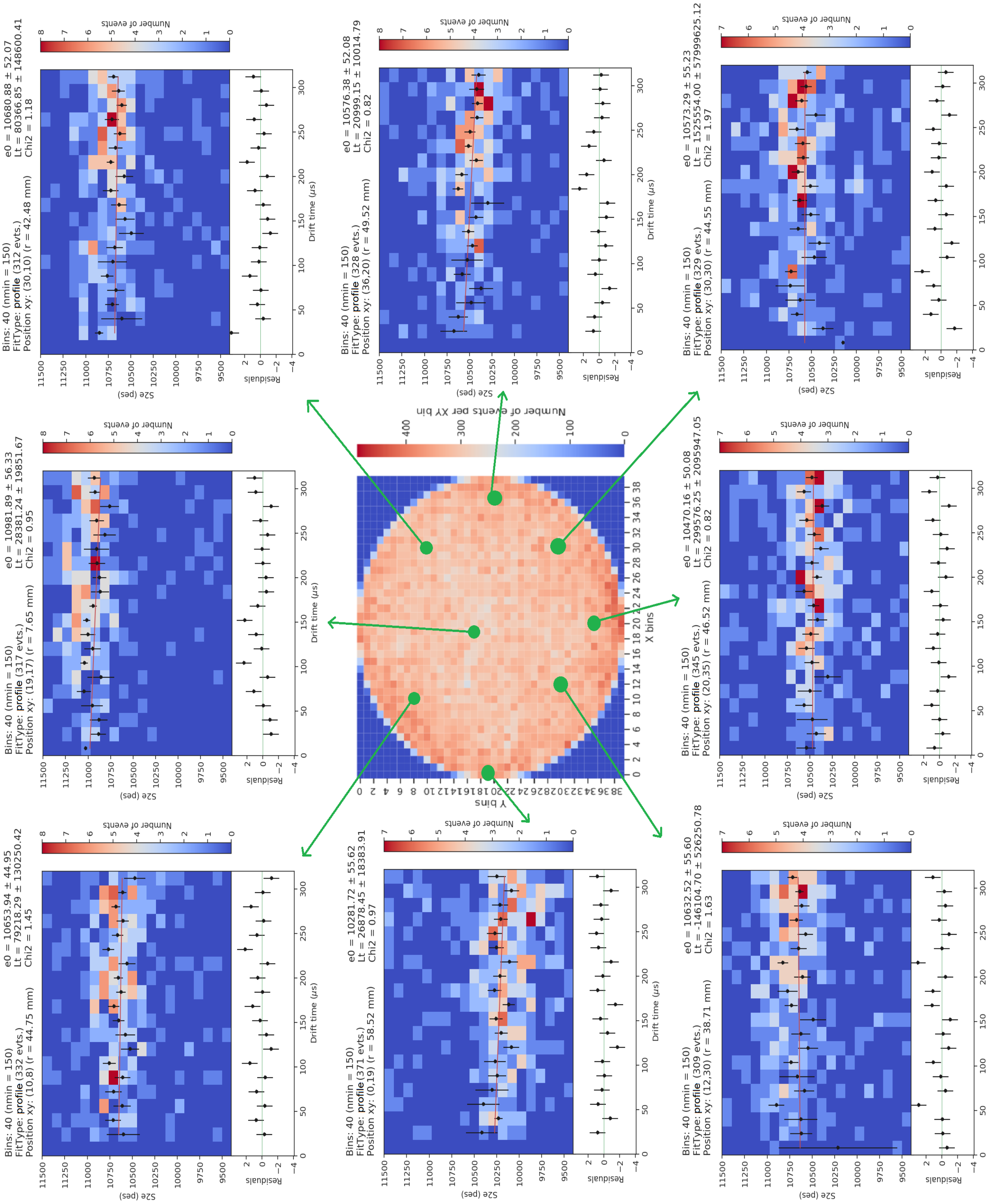

Figure 6.20: Example of fits in several bins of the detector for the map in figure 6.15.

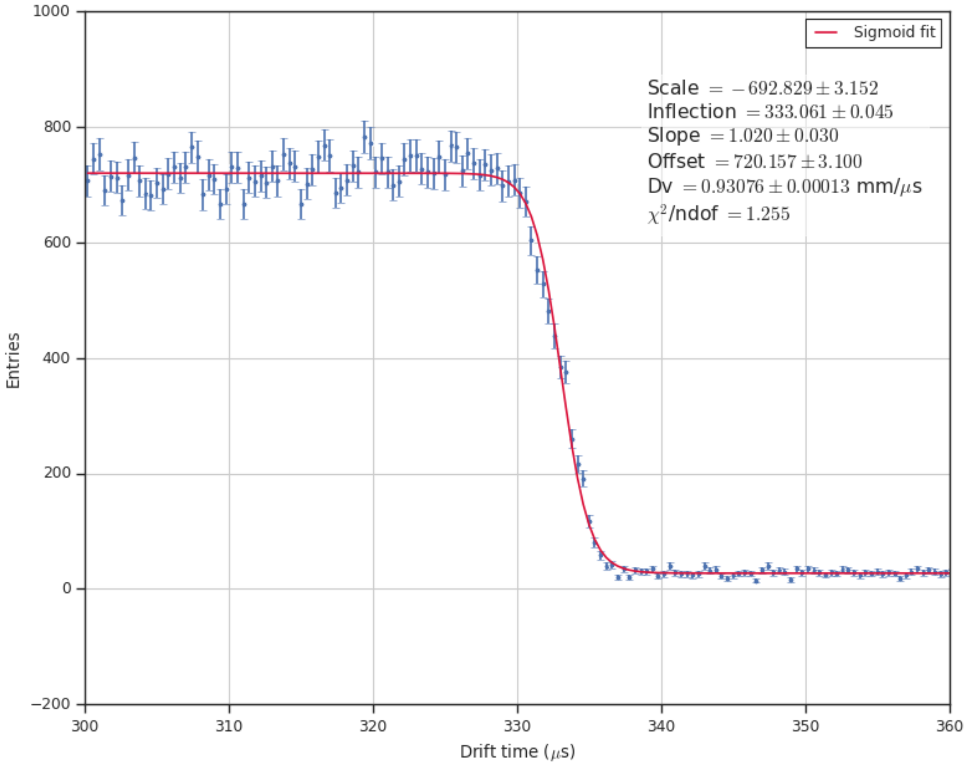

Figure 6.21: Example of a sigmoid function fit to the drift time distribution. The respective parameters coming from the fit are also presented.

6.6.1 Data correction as a function of DT, R and ϕ

Figure 6.23 shows a comparison between the uncorrected (left) and the corrected data (right) for several radial regions of the detector, namely $0 < R < 20$ mm, $20 < R < 40$ mm and $40 < R < 50$ mm. As can be seen, the corrected data is more gaussian-like and the krypton peaks, for the different radial regions, are at similar positions around 11200 pes. As for the uncorrected, the region $40 < R < 50$ mm has its peak at a significant lower value (around 10500 pes) when comparing to the other regions where the peak is around 10900 - 11000 pes. Figure 6.24 shows the profile for the uncorrected (left) and corrected (right) energy distributions as a function of the drift time. As can be seen, a residual effect is still visible for the outer regions, which could be mitigated with higher statistic data samples.

The uncorrected and corrected energy distributions as a function of the drift time, the radial position and the ϕ are shown in figures 6.25, 6.26 and 6.27, respectively. For the energy distribution, it can be seen that the width of the distribution is smaller, with an increase in its mean value for the corrected distribution. The corrected energy distribution as a function of radial position, compared to the uncorrected, is more flat until $R = 50$ mm. Finally, for the distribution as a function of ϕ, as seen in figure 6.27, the events are narrower in energy for the corrected distribution.

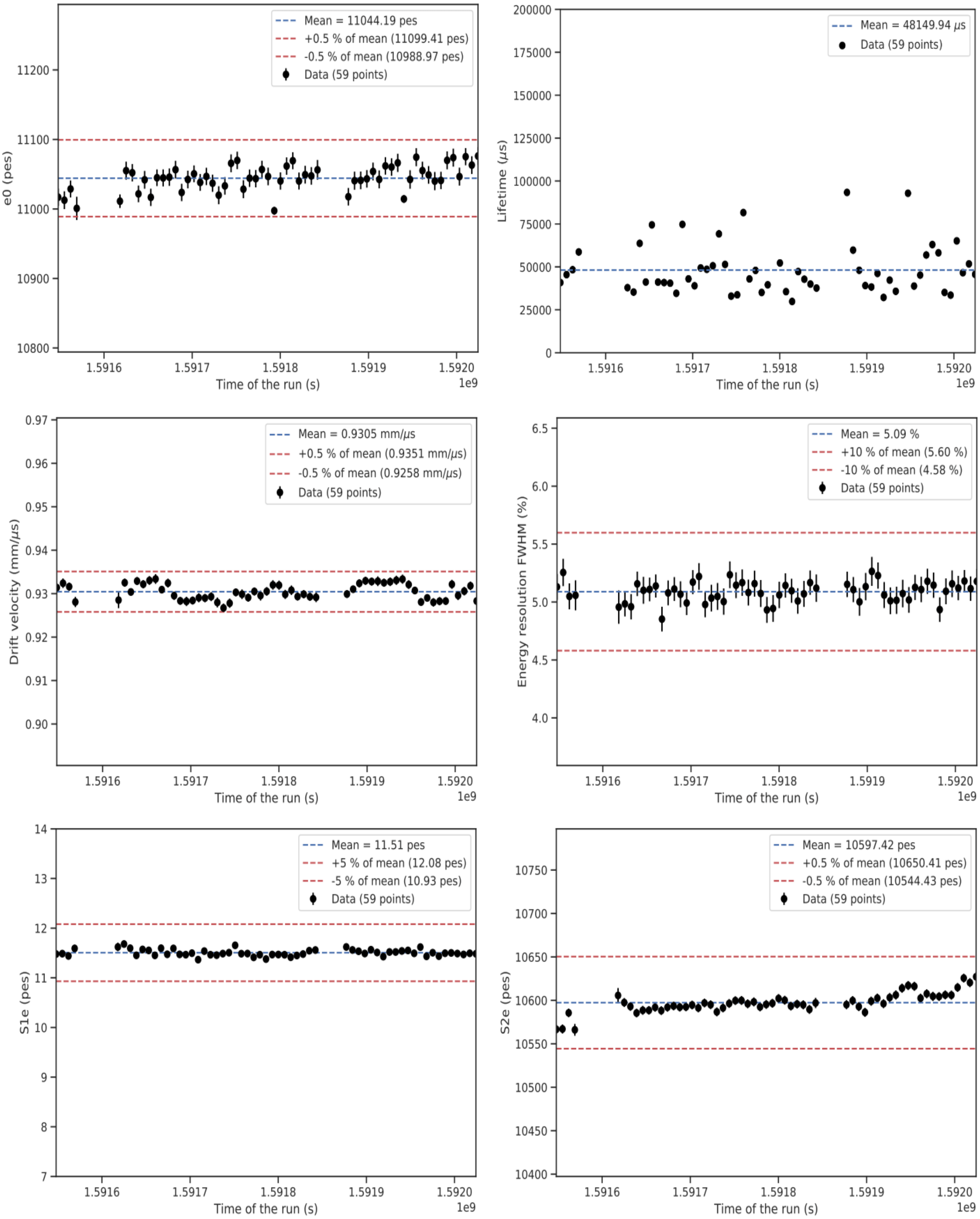

Figure 6.22: Time evolution for the fitting parameters e_0 and lifetime, drift velocity, energy resolution (FWHM), $S1e$ and $S2e$.

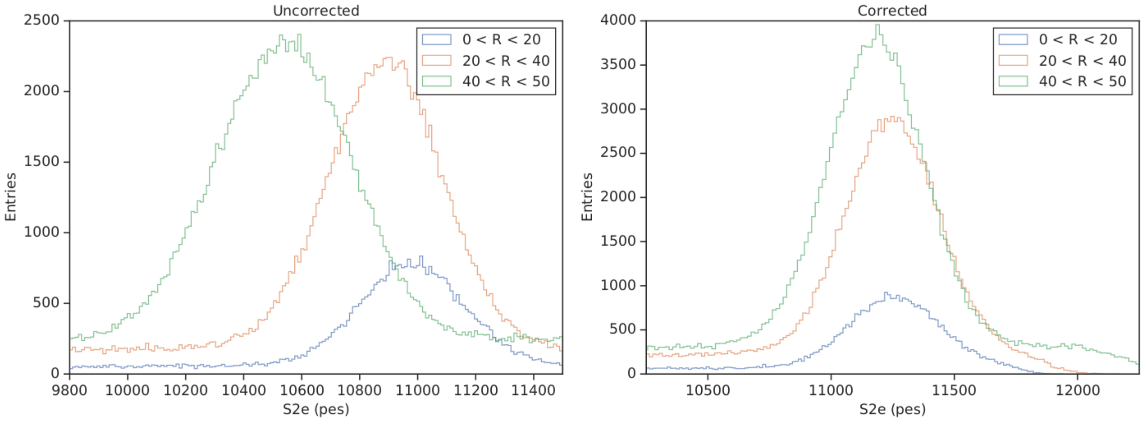

Figure 6.23: Energy distributions for the uncorrected (left) and corrected data (right) for several radial regions of the detector.

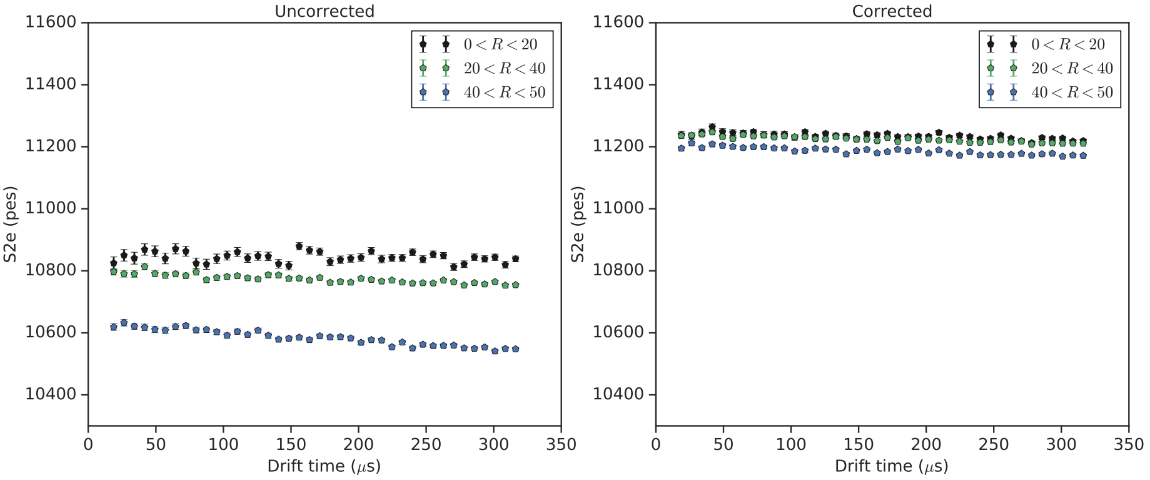

Figure 6.24: Profile of the energy distributions for the uncorrected (left) and corrected data (right) for several radial regions of the detector.

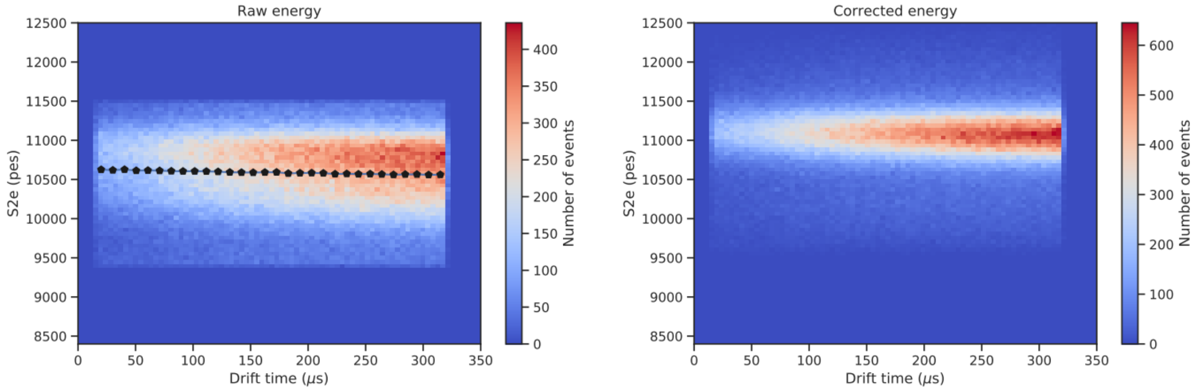

Figure 6.25: Uncorrected (left) and corrected (right) energy distributions as a function of the drift time. The points represent the mean energy value at each bin in the uncorrected energy distribution.

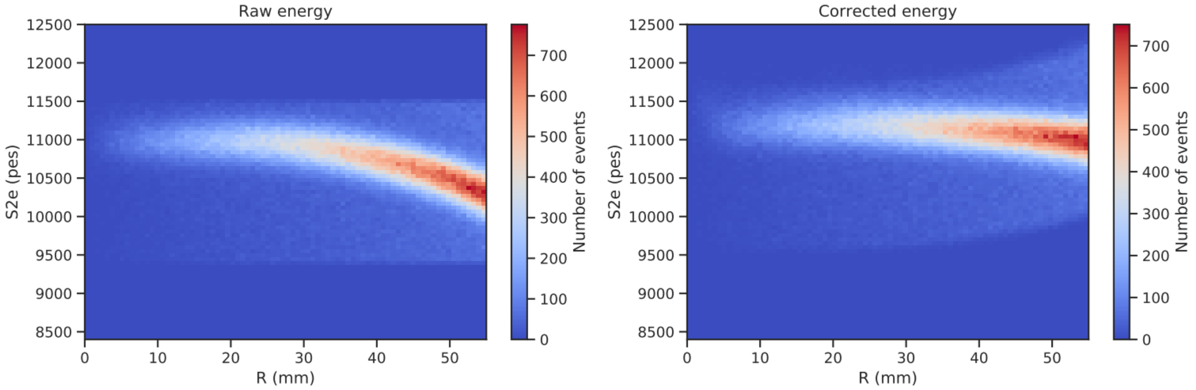

Figure 6.26: Uncorrected (left) and corrected (right) energy distributions as a function of the radial position.

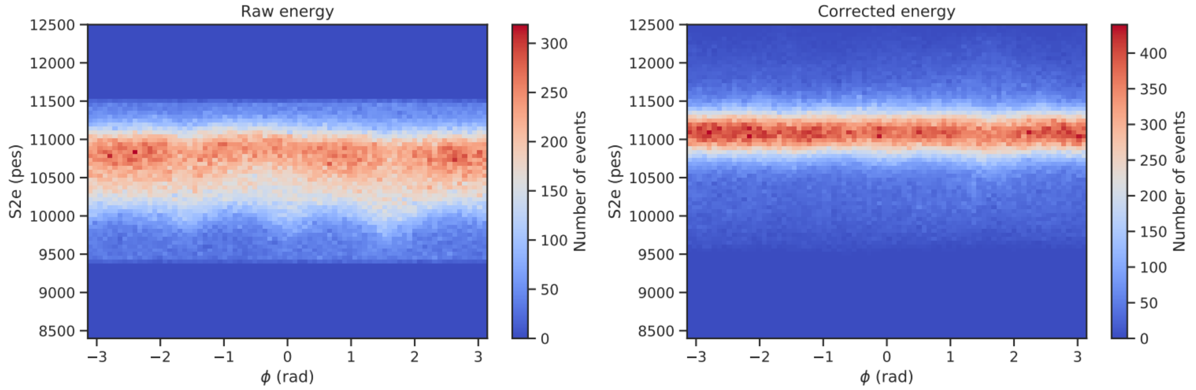

Figure 6.27: Uncorrected (left) and corrected (right) energy distributions as a function of ϕ.

6.6.2 Energy resolution

The default energy resolution assessment in the time evolution computation consists only on a simple gaussian fit to the data. A more accurate procedure, however, is followed to estimate the energy resolution. The details of the improved fit are the following:

1. A gaussian distribution is used to describe the krypton signal and a polynomial function to describe the background:

$$f(x) = N \cdot \exp\left(-\frac{(x-\mu)^2}{2\sigma^2}\right) + g_n(x), \tag{6.7}$$

   where $\boldsymbol{\mu}$ and $\boldsymbol{\sigma}$ are the mean and standard deviation of the distribution, $\mathbf{N}$ is a constant term that multiplies the exponential and $\mathbf{g_n(x)}$ a n-degree polynomial function:

$$g_n(x) = a_0 + a_1 \cdot x + a_2 \cdot x^2 + \ldots a_n \cdot x^n \tag{6.8}$$

   All these parameters will be obtained from the fit.

2. A binned χ^2 fit is performed using the **Probfit** package [113] and the cost function **BinnedChi2** method:

$$
\begin{aligned}
\text{binned\_fit} &= \mathit{BinnedChi2}\,(f(x),\ \text{energy distribution},\ \#\ \text{bins},\ \text{fit range}) \\
\text{ndof} &= \text{binned\_fit}.\mathit{ndof}
\end{aligned}
\tag{6.9}
$$

   An adequate number of bins and fit range is selected to have enough statistics in each bin.

3. The **Minuit** function from the numerical minimisation **Iminuit** package [114] is used like:

$$
\begin{aligned}
m &= \mathit{Minuit}(\text{binned\_fit}, \mu, \sigma, \alpha, \beta, a_n), \\
& m.\mathit{migrad}(),
\end{aligned}
\tag{6.10}
$$

   with $\boldsymbol{\mu}$, $\boldsymbol{\sigma}$, $\boldsymbol{\alpha}$, $\boldsymbol{\beta}$ and $\mathbf{a_n}$ initial guesses for the values.

4. With the result of the fit **m**, the fitted parameters and their uncertainties can be obtained:

$$
\begin{aligned}
\mu &= m.\mathit{values}[0] \quad \text{and} \quad \mu_u = m.\mathit{errors}[0], \\
\sigma &= m.\mathit{values}[1] \quad \text{and} \quad \sigma_u = m.\mathit{errors}[1], \\
N &= m.\mathit{values}[2] \quad \text{and} \quad N_u = m.\mathit{errors}[2], \\
a_n &= m.\mathit{values}[3+n] \quad \text{and} \quad a_{n_u} = m.\mathit{errors}[3+n], \\
\chi^2 &= m.\mathit{fval} \qquad .
\end{aligned}
\tag{6.11}
$$

   The subscript **u** associated to a variable means its uncertainty. The value of $\boldsymbol{\chi}^2$**/ndof** can be obtained from the fit.

Then, the energy resolution R can be defined as:

$$
R = 2.35 \cdot \frac{\sigma}{\mu}
\tag{6.12}
$$

with the following associated error (demonstration in Appendix B):

$$
\delta R = 2.35 \cdot R \sqrt{\left(\frac{\delta\sigma}{\sigma}\right)^2 + \left(\frac{\delta\mu}{\mu}\right)^2 - \frac{2 \cdot \mathrm{Cov}\,(\mu, \sigma)}{\mu \cdot \sigma}}.
\tag{6.13}
$$

6.6.2.1 Background modelling

A careful study was performed to evaluate the dependence of the degree of the polynomial representing the background on the energy resolution. A zeroth, first, second, third and fourth-order polynomial functions were used as input for equation 6.7. In addition, a pure gaussian form was considered as reference. For the purpose of this test, a cut in $R < 50$ mm and $DT < 300$ μs were made. The results for the energy resolution for each function and the respective χ^2/ndof value are shown in figure 6.28. As seen, there is no major dependence on the degree of the polynomial function. The quality of the fits is good since χ^2/ndof is close to 1. Performing a fit using a gaussian distribution does not necessarily produce a reliable result as there is always a background level, as shown by the large χ^2/ndof value. Thus, **a first degree** function was chosen.

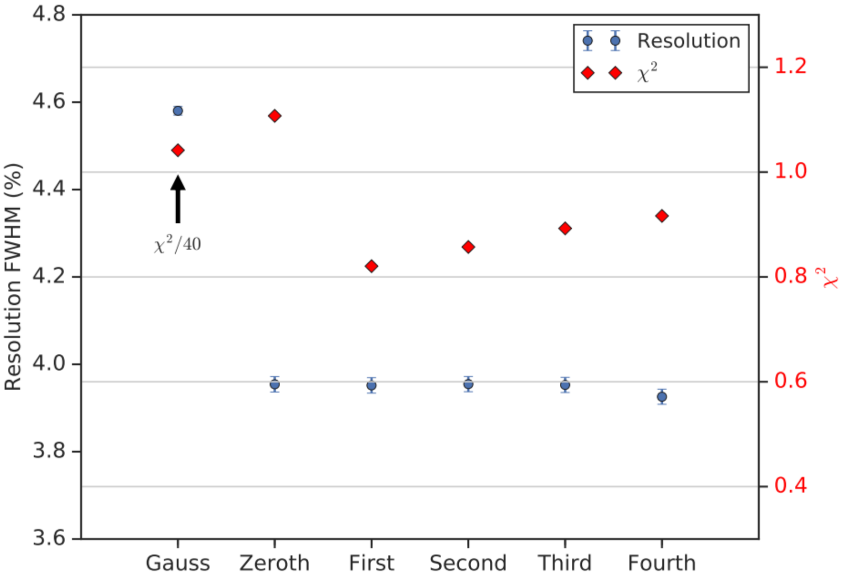

Figure 6.28: Energy resolution dependence, in blue, as a function of the n-degree function used to model the background. The red points correspond to the respective χ^2/ndof value of the fitting. Note that the χ^2/ndof value for the gaussian fit was divided by 40.

6.6.2.2 Fit range

The dependence of the energy resolution on the fit range was tested by choosing a fit interval ranging from $2.0 \cdot \sigma$ to $3.0 \cdot \sigma$, using the same data selection as in the previous section. The results are presented in figure 6.29. As can be seen, there is no significant dependence on the fit range in the energy resolution.

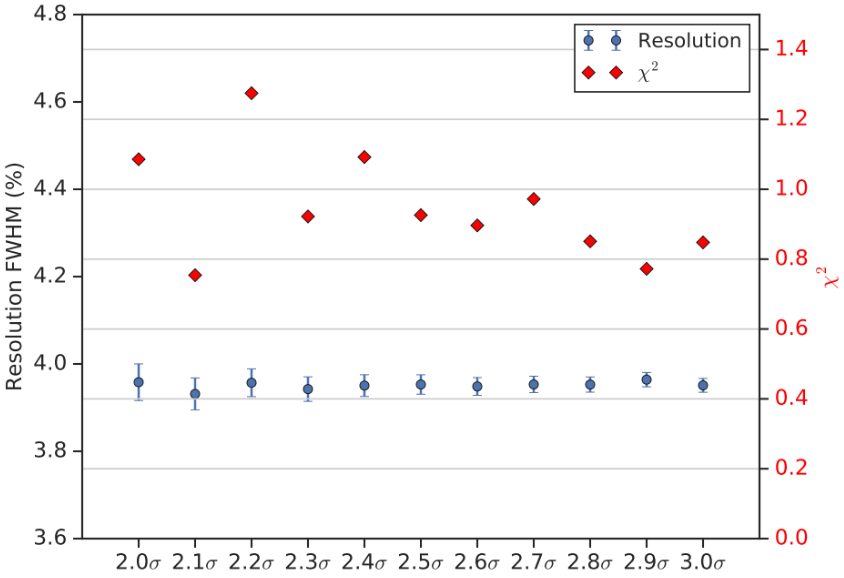

Figure 6.29: Energy resolution dependence, in blue, as a function of the fit range around the peak. The red points correspond to the respective χ^2/ndof value of the fit.

6.6.2.3 Energy resolution across the detector

A conclusiveness test is performed by studying the dependence of the energy resolution on the position of the event on the detector after applying the corrections: if no dependence is observed, then the data is properly corrected. The radial regions are divided in 10 mm slices called *rings*, from 20 to 50 mm, while the drift regions are divided in slices of 50 μs and ranging from 0 to 300 μs. As an example, it is shown in figure 6.30 the fit for $20 < R < 30$ mm for a region near the anode, with $0 < DT < 50$ μs (left), and a region near the cathode, with $250 < DT < 300$ μs (right). Also presented is the expected resolution R_{exp} given in [115] by:

$$\mathrm{R}_{exp} = 2.35\sqrt{\frac{F \cdot w}{E_{Kr}} + \frac{1 + \sigma_{ph}^2}{N_{ph}}} \tag{6.14}$$

where F is the Fano factor, w is the energy to produce an electron-ion pair in xenon, E_{Kr} is the total energy released by the krypton decay, σ_{ph} is related to the fluctuations in the photosensor signal and N_{ph} is the number of detected photoelectrons, i.e., $S2e$. For this case, $F = 0.17$ [90], $w = 21.9$ eV [84–87], $E_{Kr} = 41.5$ keV [109] and $\sigma_{ph} = 0.35$.

The results for the energy resolution and its uncertainty as a function of the radial position (and respective statistical uncertainties) are shown in figure 6.31 and as a function of the drift time interval in figure 6.32. The resolution looks stable in all the regions of the detector and the fluctuations between the values may be due to deficits in statistics in that region (specially for the $0 < R < 20$ mm *ring*).

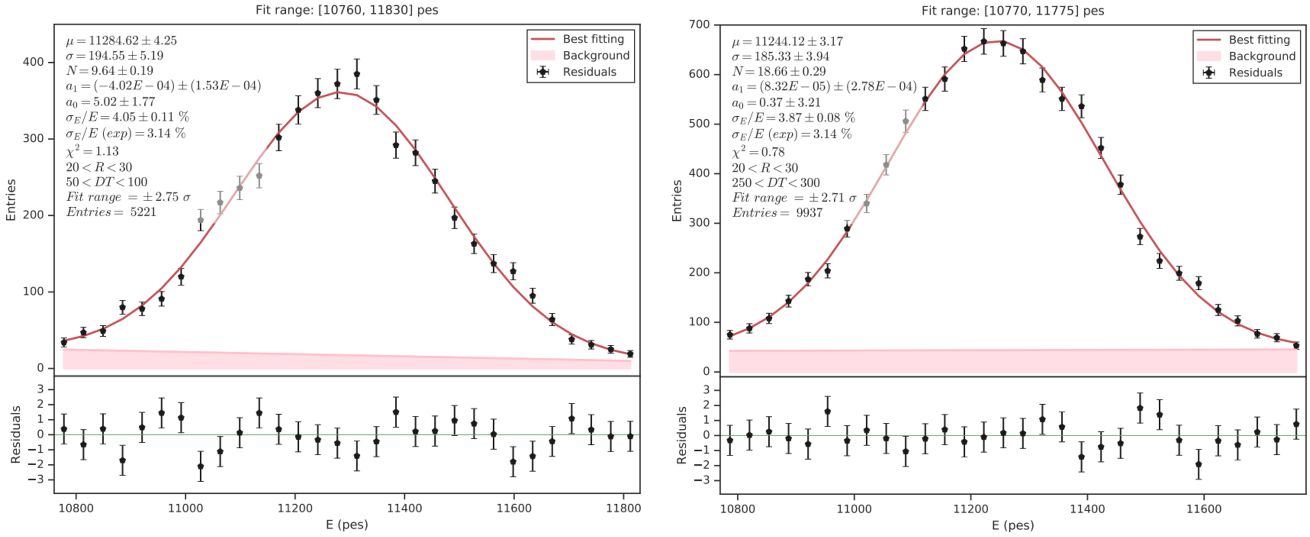

Figure 6.30: Energy distribution and resolution fit for $20 < R < 30$ mm for $0 < DT < 50$ μs (left) and for $250 < DT < 300$ μs (right) with the parameters coming from the fit.

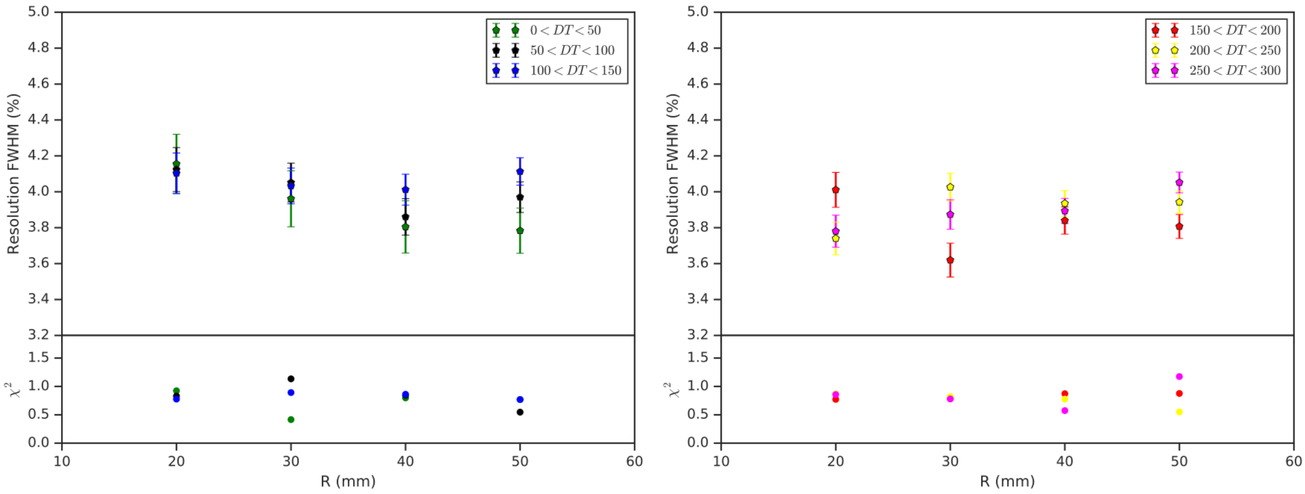

Figure 6.31: Energy resolution as a function of the radial region. Below is the χ^2/ndof value for each of the results.

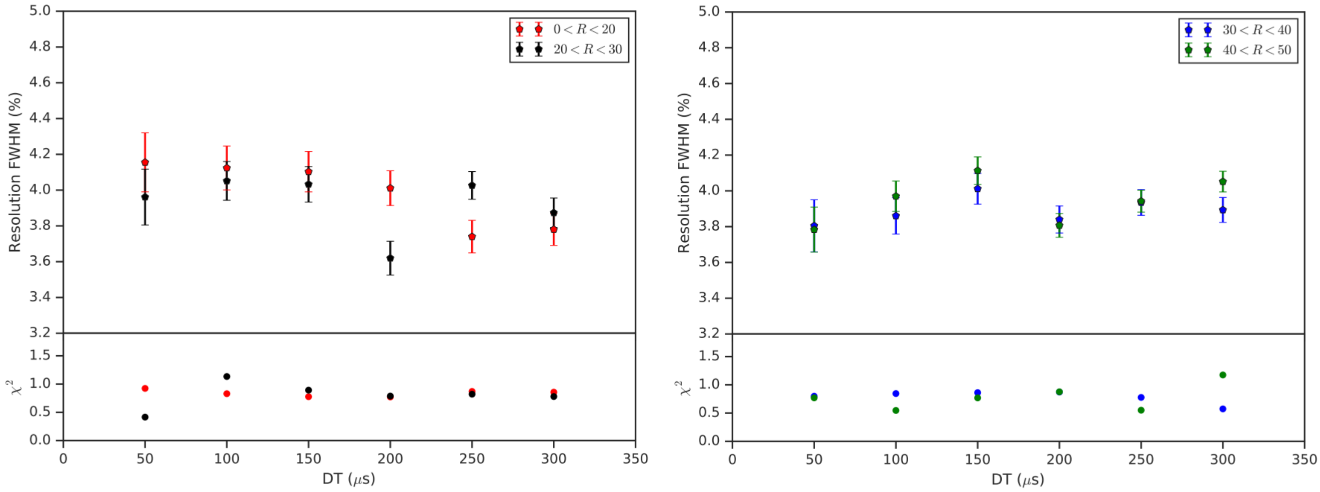

Figure 6.32: Energy resolution as a function of the drift time interval. Below is the χ^2/ndof value for each of the results.

6.6.3 Energy correction factor

Another way to quantify the corrections obtained is to study how they are spread within a correction map. For a particular map bin (i, j), the energy correction factor $\alpha(i, j)$ is defined as follows:

$$\alpha(i,j) = \frac{\max(e_0) - e_0(i,j)}{e_0(i,j)} \tag{6.15}$$

where e_0 is one of the parameters included in the map, and $e_o(i, j)$ is its value in a particular (i, j) bin. Several radial regions (*rings*), with 2.5 mm of width, are defined from 2.5 to 60.0 mm, as evidenced in figure 6.33. As illustrated, the correction factor is uniform until, at least, $R = 40$ mm and then, as expected by the behaviour of the e_0 distribution presented in figure 6.15, it increases for the outer regions.

Then, by averaging the $\alpha(i,j)$ value in each ring, one can get a profile of the corrections as a function of the radial position of the *ring*. Moreover, it is important to acknowledge how additional corrections such as drift time in several intervals and how the time evolution of the e_0 (figure 6.22) can affect the corrections. The following options are considered:

- Without any additional correction.
- With drift time correction at 50, 150 and 300 μs.
- With drift time correction at 50, 150 and 300 μs and with the e_0 value at different time evolution positions, namely at the beginning, middle and end of the run.

The results are shown in figure 6.34. The data correction is around 2 % for the inner regions of the map, until R = 40 mm. Then, the correction value increases up to 7 % for the outer *rings*. For a fiducial region of $R <$ 40 mm, there is no obvious difference between the additional corrections made and the default one. Moreover, the differences between each type of correction are not significant and are only visible for $R >$ 55 mm.

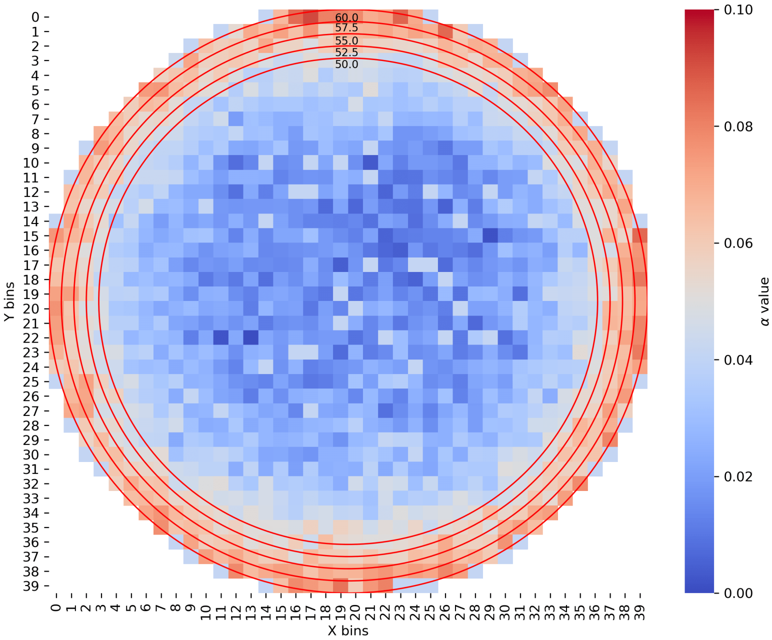

Figure 6.33: Energy correction factor distribution with some example rings.

6.7 Energy variation over time

It was noticed that the energy of the $S2$ signal increased over different runs. This could be related to the decrease in detector's pressure, as seen in figure 6.2, which will increase the Y/P value. Figure 6.35 shows the increase of $S2e$ for runs III and IV as a function of the real time.

As presented in the figure, there is an increase by:

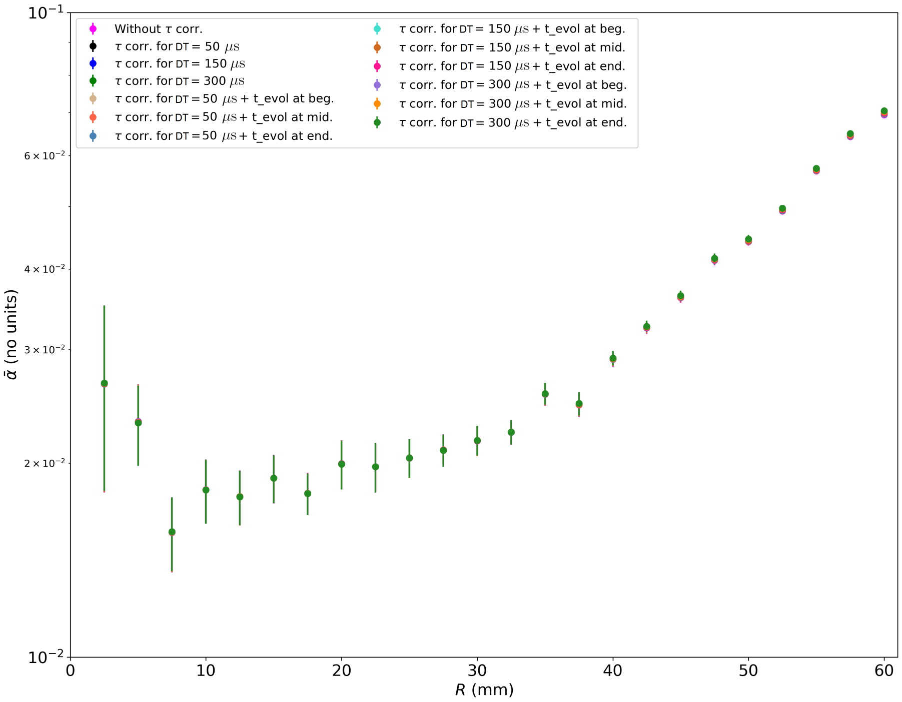

Figure 6.34: Mean value of $\alpha(i,j)$ as a function of the radial position for the uncorrected and corrected distributions.

- $\sim$ 123 pes during run III.
- $\sim$ 172 pes when changing between run III and IV. This unexpected increase might be due to the introduction of another Th source near the EL region (under investigation).
- $\sim$ 170 pes during run IV.

From this figure, one can determine the $S2e$ in the beginning of run III and end of run IV:

$$\begin{aligned} S2e\,(\text{beg.}) &= 10162.41 \pm 3.33 \ \text{pes} \\ S2e\,(\text{end}) &= 10627.24 \pm 5.18 \ \text{pes} \end{aligned} \tag{6.16}$$

and therefore the ratio of $S2e$ in the beginning and end of the plot, which is:

$$\frac{S2e\,(\text{end})}{S2e\,(\text{beg.})} = 1.04574 \pm 0.00061 \tag{6.17}$$

From figure 6.2:

$$\begin{aligned} Y/P\,(\text{beg.}) &= 102 \pm 1 \ \text{ph/e}^-/\text{cm/bar} \\ Y/P\,(\text{end}) &= 108 \pm 1 \ \text{ph/e}^-/\text{cm/bar} \end{aligned} \tag{6.18}$$

and the ratio of Y/P is:

$$\frac{Y/P\,(\text{end})}{Y/P\,(\text{beg.})} = 1.06051 \pm 0.00738 \tag{6.19}$$

As can be seen, the main reason behind the $S2e$ increase is the decrease of the detector's pressure.

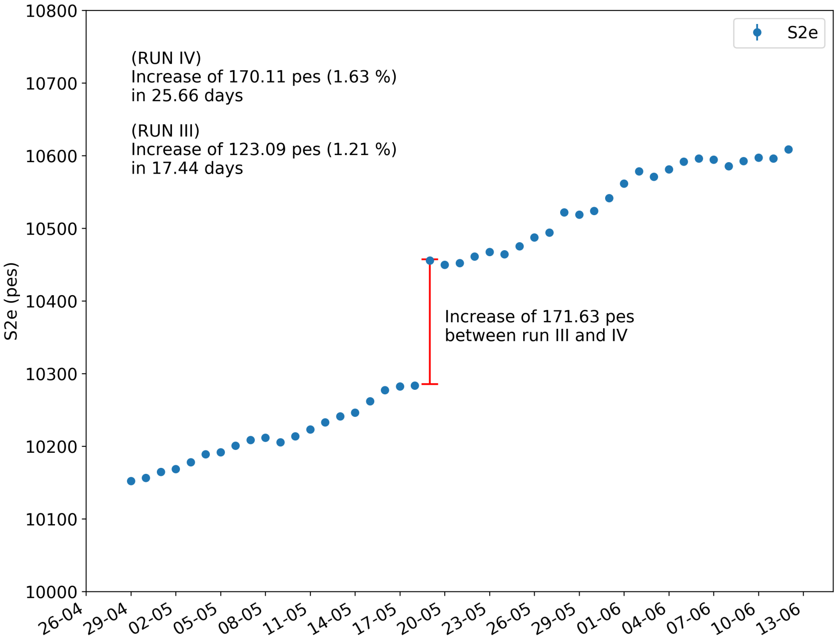

Figure 6.35: $S2e$ increase in runs III and IV as a function of the real time.

6.8 Checking the dependence of the lifetime with the drift time

As previously mentioned, the electron lifetime might depend on all spatial coordinates (X, Y, Z) and, therefore, on the drift time. Although, from previous studies in NEW [109], the dependence on the drift time was neglected, this had to be analysed for NEXT-DEMO++. In order to quantify the dependence of the lifetime on the drift time, the next steps are followed:

1. For each xy bin (of a total of n_{xy} bins), plot the energy distribution over the drift time and, for each bin in each plot, compute the mean energy. The result of the profile will be a mean drift time $(\overline{DT}_{xy})$, a mean energy $(\bar{E}_{xy})$ and an error on the mean energy $(\overline{Eu}_{xy})$.

2. Fit an exponential function to the energy distribution as:

$$f(DT)_{xy} = e_0 \exp\left(-\frac{DT}{\tau}\right), \tag{6.20}$$

   and get the values of e_0, τ and χ^2 of the fit.

3. Compute the residuals r_{DT} for each xy bin as the following:

$$r_{DT} = \frac{\bar{E}_{xy} - f(DT)_{xy}}{\overline{Eu}_{xy}}. \tag{6.21}$$

4. Sum up "point by point" the residuals for all bins and divide by the total number of bins where a fit could be completed, getting an average standardised residuals (R_{DT}):

$$R_{DT} = \frac{\sum_{xy} r_{DT}}{n_{xy}}, \tag{6.22}$$

that will measure how dependent is the lifetime on the drift time: **if R_{DT} is close to 0, then there is no dependence.**

As can be seen in the plot in figure 6.36, there is no significant dependence of the average standardised residuals on the drift time, which proves the initial hypothesis.

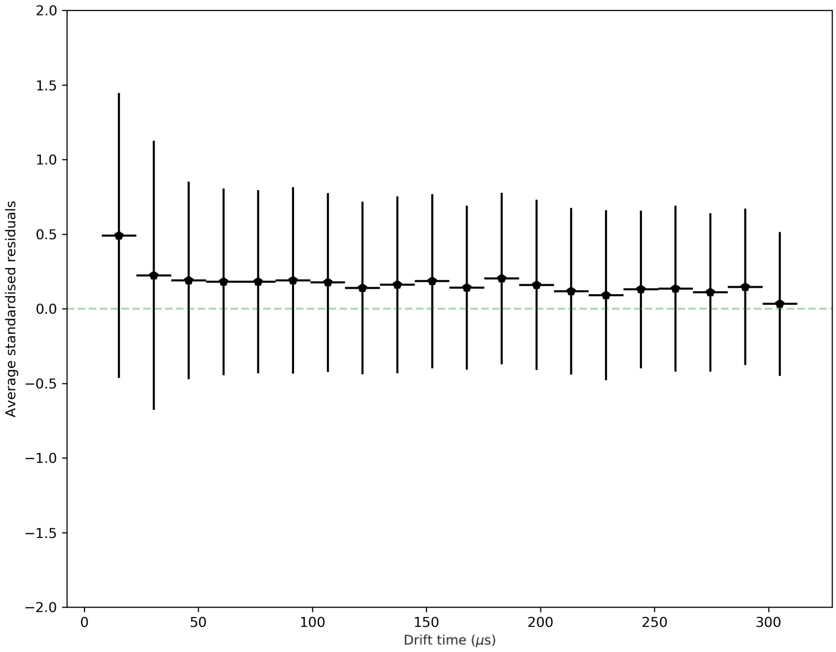

Figure 6.36: R_{DT} results as a function of the drift time.

6.9 Using the correction maps for high-energy peaks analysis

As mentioned in Section 5.4, the high-energy electrons produce long ionisation tracks. In NEXT-DEMO++ there are 3 high-energy radioactive sources, one is ^{137}Cs, with a photopeak at the energy of 0.662 MeV, and two sources of ^{228}Th, with a 1.593 MeV double-escape peak. The position of the sources is presented in figure 6.37.

Figure 6.38 illustrates the track energy spectrum for run IV (left) and run V (right), respectively. The blue lines indicate the usual cut in the Cs and Th peaks.

Figure 6.39 and figure 6.40 presents the reconstructed tracks for the Cs and Th peak from run IV (left) and run V (right), respectively, after applying the corresponding correction maps.

As can be seen, there is an unexpected dependence on the energy of the Z-track length in both peaks known as *Z-effect*, that is quantified as follows:

$$\begin{gathered}\textbf{CS PEAK}\\ \textbf{High EL:}\quad m/b = (-7.31 \pm -0.06)\times 10^{-4}\ \text{mm}^{-1}\\ \textbf{Low EL:}\quad m/b = (-7.33 \pm -0.11)\times 10^{-4}\ \text{mm}^{-1}\end{gathered}\tag{6.23}$$

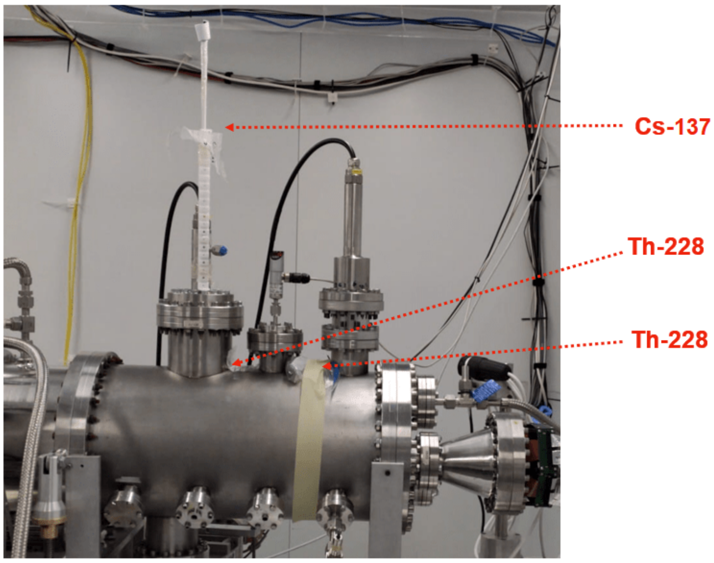

Figure 6.37: Position of the high-energy radioactive sources.

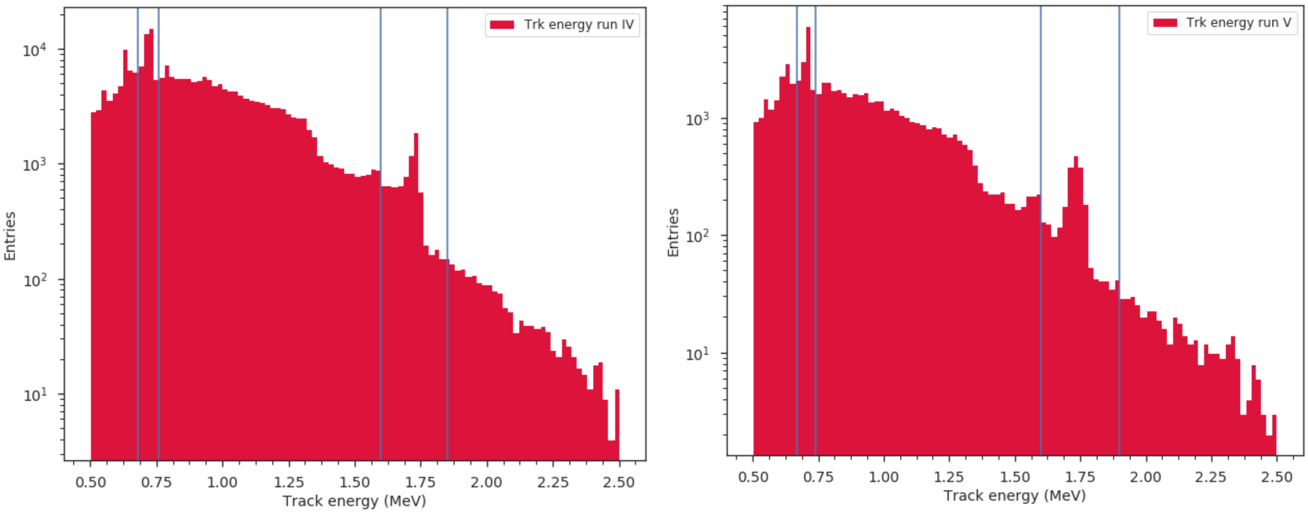

Figure 6.38: Track energy spectrum of the high-energy peaks for run IV (left) and run V (right). The blue lines are placed at 0.68 and 0.76 MeV (Cs peak) and 1.60 and 1.85 MeV (Th peak) for run IV. As for run V, they are placed at 0.67 and 0.74 MeV (Cs peak) and 1.60 and 1.90 MeV (Th peak).

TH PEAK

$$\begin{aligned} \textbf{High EL:}\quad & m/b = (-0.84 \pm -0.07) \times 10^{-4}\ \text{mm}^{-1} \\ \textbf{Low EL:}\quad & m/b = (-6.00 \pm -0.13) \times 10^{-4}\ \text{mm}^{-1} \end{aligned} \tag{6.24}$$

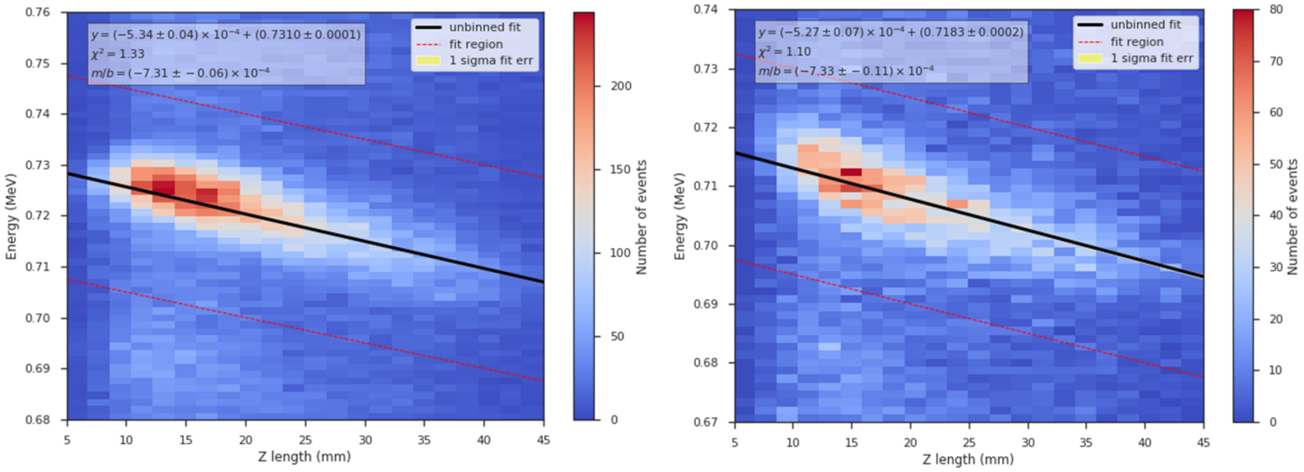

Figure 6.39: Observed *Z-effect* for the Cs peak for run IV (left, high EL) and run V (right, low EL).

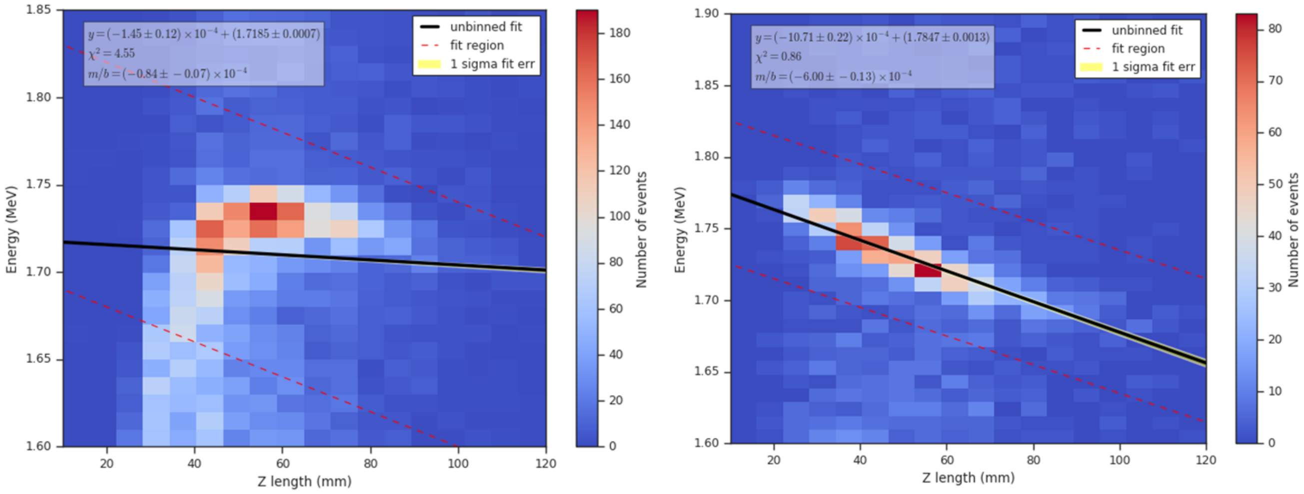

Figure 6.40: Observed *Z-effect* for the Th peak for run IV (left, high EL) and run V (right, low EL).

This apparent correlation between the energy and the track length projected onto the drift axis has different magnitudes in different peaks. The following reasons have already been discarded:

- **Saturation of the PMTs and baseline shift due to the deconvolution algorithm**: this algorithm, as previously mentioned, is used to remove distortions. According to [112], if the response of the PMTs saturates, the deconvolution might lead to a shifted baseline. This results in an error on the integration of the signal that depends on the length of the time integration. However, this effect exists even in low gain regimes, where there is no saturation, and where the baseline shift is not significant.
- **Recombination of the drifting electrons:** the electrons that drift towards the EL plane might recombine with other ions, resulting in less light. After running some simulations, it has been concluded that the recombination radius would need to be of the order of several μm, which is not physically possible for a single ion. Also, if an electron recombined with

an ion, it would produce scintillation light that should be visible between the $S1$ and $S2$ signals. There is no evidence of this light.

- **Light emitted from the SiPMs**: it was proposed that the SiPMs may emit light in a nonlinear way during the scintillation. However, when turning off the tracking plane and using only the energy plane, this effect was still observed.

There are some possible explanations yet to be investigated:

- **Charge-up effect at the EL plane:** an electron may alter the local electric field felt by another crossing electron in the EL gap, giving rise to this effect.
- **Attachment to ionised impurities in the EL gap:** the EL photons may photoionise the TPB deposits used to shift the wavelength of the VUV light. This will result in ions drifting in the EL gap that may recombine with some of the electrons, reducing the overall produced light (although there is a photon production from the recombination).
- **Consequences of the cuts applied in the production of *PMaps/hDSTs* in the SiPMs waveforms**.
- **Non-linearity in the light production due to some other internal detector component**.

In order to study the hypothesis of the photoionisation of the TPB, the detector configuration was changed, namely the crystal ITO + TPB coated anode plate was replaced with an inox mesh, similarly to the gate and the masks of the tracking plane were coated with TPB.

This new detector configuration has already been installed and the data taking is ongoing.

Conclusions and future work

Neutrinos are evasive particles that might contain the key to the matter-antimatter asymmetry. The recent neutrino oscillation experiments have shown that neutrinos do have mass, but their nature, Dirac or Majorana, and absolute mass value are still under investigation.

The observation of a hypothetical neutrinoless double beta decay ($\beta\beta^{o\nu}$) will establish that neutrinos are Majorana particles. A unarguable measurement of this decay's half-life would result in an absolute neutrino mass. There are many experiments working on the search of $\beta\beta^{o\nu}$ using different detectors and different radioactive isotopes. The main requirement of these experiments is an optimal energy resolution due to the fact that the energy of the electrons emitted in the neutrinoless mode would be very close to the electrons in the double beta decay with neutrino emission.

The Neutrino Experiment with a Xenon TPC (NEXT) experiment uses a electroluminescent TPC with high pressure gaseous ^{136}Xe. This isotope has a rather high natural abundance, high Q value and slow double beta decay half-life compared to the two-neutrino mode, and an energy resolution below 0.5 % a¡is achievable at the desired energy.

The NEXT-DEMO++ prototype was designed to test different gas mixtures to be used in the NEXT detectors in order to reduce the diffusion of the drifting electrons. After renewal in 2018, it uses the same sensors as in NEW and NEXT-100, with 3 *Hamamatsu R11410-10* PMTs and 256 *SensL MicroFC-10035-SMT-GP* SiPMs, allowing to fine-tune some details of the under-construction NEXT-100 detector.

◆

The results presented in Chapter 6 show that a cut in the data is required in order to minimise the influence of unwanted events in the detector and remove background. A calibration map must be constructed in order to normalise the energy coming from different regions of the detector. Attention is also give to the time evolution of relevant parameters during run time as this information can be used in improved data correction algorithms.

The use of calibration maps has shown that the energy distribution is successfully corrected as events become independent of the radial position of the interaction point, with a mean value around 11200 pes, while the uncorrected energy distribution had a mean value of around 10500 pes in $0 < R < 20$ mm and 10900 and 11000 pes in the other regions.

Moreover, calibration has stabilised the energy resolution in all regions of the detector, with fluctuations only reflecting lower statistical significance. The detector's response was fitted by a polynomial function within the background, whose degree does not affect the value obtained, and by a gaussian in the range of the signal. The range of the gaussian fit does not affect the obtained values, either.

One important detail, had also been proved for other NEXT detectors like NEW, is that the lifetime of the electrons is not dependent on their drift time. An average lifetime value of 48 ms was measured, a higher value than for other NEXT detectors, indicating that fewer electrons are lost.

The so-called *Z-effect*, visible in NEW, is also present in NEXT-DEMO++. This effect is under investigation in a recent update of the detector in which the anode coated with TPB has been replaced by a mesh.

As seen in Section 6.3 and in the lifetime value obtained, the krypton peak position does not depend on the electrons' lifetime. However, it depends on the radial position, decreasing for a higher radial selection. A fixed cut in $S2e$ is applied to all regions of that detector, which must include the krypton peak in every region of the detector. Although this cut is suitable for the $40 < R < 60$ mm region, it may not be optimal for other regions ($0 < R < 20$ mm). Accordingly, it must be considered in the future:

1. **An implementation of a dynamic $S2e$ cut**: create an algorithm that compares the $S2e$ in different regions of the detector and produces an optimal cut for each region.

Other possible studies include the:

2. **Monte Carlo simulation of the Y/P yield in parallel with an experimental setup to assess the dependence of the EL yield on the pressure and electrical conditions**: previous studies [116] show that there might be some dependencies with pressure in the amplification parameters, believed to be fixed, of the equation presented in Section 6.2.

Appendix A

More present experiments on $\beta\beta^{0\nu}$

A.1 CANDLES

The experiment Calcium fluoride for the study of Neutrinos and Dark matters by Low Energy Spectrometer (CANDLES) uses a pure cube of CaF_2 scintillator immersed in a liquid scintillator that surrounds all the detector for background rejection. The isotope ^{48}Ca has the high Q value of 4.27 MeV, an advantage while comparing to the natural radioactive backgrounds. The schematics of the experiment are shown in figure A.1 [117].

The CANDLES III, the newer detector, consists of 96 CaF_2 scintillators, with a total mass of 305 kg and suspended by wires from the ceiling, and total liquid scintillator volume of 2 m^3. All the modules are installed in tank full of water with 3 m of diameter and 4 m of height [117]. The external background is strongly rejected due to the 4π shielding. The expected sensitivity is $m_{\beta\beta} = 0.5$ eV.

The main problem with this experiment is that the natural abundance of the isotope ^{48}Ca is a low 0.187 % and the enrichment process is complicated.

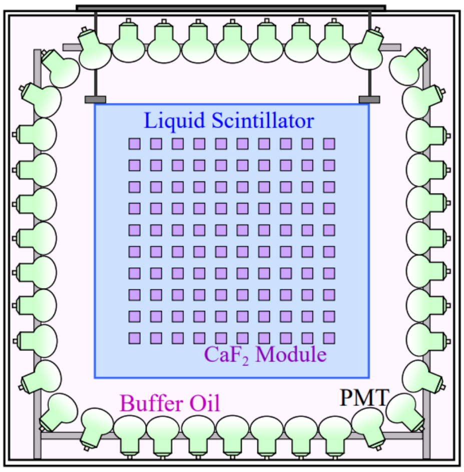

Figure A.1: Design of the CANDLES system [118].

A.2 LUCIFER

The Low-background Underground Cryogenic Installation For Elusive Rates (LUCIFER) is an experiment located in LNGS, in Italy, that uses the idea of CUORE bolometric technique with the light detection method used in cryogenic dark matter experiments [119]. It uses both the isotope ^{82}Se in ZnSe scintillating bolometers and ^{100}Mo in $ZnMoO_4$ scintillating bolometers.

It consists of 36 cylindrical crystals with 45 mm of diameter and 55 mm of height enriched $\sim$ 95 %. Each crystal has a Ge disk, with 44 mm of diameter and 180 μm of thickness, that acts as a light detector. The schematics of the detector are shown in A.2.

The half-life limits and effective neutrino masses, for the different bolometers, are summarised in table A.1, obtained from [120].

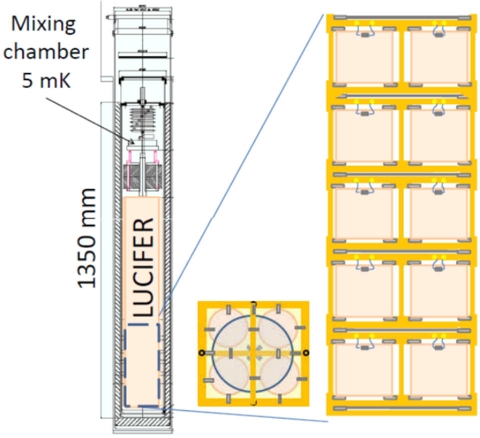

Figure A.2: Schematics of the LUCIFER detector [119].

Table A.1: Half-life lower limit value ($T^{0\nu}_{1/2}$), with 90 % CL, and relative effective neutrino masses ($\langle m_{\beta\beta}\rangle_{rel}$), with respect to several scintillating bolometer crystals, at different running times.

Bolometer	$Q_{\beta\beta}$ (keV)	FWHM (keV)	Run. time (yrs)	$T^{0\nu}_{1/2}$ ($\times 10^{26}$ yrs)	$\langle m_{\beta\beta}\rangle_{rel}$ (meV)
ZnSe	2997	16.5	5	> 0.6	65 / 194
ZnSe	2997	16.5	10	> 1.2	45 / 138
$ZnMoO_4$	3034	7	5	> 0.3	60 / 170
$ZnMoO_4$	3034	7	10	> 0.6	42 / 120

A.3 COBRA

The Cadmium Zinc Telluride 0-Neutrino Double-Beta (COBRA) experiment is located in LNGS, in Italy, and it is a different approach for the neutrinoless double beta decay searches. It uses room-temperature semiconductors like CdZnTe with good energy resolution, high natural abundance (^{130}Te) and high Q value of 2.8 MeV (^{116}Cd) [121].

The crystals act as both source and detection medium and has nine isotopes that have double beta decay. The detectors are placed in a coplanar-grid design similar to a Frisch grid in the ionisation chambers, like shown in figure A.3.

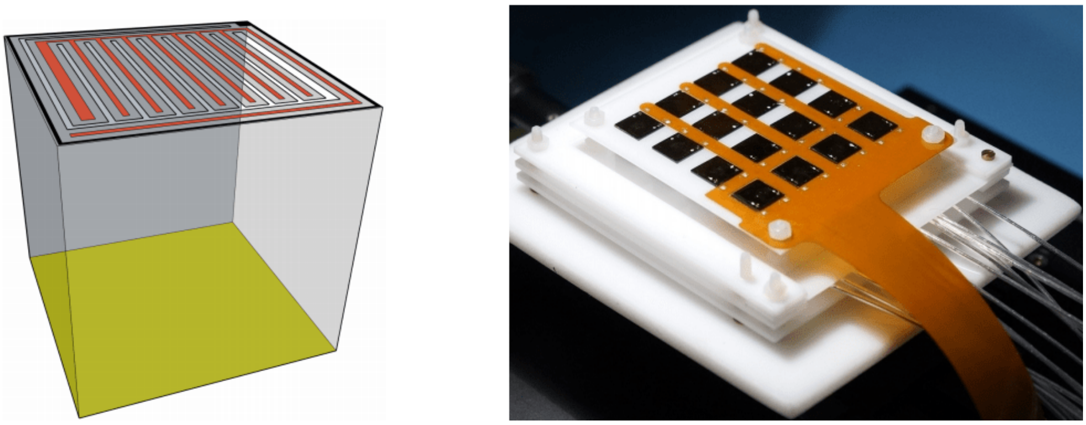

Figure A.3: Sketch of a coplanar-grid detector (left) and photo of a detector layer (right). Adapted from [122].

The results from this experiment are summarised in table A.2.

Table A.2: Lower half-life limits for the neutrinoless double beta decays in several isotopes and respective $Q_{\beta\beta}$ value in the COBRA experiment. Adapted from [123].

Isotope	$Q_{\beta\beta}$ (keV)	$T^{0\nu}_{1/2}$ ($\times 10^{21}$ yrs, with 90% CL)
^{70}Zn	997	$> 6.8 \times 10^{-3}$
^{114}Cd	543	> 1.6
^{116}Cd	2814	> 1.1
^{128}Te	867	> 1.9
^{130}Te	2528	> 6.1

A.4 DCBA and DCBA/MTD

The concept behind the Drift Chamber Beta-ray Analyzer (DCBA) experiment relies in a magnetised drift chamber that can reconstruct the path of a particle that interacts in a medium, since the kinetic energy and the momentum are derived from the curvature of the trajectory. The detector is shown in figure A.4.

The expected energy resolution for the latest detector (DCBA-T3) is 3.4 % for the isotope ^{150}Nd [125] and the tentative half-life limits and effective neutrino masses are summarised in table A.3.

The collaboration is now planning a future experiment called Drift Chamber Beta-ray Analyzer and Magnetic Tracking Detector (DCBA/MTD), that wants to achieve an effective neutrino

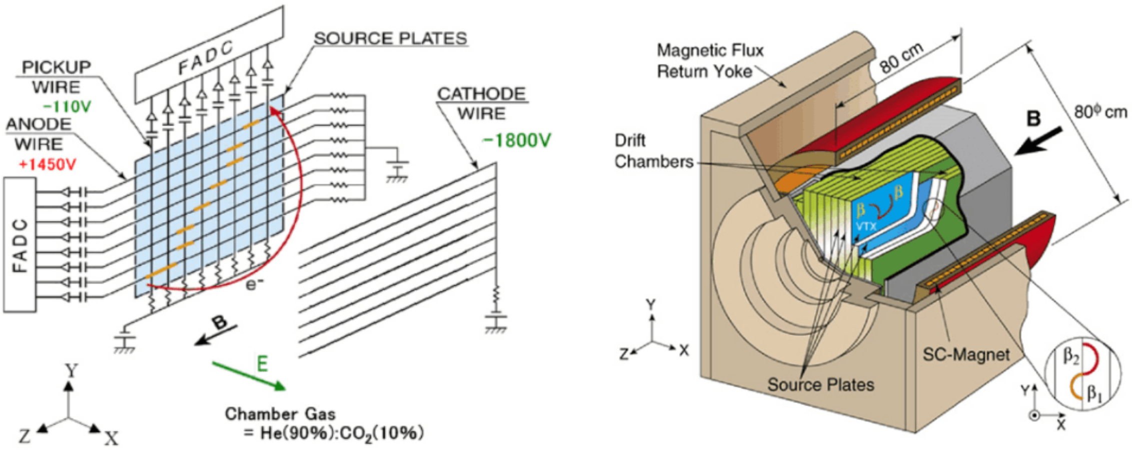

Figure A.4: Detection principle (left) and schematics of the latest detector - DCBA-T3 (right). Adapted from [124].

Table A.3: Lower half-life limits and effective neutrino mass in the DCBA experiment for the neutrinoless double beta decays in several isotopes. Adapted from [125].

Isotope	$T^{0\nu}_{1/2}$ ($\times 10^{26}$ yrs)	$\langle m_\nu \rangle$ (eV)
5.6 % enr. of ^{150}Nd	$< 9 \times 10^{-2}$	0.06
80 % enr. of ^{150}Nd	< 1	0.02
90 % enr. of ^{100}Mo	< 2	0.07
90 % enr. of ^{82}Se	< 3	0.04

mass of 30 meV, which corresponds to an half-life of 10^{26} years [126]. The conceptual design of the new detector is presented in figure A.5.

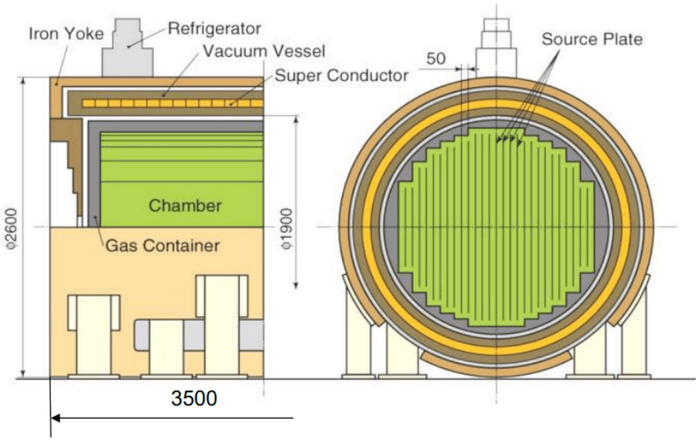

Figure A.5: Conceptual drawing of DCBA/MTD, where a super conducting solenoid will be able to create a uniform magnetic field of 2.4 kG [126].

A.5 MOON

The Molybdenum Observatory Of Neutrinos (MOON) collaboration is a spectroscopic experiment for detecting individual $\beta\beta$ rays. The detectors are separated from the double beta sources to measure the decays from the isotopes ^{100}Mo and ^{82}Se and consist of a stack of multi-layer modules. Each module is made of a scintillator plate to measure energy and time, a thin double beta source film and two thin detector layers to identify the particles and their position. One full detector consists of 15 modules, with 2 kg of the double beta isotopes. The detector is shown in figure A.6.

An energy resolution of 3 % (FWHM) at 3 MeV was already achieved in the first prototype.

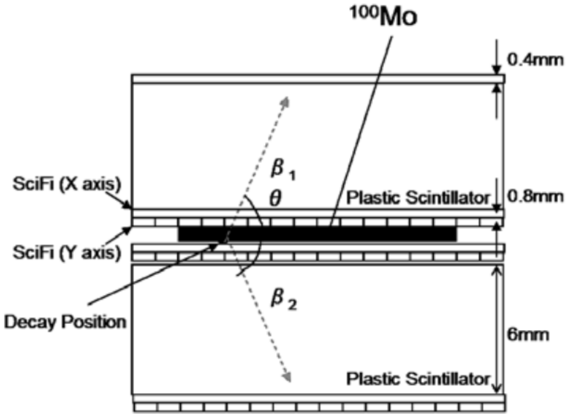

Figure A.6: A part of cross-section of MOON-1 detector [127].

A.6 FLARES

The Flexible Scintillation Light Apparatus for Rare Event Searches (FLARES) collaboration focused on the field of rare events searches. Currently is working on a prototype scintillating detector to enhance the collection of scintillation photons emitted by ultra-pure crystals. It aims to achieve an energy resolution of 2 % (FWHM), but 1 % is achievable [128].

The project is now focusing on the crystals $CaMoO_4$ and $CdWO_4$, but the latter has a higher light yield. The detector is based on Silicon Drift Detectors (SDDs), which have an high performance, to collected the emitted light. The major advantages are the flexibility of the used isotope, easy mass scalability, good energy resolution and high achievable purity materials. The main directions of research are the optimisation of the scintillation properties of the crystals and the development of the SDDs [129]. The configuration of the scintillators and a drawing of the SDDs matrix are shown in figure A.7.

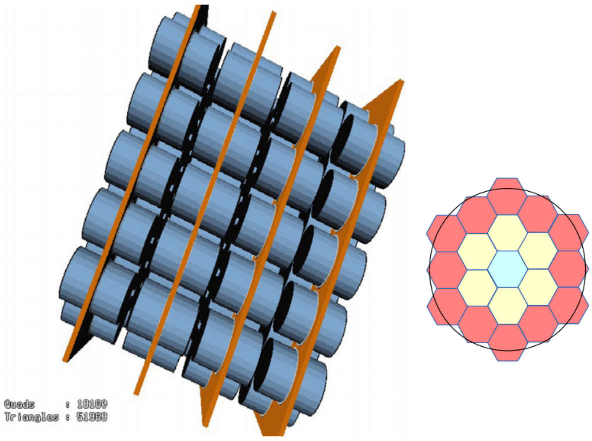

Figure A.7: Array of the scintillators (left) and one of the configurations of the SDDs matrix (right) [130].

A.7 AMoRE

The Advanced Mo-based Rare process Experiment (AMoRE) experiment [131] located in Y2L, in South Korea, that is using scintillating $CaMoO_4$ crystals to search for neutrinoless double beta decays using the isotope ^{100}Mo, with an enrichment up to 96 %. The simultaneous detection of phonons and photons from the scintillation is the proposed technique to reject the natural radioactive background. When there is an interaction in the scintillator, the produced heat and light are measured using MCCs and the signal are collected by SQUIDs.

The projected sensitivity, after 250 kg·yr of data acquisition, is $T^{0\nu}_{1/2} \sim 3 \times 10^{26}$ years, which implies an effective neutrino mass of $0.02 - 0.06$ eV.

Some photos of the prototype detector, as well as it individual parts, are shown in figure A.8.

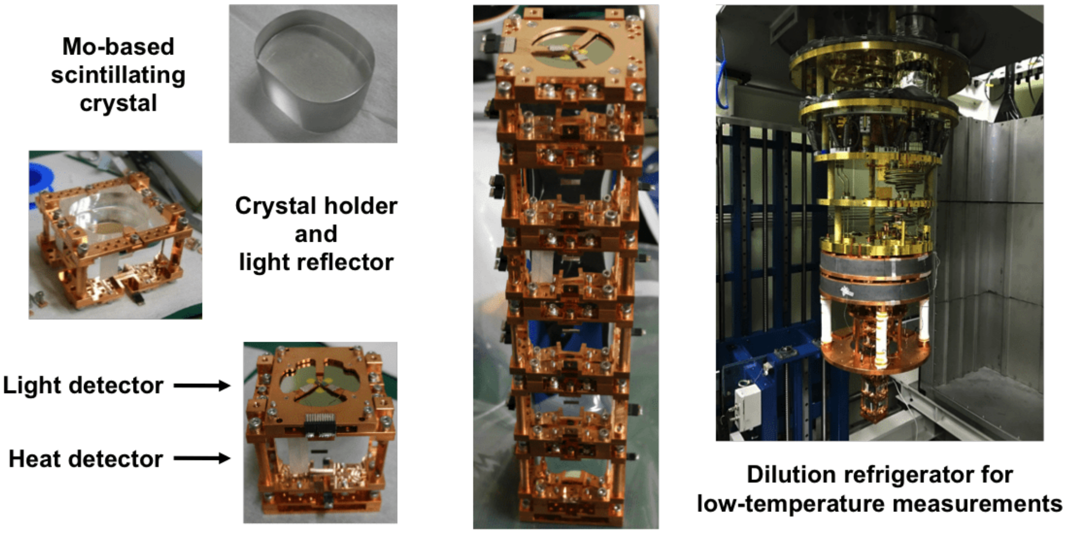

Figure A.8: Some parts of the AMoRE-Pilot, the pilot phase of the project [132].

Appendix B

Demonstrations

B.1 Error on the computed energy resolution

If the energy resolution R is defined as:

$$\mathrm{R} = 2.35 \cdot \frac{\sigma}{\mu}$$

with σ and μ as the standard deviation and mean value (centroid) of a gaussian fit distribution, the error on the computed value will be:

$$\delta\mathrm{R} = \sqrt{\left(\frac{\partial\sigma}{\partial\mathrm{R}}\delta\sigma\right)^2 + \left(\frac{\partial\mu}{\partial\mathrm{R}}\delta\mu\right)^2 + 2\cdot\mathrm{Cov}\left(\mu,\sigma\right)\left(\frac{\partial\sigma}{\partial\mathrm{R}}\right)\left(\frac{\partial\mu}{\partial\mathrm{R}}\right)}$$

$$= \sqrt{\left(\frac{2.35}{\mu}\delta\sigma\right)^2 + \left(-\frac{2.35\cdot\sigma}{\mu^2}\delta\mu\right)^2 + 2\cdot\mathrm{Cov}\left(\mu,\sigma\right)\left(\frac{2.35}{\mu}\right)\left(\frac{1}{\mu}\right)\left(-\frac{\sigma}{\mu^2}\right)}$$

$$= \sqrt{\left(\frac{2.35\cdot\sigma}{\mu}\right)^2 \cdot \left(\left(\frac{\delta\sigma}{\sigma}\right)^2 + \left(\frac{\delta\mu}{\mu}\right)^2 - \frac{2\cdot\mathrm{Cov}\left(\mu,\sigma\right)}{\mu\cdot\sigma}\right)}$$

$$= \underbrace{\left|\frac{2.35\cdot\sigma}{\mu}\right|}_{\mathrm{R}} \sqrt{\left(\frac{\delta\sigma}{\sigma}\right)^2 + \left(\frac{\delta\mu}{\mu}\right)^2 - \frac{2\cdot\mathrm{Cov}\left(\mu,\sigma\right)}{\mu\cdot\sigma}}$$

Hence:

$$\delta\mathrm{R} = \mathrm{R}\cdot\sqrt{\left(\frac{\delta\sigma}{\sigma}\right)^2 + \left(\frac{\delta\mu}{\mu}\right)^2 - \frac{2\cdot\mathrm{Cov}\left(\mu,\sigma\right)}{\mu\cdot\sigma}} \tag{B.1}$$

Bibliography

[1] C. L. Cowan, F. Reines, F. B. Harrison, H. W. Kruse, A. D. McGuire, Detection of the Free Neutrino: a Confirmation, Science 124 (3212) (1956) 103–104. doi:10.1126/science.124.3212.103.

[2] F. Reines, C. L. Cowan, The neutrino, Nature 178 (1956) 446–449. doi:10.1038/178446a0.

[3] R. Z. Funchal, B. Schmauch, G. Giesen, The physics of neutrinos, High Energy Physics - Experiment (2013). arXiv:1308.1029.

[4] K. Kodama, et al., Observation of tau neutrino interactions, Phys. Lett. B 504 (2001) 218–224. doi:10.1016/S0370-2693(01)00307-0.

[5] K. S. Krane, Introductory nuclear physics, Wiley, New York, NY, 1988.

[6] Y. Fukuda, et al., Evidence for Oscillation of Atmospheric Neutrinos, Phys. Rev. Lett. 81 (1998) 1562–1567. doi:10.1103/PhysRevLett.81.1562.

[7] A. Smirnov, Towards the solution of the solar neutrino problem, Nuclear Physics B - Proceedings Supplements 77 (1-3) (1999) 98–107. doi:10.1016/s0920-5632(99)00404-1.

[8] T. Kajita, Discovery of neutrino oscillations, Reports on Progress in Physics 69 (6) (2006) 1607–1635. doi:10.1088/0034-4885/69/6/r01.

[9] J. J. Gomez-Cadenas, J. Martin-Albo, M. Mezzetto, F. Monrabal, M. Sorel, The search for neutrinoless double beta decay, arXiv e-prints (Sep 2011). arXiv:1109.5515.

[10] E. Komatsu, et al., Seven-Year Wilkinson Microwave Anisotropy Probe (WMAP) Observations: Cosmological Interpretation, The Astrophysical Journal Supplement Series 192 (2) (2011) 18. doi:10.1088/0067-0049/192/2/18.

[11] K. N. and, Review of particle physics, Journal of Physics G: Nuclear and Particle Physics 37 (7A) (2010) 075021. doi:10.1088/0954-3899/37/7a/075021.

[12] R. Emami, et al., Evidence of Neutrino Enhanced Clustering in a Complete Sample of Sloan Survey Clusters, Implying $\sum m_\nu = 0.119 \pm 0.034$ eV, arXiv e-prints (2017). arXiv:1711.05210.

[13] V. Lobashev, et al., Direct search for mass of neutrino and anomaly in the tritium beta-spectrum, Nuclear Physics B - Proceedings Supplements 87 (1) (2000) 275 – 277. `doi:10.1016/S0920-5632(00)00678-2`.

[14] C. Kraus, et al., Final results from phase ii of the mainz neutrino mass search in tritium β decay, The European Physical Journal C 40 (4) (2005) 447–468. `doi:10.1140/epjc/s2005-02139-7`.

[15] K. Olive, Review of particle physics, Chinese Physics C 38 (9) (2014) 698. `doi:10.1088/1674-1137/38/9/090001`.

[16] A. Osipowicz, et al., KATRIN: A next generation tritium beta decay experiment with sub-eV sensitivity for the electron neutrino mass, arXiv e-prints (2001). `arXiv:hep-ex/0109033`.

[17] Miquel Nebot Guinot, The NEXT path to neutrino inverse hierarchy, Ph.D. thesis, Departament de Física Atòmica, Molecular i Nuclear (2017).

[18] M. Drewes, The Phenomenology of Right Handed Neutrinos, International Journal of Modern Physics E 22 (03 2013). `doi:10.1142/S0218301313300191`.

[19] E. Majorana, L. Maiani, A symmetric theory of electrons and positrons, Springer Berlin Heidelberg, Berlin, Heidelberg, 2006, Ch. 9, pp. 201–233. `doi:10.1007/978-3-540-48095-2_10`.

[20] P. Hernandez, Neutrino physics, CERN (2010). `arXiv:1010.4131`.

[21] M.-C. Chen, TASI 2006 Lectures on Leptogenesis, `https://ui.adsabs.harvard.edu/abs/2007hep.ph....3087C` (Mar 2007).

[22] A. D. Sakharov, Violation of CP Invariance, C asymmetry, and baryon asymmetry of the universe, Pisma Zh. Eksp. Teor. Fiz. 5 (1967) 32–35. `doi:10.1070/PU1991v034n05ABEH002497`.

[23] G. A. White, The Sakharov conditions, in: A Pedagogical Introduction to Electroweak Baryogenesis, 2053-2571, Morgan & Claypool Publishers, 2016, pp. 2–1 to 2–2. `doi:10.1088/978-1-6817-4457-5ch2`.

[24] A. Atre, V. Barger, T. Han, Upper bounds on lepton-number violating processes, Physical Review D 71 (11) (Jun 2005). `doi:10.1103/physrevd.71.113014`.

[25] M. Goeppert-Mayer, Double Beta-Disintegration, Phys. Rev. 48 (1935) 512–516. `doi:10.1103/PhysRev.48.512`.

[26] M. G. Inghram, J. H. Reynolds, Double Beta-Decay of Te^{130}, Phys. Rev. 78 (1950) 822–823. `doi:10.1103/PhysRev.78.822.2`.

[27] S. R. Elliott, A. A. Hahn, M. K. Moe, Direct evidence for two-neutrino double-beta decay in $^{82}\mathrm{Se}$, Phys. Rev. Lett. 59 (1987) 2020–2023. `doi:10.1103/PhysRevLett.59.2020`.

[28] M. Tanabashi, et al., Review of particle physics, Phys. Rev. D 98 (2018) 030001. `doi:10.1103/PhysRevD.98.030001`.

[29] R. Arnold, et al., Measurement of the double-beta decay half-life and search for the neutrinoless double-beta decay of ^{48}Ca with the NEMO-3 detector, Physical Review D 93 (11) (Jun 2016). `doi:10.1103/physrevd.93.112008`.

[30] C. Patrignani, et al., Review of Particle Physics, Chin. Phys. C40 (10) (2016) 100001. `doi:10.1088/1674-1137/40/10/100001`.

[31] C. Alduino, et al., Measurement of the two-neutrino double-beta decay half-life of ^{130} Te with the CUORE-0 experiment, The European Physical Journal C 77 (1) (Jan 2017). `doi:10.1140/epjc/s10052-016-4498-6`.

[32] J. B. Albert, et al., Improved measurement of the $2\nu\beta\beta$ half-life of ^{136}Xe with the EXO-200 detector, Physical Review C 89 (1) (Jan 2014). `doi:10.1103/physrevc.89.015502`.

[33] W. H. Furry, On Transition Probabilities in Double Beta-Disintegration, Phys. Rev. 56 (1939) 1184–1193. `doi:10.1103/PhysRev.56.1184`.

[34] Javier Muñoz Vidal, Calibration and background model of the NEW detector at the LSC, Ph.D. thesis, Departament de Física Atòmica, Molecular i Nuclear (Apr 2018).

[35] M. Doi, T. Kotani, E. Takasugi, Double Beta Decay and Majorana Neutrino, Progress of Theoretical Physics Supplement 83 (1985) 1–175. `doi:10.1143/PTPS.83.1`.

[36] J. Kotila, F. Iachello, Phase-space factors for double-β decay, Physical Review C 85 (3) (Mar 2012). `doi:10.1103/physrevc.85.034316`.

[37] M. Mirea, T. Pahomi, S. Stoica, Values of the phase space factors involved in double beta decay, Romanian Reports in Physics 67 (2015) 872–889. `doi:10.1063/1.4934913`.

[38] J. Menéndez, A. Poves, E. Caurier, F. Nowacki, Disassembling the nuclear matrix elements of the neutrinoless $\beta\beta$ decay, Nuclear Physics A 818 (3-4) (2009) 139–151. `doi:10.1016/j.nuclphysa.2008.12.005`.

[39] J. Hyvärinen, J. Suhonen, Nuclear matrix elements for $0\nu\beta\beta$ decays with light or heavy Majorana-neutrino exchange, Phys. Rev. C 91 (2015) 024613. `doi:10.1103/PhysRevC.91.024613`.

[40] J. Barea, J. Kotila, F. Iachello, $0\nu\beta\beta$ and $2\nu\beta\beta$ nuclear matrix elements in the interacting boson model with isospin restoration, Physical Review C 91 (3) (Mar 2015). `doi:10.1103/physrevc.91.034304`.

[41] L. S. Song, J. M. Yao, P. Ring, J. Meng, Nuclear matrix element of neutrinoless double-β decay: Relativity and short-range correlations, Physical Review C 95 (2) (Feb 2017). `doi:10.1103/physrevc.95.024305`.

[42] A. V. Tikhomirov, Centrifugal enrichment of stable isotopes and modern physical experiments, Czechoslovak Journal of Physics 50 (4) (2000) 577–580. doi:10.1023/A:1022809128791.

[43] A. S. Barabash, Brief review of double beta decay experiments, Particle Physics at the Year of Centenary of Bruno Pontecorvo (2017). arXiv:1702.06340.

[44] S. Umehara, et al., Neutrino-less double-β decay of ^{48}Ca studied by CaF_2(Eu) scintillators, Phys. Rev. C 78 (2008) 058501. doi:10.1103/PhysRevC.78.058501.

[45] M. Agostini, et al., First results from GERDA Phase II, Journal of Physics: Conference Series 888 (2017) 012030. doi:10.1088/1742-6596/888/1/012030.

[46] A. S. Barabash, V. B. Brudanin, NEMO Collaboration, Investigation of double-beta decay with the nemo-3 detector, Physics of Atomic Nuclei 74 (2) (2011) 312–317. doi:10.1134/S1063778811020062.

[47] J. Argyriades, et al., Measurement of the two neutrino double beta decay half-life of zr-96 with the nemo-3 detector, Nuclear Physics A 847 (3) (2010) 168 – 179. doi:10.1016/j.nuclphysa.2010.07.009.

[48] R. Arnold, et al., Results of the search for neutrinoless double-β decay in ^{100}Mo with the NEMO-3 experiment, Phys. Rev. D 92 (2015) 072011. doi:10.1103/PhysRevD.92.072011.

[49] F. A. Danevich, A. S. Barabash, P. Belli, R. Bernabei, F. Cappella, V. Caracciolo, R. Cerulli, D. M. Chernyak, S. d' Angelo, A. Incicchitti, et al., Search for double beta decay of ^{116}Cd with enriched $^{116}CdWO_4$ crystal scintillators (Aurora experiment), Journal of Physics: Conference Series 718 (2016) 062009. doi:10.1088/1742-6596/718/6/062009.

[50] A. Barabash, Average and recommended half-life values for two-neutrino double beta decay, Nuclear Physics A 935 (2015) 52 – 64. doi:10.1016/j.nuclphysa.2015.01.001.

[51] C. Alduino, et al., Analysis techniques for the evaluation of the neutrinoless double-β decay lifetime in ^{130}Te with the CUORE-0 detector, Phys. Rev. C 93 (2016) 045503. doi:10.1103/PhysRevC.93.045503.

[52] A. Gando, et al., Search for Majorana Neutrinos Near the Inverted Mass Hierarchy Region with KamLAND-Zen, Phys. Rev. Lett. 117 (2016) 082503. doi:10.1103/PhysRevLett.117.082503.

[53] R. Arnold, et al., Measurement of the $2\nu\beta\beta$ decay half-life of ^{150}Nd and a search for $0\nu\beta\beta$ decay processes with the full exposure from the NEMO-3 detector, Phys. Rev. D 94 (2016) 072003. doi:10.1103/PhysRevD.94.072003.

[54] V. Marco, Model of the Response Function of CUORE Bolometers, Springer Netherlands, Dordrecht, 2011, Ch. 3, pp. 35–55. doi:10.1007/978-94-007-1232-4_3.

[55] C. Arnaboldi, et al., A calorimetric search on double beta decay of ^{130}Te, Physics Letters B 557 (3-4) (2003) 167–175. doi:10.1016/s0370-2693(03)00212-0.

[56] E. Andreotti, et al., ^{130}Te neutrinoless double-beta decay with CUORICINO, Astroparticle Physics 34 (11) (2011) 822–831. doi:10.1016/j.astropartphys.2011.02.002.

[57] K. Alfonso, et al., Search for Neutrinoless Double-Beta Decay of ^{130}Te with CUORE-0, Physical Review Letters 115 (10) (Sep 2015). doi:10.1103/physrevlett.115.102502.

[58] C. Alduino, et al., Measurement of the two-neutrino double-beta decay half-life of ^{130}Te with the CUORE-0 experiment, The European Physical Journal C 77 (1) (2017) 13. doi:10.1140/epjc/s10052-016-4498-6.

[59] C. Alduino, et al., CUORE sensitivity to $0\nu\beta\beta$ decay, The European Physical Journal C 77 (8) (Aug 2017). doi:10.1140/epjc/s10052-017-5098-9.

[60] C. Brofferio, O. Cremonesi, S. Dell'Oro, Neutrinoless double beta decay experiments with teo$_2$ low-temperature detectors, Frontiers in Physics 7 (2019) 86. doi:10.3389/fphy.2019.00086.

[61] D. R. Artusa, et al., Searching for Neutrinoless Double-Beta Decay of ^{130}Te with CUORE, Advances in High Energy Physics 2015 (2015) 1–13. doi:10.1155/2015/879871.

[62] J. Albert, Search for Majorana neutrinos with the first two years of EXO-200 data, Nature 510 (7504) (2014) 229–234. doi:10.1038/nature13432.

[63] J. B. Albert, et al., Sensitivity and discovery potential of the proposed nEXO experiment to neutrinoless double-β decay, Physical Review C 97 (6) (Jun 2018). doi:10.1103/physrevc.97.065503.

[64] M. Auger, et al., The EXO-200 detector, part I: detector design and construction, Journal of Instrumentation 7 (05) (2012) P05010–P05010. doi:10.1088/1748-0221/7/05/p05010.

[65] K.-H. Ackermann, et al., The GERDA experiment for the search of $0\nu\beta\beta$ decay in ^{76}Ge, The European Physical Journal C 73 (3) (Mar 2013). doi:10.1140/epjc/s10052-013-2330-0.

[66] M. Agostini, et al., Results on Neutrinoless Double-β Decay of ^{76}Ge from Phase I of the GERDA Experiment, Physical Review Letters 111 (12) (Sep 2013). doi:10.1103/physrevlett.111.122503.

[67] M. Agostini, et al., Background-free search for neutrinoless double-β decay of ^{76}Ge with GERDA, Nature 544 (7648) (2017) 47–52. doi:10.1038/nature21717.

[68] S. I. Alvis, et al., Search for neutrinoless double-β decay in ^{76}Ge with 26 kg·yr of exposure from the Majorana Demonstrator, Physical Review C 100 (2) (Aug 2019). doi:10.1103/physrevc.100.025501.

[69] M. Agostini, et al., Search of Neutrinoless Double Beta Decay with the GERDA Experiment, Nuclear and Particle Physics Proceedings 273-275 (2016) 1876 – 1882, 37th International Conference on High Energy Physics (ICHEP). doi:10.1016/j.nuclphysbps.2015.09.303.

[70] N. Abgrall, et al., The Majorana Demonstrator radioassay program, Nuclear Instruments and Methods in Physics Research Section A: Accelerators, Spectrometers, Detectors and Associated Equipment 828 (2016) 22–36. doi:10.1016/j.nima.2016.04.070.

[71] S. Abe, et al., Production of radioactive isotopes through cosmic muon spallation in KamLAND, Physical Review C 81 (2) (Feb 2010). doi:10.1103/physrevc.81.025807.

[72] A. Gando, et al., Measurement of the double-β decay half-life of136Xe with the KamLAND-Zen experiment, Physical Review C 85 (4) (Apr 2012). doi:10.1103/physrevc.85.045504.

[73] E. Caden, Status of the SNO+ Experiment, in: 15th International Conference on Topics in Astroparticle and Underground Physics (TAUP 2017) Sudbury, Ontario, Canada, July 24-28, 2017, 2017, pp. 1–5. arXiv:1711.11094.

[74] R. Arnold, et al., First Results of the Search for Neutrinoless Double-Beta Decay with the NEMO 3 Detector, Physical Review Letters 95 (18) (Oct 2005). doi:10.1103/physrevlett.95.182302.

[75] P. Povinec, Background constrains of the SuperNEMO experiment for neutrinoless double beta-decay searches, Nuclear Instruments and Methods in Physics Research Section A: Accelerators, Spectrometers, Detectors and Associated Equipment 845 (Jun 2016). doi:10.1016/j.nima.2016.06.104.

[76] R. Arnold, et al., Technical design and performance of the nemo 3 detector, Nuclear Instruments and Methods in Physics Research Section A: Accelerators, Spectrometers, Detectors and Associated Equipment 536 (1) (2005) 79 – 122. doi:10.1016/j.nima.2004.07.194.

[77] X. Chen, et al., PandaX-III: Searching for neutrinoless double beta decay with high pressure ^{136}Xe gas time projection chambers, Science China Physics, Mechanics & Astronomy 60 (6) (Apr 2017). doi:10.1007/s11433-017-9028-0.

[78] X. Cao, et al., PandaX: a liquid xenon dark matter experiment at CJPL, Science China Physics, Mechanics & Astronomy 57 (8) (2014) 1476–1494. doi:10.1007/s11433-014-5521-2.

[79] Karl Giboni, PANDAX Results and Outlook, CERN (Dec 2014).

[80] J. N. Marx, D. R. Nygren, The Time Projection Chamber, Phys. Today 31N10 (1978) 46–53. doi:10.1063/1.2994775.

[81] M. Redshaw, E. Wingfield, J. McDaniel, E. G. Myers, Mass and double-beta-decay Q value of Xe-136, Phys. Rev. Lett. 98 (2007) 053003. doi:10.1103/PhysRevLett.98.053003.

[82] P. M. McCowan, R. C. Barber, Q value for the double-β decay of ^{136}Xe, Phys. Rev. C 82 (2010) 024603. doi:10.1103/PhysRevC.82.024603.

[83] D. Nygren, High-pressure xenon gas electroluminescent TPC for 0ν beta beta-decay search, Nucl. Instrum. Meth. A603 (2009) 337–348. doi:10.1016/j.nima.2009.01.222.

[84] C. A. B. Oliveira, et al., Energy Resolution studies for NEXT, JINST 6 (2011) P05007. doi:10.1088/1748-0221/6/05/P05007.

[85] M. Miyajima, et al., Average energy expended per ion pair in liquid argon, Phys. Rev. A 9 (1974) 1438–1443. doi:10.1103/PhysRevA.9.1438.

[86] L. Serra, et al., An improved measurement of electron-ion recombination in high-pressure xenon gas, Journal of Instrumentation 10 (03) (2015) P03025–P03025. doi:10.1088/1748-0221/10/03/p03025.

[87] E. Aprile, et al., Scintillation Detectors, John Wiley & Sons, Ltd, 2006, Ch. 4, pp. 107–141. doi:10.1002/9783527610020.ch4.

[88] C. M. B. Monteiro, L. M. P. Fernandes, J. A. M. Lopes, L. C. C. Coelho, J. F. C. A. Veloso, J. M. F. d. Santos, K. Giboni, E. Aprile, Secondary scintillation yield in pure xenon, Journal of Instrumentation 2 (05) (2007) P05001–P05001. doi:10.1088/1748-0221/2/05/p05001.

[89] U. Fano, Ionization Yield of Radiations. II. The Fluctuations of the Number of Ions, Phys. Rev. 72 (1947) 26–29. doi:10.1103/PhysRev.72.26.

[90] A. Policarpo, M. Alves, M. Salete, S. Leite, M. dos Santos, Detection of soft X-rays with a xenon proportional scintillation counter, Nuclear Instruments and Methods 118 (1) (1974) 221 – 226. doi:10.1016/0029-554X(74)90706-X.

[91] T. Doke, A. Hitachi, S. Kubota, A. Nakamoto, T. Takahashi, Estimation of Fano factors in liquid argon, krypton, xenon and xenon-doped liquid argon, Nuclear Instruments and Methods 134 (2) (1976) 353 – 357. doi:10.1016/0029-554X(76)90292-5.

[92] E. Conti, et al., Correlated fluctuations between luminescence and ionization in liquid xenon, Phys. Rev. B 68 (2003) 054201. doi:10.1103/PhysRevB.68.054201.

[93] P. Ferrario, et al., First proof of topological signature in the high pressure xenon gas TPC with electroluminescence amplification for the NEXT experiment, JHEP 01 (2016) 104. doi:10.1007/JHEP01(2016)104.

[94] J. Toledo, H. Muller, R. Esteve, J. M. Monzó, A. Tarazona, S. Martoiu, The Front-End Concentrator card for the RD51 Scalable Readout System, Journal of Instrumentation 6 (11) (2011) C11028–C11028. doi:10.1088/1748-0221/6/11/c11028.

[95] V. Álvarez, F. Borges, S. Cárcel, J. Castel, S. Cebrián, A. Cervera, C. Conde, T. Dafni, T. Dias, J. Díaz, et al., Near-intrinsic energy resolution for 30–662 keV gamma rays in a high pressure xenon electroluminescent TPC, Nuclear Instruments and Methods in Physics Research Section A: Accelerators, Spectrometers, Detectors and Associated Equipment 708 (2013) 101–114. doi:10.1016/j.nima.2012.12.123.

[96] C. A. B. Oliveira, Results from the NEXT prototypes, Journal of Physics: Conference Series 460 (2013) 012011. doi:10.1088/1742-6596/460/1/012011.

[97] V. Álvarez, F. Aznar, F. I. G. M. Borges, D. Calvet, S. Cárcel, J. Castel, S. Cebrián, A. Cervera, C. A. N. Conde, T. Dafni, et al., Description and commissioning of NEXT-MM prototype: first results from operation in a Xenon-Trimethylamine gas mixture, Journal of Instrumentation 9 (03) (2014) P03010–P03010. doi:10.1088/1748-0221/9/03/p03010.

[98] V. Alvarez, F. Borges, et al., Characterization of a medium size Xe/TMA TPC instrumented with microbulk Micromegas, using low-energy γ-rays, Journal of Instrumentation 9 (Nov 2013). doi:10.1088/1748-0221/9/04/C04015.

[99] F. Monrabal, et al., The NEXT White (NEW) detector, Journal of Instrumentation 13 (12) (2018) P12010–P12010. doi:10.1088/1748-0221/13/12/p12010.

[100] J. J. Gómez-Cadenas, J. Martín-Albo, NEXT, a HPXe TPC for neutrinoless double beta decay searches, Journal of Physics: Conference Series 136 (4) (2008) 042048. doi:10.1088/1742-6596/136/4/042048.

[101] V. Álvarez, et al., The NEXT-100 experiment for neutrinoless double beta decay searches (Conceptual Design Report), arXiv e-prints (2011). arXiv:1106.3630.

[102] V. Álvarez, F. I. G. M. Borges, et al., NEXT-100 Technical Design Report (TDR). Executive summary, Journal of Instrumentation 7 (06) (2012) T06001–T06001. doi:10.1088/1748-0221/7/06/t06001.

[103] J. Martín-Albo, et al., Sensitivity of NEXT-100 to neutrinoless double beta decay, Journal of High Energy Physics 2016 (5) (May 2016). doi:10.1007/jhep05(2016)159.

[104] L. Rogers, Searching for $0\nu\beta\beta$ in high pressure xenon gas time projection chambers, CERN (May 2019).

[105] K. Lung, et al., Characterization of the Hamamatsu R11410-10 3-in. photomultiplier tube for liquid xenon dark matter direct detection experiments, Nuclear Instruments and Methods in Physics Research Section A: Accelerators, Spectrometers, Detectors and Associated Equipment 696 (2012) 32 – 39. doi:10.1016/j.nima.2012.08.052.

[106] K. Lung, et al., Characterization of the Hamamatsu R11410-10 3-Inch Photomultiplier Tube for Liquid Xenon Dark Matter Direct Detection Experiments, Nucl. Instrum. Meth. A 696 (2012) 32–39. doi:10.1016/j.nima.2012.08.052.

[107] G. Martínez Lema, Low-energy calibration, reconstruction software and light-collection efficiency parametrization of the NEXT-White detector, Ph.D. thesis, Santiago de Compostela U. (Jul 2018).

[108] T. H. Cormen, C. E. Leiserson, R. L. Rivest, C. Stein, Introduction to Algorithms, Third Edition, 3rd Edition, The MIT Press, 2009.

[109] G. Martínez-Lema, et al., Calibration of the NEXT-White detector using ^{83m}Kr decays, JINST 13 (10) (2018) P10014. doi:10.1088/1748-0221/13/10/P10014.

[110] C. A. B. Oliveira, M. Sorel, J. Martin-Albo, J. J. Gomez-Cadenas, A. L. Ferreira, J. F. C. A. Veloso, Energy resolution studies for NEXT, Journal of Instrumentation 6 (05) (2011) P05007–P05007. doi:10.1088/1748-0221/6/05/p05007.

[111] D. Lorca, et al., Characterisation of NEXT-DEMO using xenon K_α X-rays, JINST 9 (10) (2014) P10007. doi:10.1088/1748-0221/9/10/P10007.

[112] J. Renner, G. Díaz López, P. Ferrario, J. A. Hernando Morata, M. Kekic, G. Martínez-Lema, F. Monrabal, J. J. Gómez-Cadenas, C. Adams, et al., Energy calibration of the next-white detector with 1 resolution near $q_{\beta\beta}$ of ^{136}xe, Journal of High Energy Physics 2019 (10) (Oct 2019). doi:10.1007/jhep10(2019)230.

[113] Probfit, https://probfit.readthedocs.io/en/latest/ (2012).

[114] Iminuit, https://iminuit.readthedocs.io/en/stable/ (2012).

[115] J. Benlloch-Rodriguez, The NEXT experiment for neutrinoless double beta decay searches, Journal of Physics: Conference Series 1468 (2020) 012110. doi:10.1088/1742-6596/1468/1/012110.

[116] E. Freitas, C. Monteiro, M. Ball, J. Gómez-Cadenas, J. Lopes, T. Lux, F. Sánchez, J. dos Santos, Secondary scintillation yield in high-pressure xenon gas for neutrinoless double beta decay ($0\nu\beta\beta$) search, Physics Letters B 684 (4) (2010) 205 – 210. doi:10.1016/j.physletb.2010.01.013.

[117] S. Umehara, et al., Search for Neutrino-less Double Beta Decay with CANDLES, Physics Procedia 61 (2015) 283 – 288, 13th International Conference on Topics in Astroparticle and Underground Physics, TAUP 2013. doi:10.1016/j.phpro.2014.12.046.

[118] Y. Hirano, et al., Study of double beta decay of48Ca with CANDLES, Journal of Physics: Conference Series 120 (5) (2008) 052053. doi:10.1088/1742-6596/120/5/052053.

[119] F. Ferroni, Calorimetry at 10mK, Journal of Physics: Conference Series 293 (2011) 012005. doi:10.1088/1742-6596/293/1/012005.

[120] F. Orio, Current status and perspectives of the LUCIFER experiment, Nuclear and Particle Physics Proceedings 273-275 (2016) 1795 – 1800, 37th International Conference on High Energy Physics (ICHEP). doi:10.1016/j.nuclphysbps.2015.09.289.

[121] K. Zuber, The status of the COBRA double-beta-decay experiment, Progress in Particle and Nuclear Physics 64 (2) (2010) 267 – 269, neutrinos in Cosmology, in Astro, Particle and Nuclear Physics. doi:10.1016/j.ppnp.2009.12.025.

[122] J. Ebert, et al., The COBRA demonstrator at the LNGS underground laboratory, Nuclear Instruments and Methods in Physics Research Section A: Accelerators, Spectrometers, Detectors and Associated Equipment 807 (2016) 114–120. doi:10.1016/j.nima.2015.10.079.

[123] J. Ebert, et al., Results of a search for neutrinoless double-βdecay using the COBRA demonstrator, Physical Review C 94 (2) (Aug 2016). doi:10.1103/physrevc.94.024603.

[124] T. Ishikawa, et al., Three-dimensional drift chambers of the dcba experiment for neutrinoless double beta decay search, Nuclear Instruments and Methods in Physics Research Section A: Accelerators, Spectrometers, Detectors and Associated Equipment 628 (1) (2011) 209 – 211, vCI 2010. doi:10.1016/j.nima.2010.06.318.

[125] N. Ishihara, et al., DCBA experiment for searching for neutrinoless double beta decay (II), Journal of Physics: Conference Series 120 (2008) 052062. doi:10.1088/1742-6596/120/5/052062.

[126] H. Iwase, et al., The DCBA/MTD Experiments for Neutrinoless Double Beta Decay Search, Proceedings of the 12th Asia Pacific Physics Conference (APPC12) (2014). doi:10.7566/JPSCP.1.013023.

[127] M. Nomachi, et al., Moon (mo observatory of neutrinos) for double beta decay, Nuclear Physics B - Proceedings Supplements 138 (2005) 221 – 223, proceedings of the Eighth International Workshop on Topics in Astroparticle and Undeground Physics. doi:10.1016/j.nuclphysbps.2004.11.053.

[128] M. Sisti, et al., FLARES: A flexible scintillation light apparatus for rare event searches, Nuclear Instruments and Methods in Physics Research Section A: Accelerators, Spectrometers, Detectors and Associated Equipment 824 (2016) 661 – 664, frontier Detectors for Frontier Physics: Proceedings of the 13th Pisa Meeting on Advanced Detectors. doi:10.1016/j.nima.2015.09.028.

[129] M. Beretta, FLARES, https://ui.adsabs.harvard.edu/abs/2018arXiv180311362B (Mar. 2018).

[130] V. Bonvicini, et al., A flexible scintillation light apparatus for rare event searches, The European Physical Journal C 74 (11) (Nov 2014). doi:10.1140/epjc/s10052-014-3151-5.

[131] H. Bhang, et al., AMoRE experiment: a search for neutrinoless double beta decay of ^{100}Mo isotope with ^{40}Ca^{100}MoO$_4$ cryogenic scintillation detector, Journal of Physics: Conference Series 375 (4) (2012) 042023. doi:10.1088/1742-6596/375/1/042023.

[132] AMoRE experiment, Status, https://amore.ibs.re.kr/about/status/ (2019).